EXTREME GROUND EFFECT

by

Gillian Margaret Read

B.Sc.(Hons.), University of Adelaide, South Australia.

Thesis submitted for the degree of

Doctor of Philosophy

in the Department of Applied Mathematics,

University of Adelaide.

October, 1988.

CONTENTS

SUMMARY

The work presented in this thesis involves an analysis of thin bodies moving in extreme ground effect; that is, in close proximity to a plane ground surface.

In chapter 1, a brief introduction to the study of extreme ground effect is given and the purpose and scope of this thesis presented.

In chapter 2, some applications of the one dimensional gap flow problem are discussed. In particular, the aerodynamics of the read–write heads on computers are investigated for both hard discs and elastic discs. Some suggestions for other applications are made.

In chapter 3, the extreme ground effect problem for a thin body of general planform is detailed. The partial differential equation governing the two dimensional flow in the gap and the associated leading edge and trailing edge boundary conditions are derived in the limit as the clearance tends to zero, using the method of matched asymptotic expansions.

A boundary integral equation method to solve the resulting equations is developed in chapter 4 for the special case when the clearance between the body and the ground is constant in y and exponential in x. This method incorporates analytical and numerical techniques in approximating the integral equation by a matrix equation.

In chapter 5, the location of the transition point between the leading edge and the trailing edge is investigated for two special cases. Firstly, some theory is developed to determine the location of the transition point for thin bodies with low aspect ratio, and is illustrated using elliptical bodies. Secondly, the transition point location is studied for bodies with planforms which are near–rectangles. This results in a conclusion being made for rectangular bodies.

In chapter 6, the theory and integral equation method are applied to problems in which the transition points between the leading edge and the trailing edge are fixed. Skirts (as used in some racing cars) are incorporated, and comparisons are made for bodies with and without skirts. An inverse solution is developed and used as a comparison for the program.

Some concluding remarks and also some suggestions for further research in this area are made in chapter 7.

SIGNED STATEMENT

This thesis contains no material which has been accepted for the award of any other degree or diploma in any University.

To the best of my knowledge and belief, this thesis contains no material previously published or written by another person, except where due reference is made in the text of the thesis.

I consent to this thesis being made available for photocopying and loan.

Gillian M. Read

ACKNOWLEDGEMENTS

I would like to thank my supervisor, Professor E. O. Tuck, sincerely for his patience, guidance and encouragement during my time as a postgraduate. Thanks also go to David Beard for his assistance with some of the computing aspects of this thesis, and to Kerrie James, Michael Rumsewicz and Steve Hayes for their friendship through the years. Finally, I would like to thank Hugh and my family for their support.

CHAPTER 1

INTRODUCTION

In this thesis, we examine the flow around bodies which are in close proximity to a plane ground surface. Consider, for example, steady air flow around a body of revolution aligned with a free stream. Away from any ground plane, the flow around such a body is symmetrical and free of lateral forces. The air flows smoothly around all sides of the body and, at the rear of the body, the flows converge and realign. However, when this body is brought near a ground plane, the air flow is distorted due to the presence of the ground plane and the flow is no longer symmetrical. This phenomenon is known as ground effect and it is of practical importance in many contexts, whether or not the body is axisymmetric.

One of the earliest studies of ground effect, by Pistolesi (1937), required that the clearance between the body and the ground be large compared to all length scales of the body. Essentially, this meant that all effects of the ground plane were perturbations to the infinite flow field.

Later studies have investigated the problem in which the gap clearance is comparable to some body dimension and the effects of the ground are O(1) perturbations to the infinite fluid. For example, Bagley (1961) and Tuck and Newman (1974) considered the steady ground effect problem of a thin airfoil for which the clearance between the body and the ground was comparable to the chord.

When the clearance is small compared to the length of the body, the problem is known as a small–gap problem. Some authors have investigated this problem for thin bodies when the thickness/chord ratio and angle of attack are small compared to the clearance/chord ratio. This leads to a linear theory in which the flow departs little from the uniform stream everywhere. One such study was by Widnall and Barrows (1970), who provided a complete asymptotic solution for the steady flow case.

When the thickness/chord ratio and the angle of attack are small but of the same order as the gap clearance/chord ratio, the flow in the gap between the body and the ground is no longer a perturbation of the uniform stream. This nonlinear small–gap problem has been studied by Strand, Royce and Fujita (1962), Newman (1982) and Tuck (1980), (1981) and (1983) amongst others. One of the main features of ground effect is that it enhances lift, and so this work has relevance to several applications in aerodynamics.

Since the early days of aviation, interest in ground effect aerodynamics has resulted in the design of experimental vehicles which fly at low altitudes. These vehicles would thus take advantage of the increased lift and reduced drag that occur when a vehicle is flying in ground effect. These benefits would allow the vehicles to fly longer distances more economically than when out of ground effect, and, as they would be capable of flying over water, land and ice, they could be used in a variety of roles. Depending on the size of the vehicles, they could be used as search–and–rescue craft or to transport cargo long distances (Ollila (1980)).

Although we shall concentrate on flight over a ground plane, theory for flight over water has been developed by Tuck (1984) and Grundy (1986).

The enhancement of negative lift or down force, due to the presence of a ground plane, for a wing at negative angle of attack has applications to very streamlined, low to the ground vehicles. In particular, extreme ground effect contributes significantly to the aerodynamics of racing cars (Wise (1979)). Most racing cars can be considered as upside down wings and, therefore, cause little disturbance to the flow above the vehicle. Consequently, to study the aerodynamics of these vehicles, it is important to investigate the flow under the vehicle.

A vast amount of research has been done on the airflow over road vehicles, to the extent that most current production cars have a lower drag coefficient than their predecessors (Holt (1982)). It is apparent, however, that an explanation of ground effect would contribute significantly to the understanding of vehicle aerodynamics (Sovran et al (1978)) and enable the drag coefficient to be further reduced. Some automobile designers are now investigating the relationship between the underbody shape and drag as the next area of refinement for improving the drag coefficient and performance. For example, research performed by Volkswagenwerk AG on the Auto 2000 showed that by sealing the underbody of the car, the drag coefficient was lowered from 0.25 to 0.22. Although the addition of a sealed underbody may not always be practical, it does illustrate the contribution of the under–vehicle flow to the aerodynamics of the vehicle as a whole.

The three dimensional flow around a bluff body is extremely complex and,

therefore, some models use a two dimensional flow to represent the flow field. Tuck (1971) provided solutions for two dimensional flows using both small–gap asymptotic expansions and direct numerical computation, with close agreement between the two. The work presented in this thesis is for thin three dimensional bodies and, therefore, more directly applicable to racing cars.

Another area of relevance to extreme ground effect is the aerodynamics of read–write heads on computers. These heads are required to fly with minimal clearance above the disc and so most research in this area, by such authors as Adams (1980), Kogure et al (1983) and Shepherd (1986), uses lubrication theory to solve flow problems. For high Reynolds numbers, Tuck and Bentwich (1983) found that the solutions to this small–gap problem were those predicted by an inviscid small–gap theory. It may, therefore, be possible to explain some air–lubrication phenomena without invoking viscous effects (Tuck (1980)).

Ground effect theory also has biological applications. The first prosthetic heart valves were of the "ball in a cage" type, mainly because of their mechanical simplicity. More recently, valve designs have involved hinged, rigid, cambered leaflets (Scotten et al (1980)). Such a leaflet is required, when fully open, to provide minimum obstruction to forward flow and when the flow is reversed, it must close rapidly to block off the flow. In two dimensions, the leaflet can be represented by a thin airfoil, which, because of its proximity to one arterial wall when fully open, is in ground effect (Tuck (1982a)). Therefore, the design features of leaflet valves may be investigated using ground effect theory.

One final suggestion as an application for ground effect theory is the dynamics of skimboards or surf skimmers. These skimboards are flat, circular discs measuring about a metre in diameter and are used in very shallow water. The rider jumps on to the board and can travel for quite long distances (5–10 metres) at speeds of 2–3 metres per second (Edge (1968)). In order to achieve this, the dynamics of the flow below the board must be such as to produce high lift at low drag, and these are the properties of extreme ground effect.

The aim of this thesis is to develop a method for solving the flow around a thin body of general planform moving in extreme ground effect.

As an introduction to some of the mathematics involved in extreme ground effect problems, we present three examples in chapter two. In each of these problems, the flow around the thin body is assumed to be two dimensional everywhere and, therefore, the analysis is applicable to thin bodies of high aspect (span/chord) ratio. In the small gap below the body, there is little vertical flow variation and so the global two dimensional flow is approximated by a local one dimensional flow. To solve such problems, we need only determine the one dimensional gap flow, as the flow elsewhere remains virtually undisturbed by the presence of the thin body.

In chapter three, we consider three dimensional flow around a thin body in extreme ground effect. Once again, we need only solve the gap flow problem, in which the global three dimensional flow is approximated by a local two dimensional flow. Using the method of matched asymptotic expansions (Van Dyke (1964)), we

obtain the partial differential equation governing this two dimensional flow in the gap and the associated boundary conditions.

In the fourth chapter, we present a boundary integral equation method for solving these equations in the special case when the clearance between the body and the ground is constant in y and exponential in x. This method incorporates a combination of numerical and analytical techniques in approximating the integral equation describing variation of velocity potential along the edge contour by a matrix equation. The velocity potential and its normal derivative are then determined from the matrix equation using an iterative scheme.

The program developed in chapter four is then used to investigate different aspects of ground effect theory. In chapter five, the location of the transition point between the leading edge and the trailing edge is examined for two special cases; namely, for planforms with low aspect ratio and for planforms which are nearly rectangular in shape. In chapter six, we consider the flow around rectangular planforms with fixed transition points. We also investigate, for rectangular bodies, the effect that skirts (that is, fixed lateral flow barriers) have on the lift. The results presented illustrate the properties of extreme ground effect and, where possible, are supported by exact or previously published solutions.

CHAPTER 2

APPLICATIONS OF THE ONE DIMENSIONAL GAP FLOW PROBLEM

We present here three models covering various aspects of ground effect. In each example, the body is thin and the flow everywhere is assumed to be two dimensional. As discussed in the introduction, the presence of the thin body causes little disturbance almost everywhere to the uniform stream, and we need only solve for the flow where this is not true; that is, in the gap below the body.

2.1 Flat Plate over an Elastic Surface

Stretch–surface recording is a relatively new technique of computer disc recording using a rigid plastic disc with raised edges. A flexible membrane is stretched across and slightly above both surfaces of the disc. The disc head flies above the surface and air pressure causes the membrane to dimple beneath the head leaving a non–uniform gap. This deformation has the advantage of keeping the surface relatively free of debris as the continually moving dimpled area restores itself rapidly, flinging off any debris.

We can model this situation using the following simplifications. Firstly, we choose a frame of reference in which the disc head, held above the disc, is fixed in space relative to the disc surface. Then we assume steady, two dimensional, irrotational flow of an incompressible fluid (air) around the disc head. The head can essentially be thought of as a flat plate riding at an angle of attack and its

presence causes the disc surface to undergo deformation. The flow geometry for this model is illustrated in figure 2.1.

The surface of the disc is described by $y = \eta(x)$ and has an associated flexibility parameter T measuring the tension in the membrane. The plate is fixed between $x = 0$ and $x = L$ and its height, above the undisplaced disc surface, is defined by $h_0 = h_0(x)$, $0 \leq x \leq l$. The plate must be close to the surface and, therefore, $h_0 = O(\epsilon)$ where ϵ is a small parameter. Our aim is to determine the unknown shape of the deformed disc surface and to investigate the associated pressure and velocity profiles.

We denote the velocity in the gap between the disc head and the disc surface by $u = u(x)$ and elsewhere, the velocity is the uniform stream velocity U. The one dimensional character of the flow in the gap region demands that the velocity flux be constant through the gap. That is, the gap flow must satisfy the one dimensional continuity equation:

$$\frac{d}{dx}\Big(u(x)\big[h_0(x) - \eta(x)\big]\Big) = 0. \tag{2.1}$$

If $p(x)$ denotes the excess of pressure over the free stream value, then from Bernoulli's equation

$$p(x) = \frac{1}{2}\rho U^2 - \frac{1}{2}\rho[u(x)]^2, \tag{2.2}$$

where ρ is the density of air. There is a wake emanating from the trailing edge and the pressure is required to be continuous across this wake. For our problem, it is sufficient to note that continuity of pressure defines the Kutta condition at

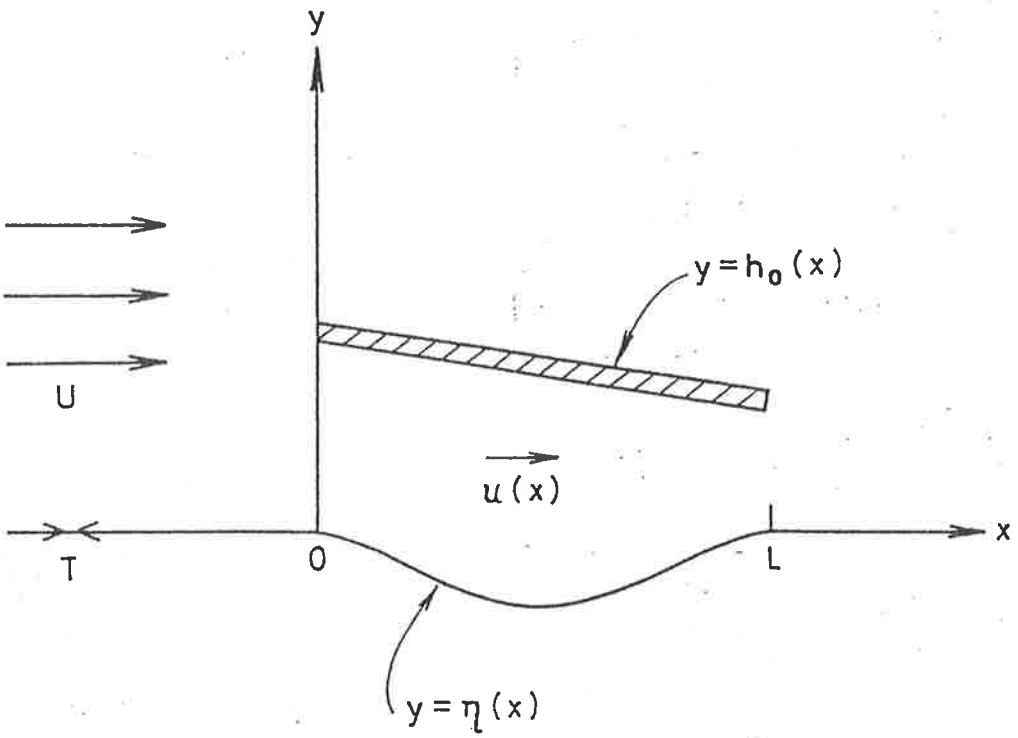

Figure 2.1 Sketch of flow geometry for the situation of a flat plate at an angle of attack flying above an elastic surface.

the trailing edge. By applying this condition to equation (2.1), we can rewrite the continuity equation as

$$u(x)\big[h_0(x) - \eta(x)\big] = U h_0(L). \tag{2.3}$$

The presence of the plate above the disc surface causes the surface to be displaced as described by the membrane–tension equation (Batchelor p. 64 (1970)):

$$p(x) = T\frac{d^2}{dx^2}\eta(x). \tag{2.4}$$

From equations (2.2), (2.3) and (2.4), we can derive the following second order non-linear differential equation in $\eta(x)$:

$$\frac{d^2}{dx^2}\eta(x) = \frac{\rho U^2}{2T}\left[1 - \frac{h_0^2(L)}{[h_0(x) - \eta(x)]^2}\right]. \tag{2.5}$$

We seek a solution to this equation subject to the boundary conditions

$$\eta(0) = 0, \quad \eta(L) = 0; \tag{2.6}$$

that is, the displacement of the surface is confined to that section of the disc directly below the plate.

If we make a substitution of the form

$$H(x) = h_0(x) - \eta(x), \tag{2.7}$$

then, as $h_0(x)$ is a linear function in x, equation (2.5) reduces to

$$\frac{d^2}{dx^2}H(x) = \frac{\rho U^2}{2T}\left[\frac{h_0^2(L)}{H(x)^2} - 1\right], \tag{2.8}$$

with the associated boundary conditions

$$H(0) = h_0(0), \quad H(L) = h_0(L). \tag{2.9}$$

After integrating once with respect to x, this equation becomes

$$\frac{d}{dx}H(x) = \lambda \left[K - \left(H(x) + \frac{H^2(L)}{H(x)}\right)\right]^{\frac{1}{2}}, \tag{2.10}$$

in which K is a constant of integration and $\lambda = \pm(\rho U^2/T)^{\frac{1}{2}}$. By separating the variables in this differential equation, we can rewrite it as an integral equation, relating the displacement of the disc surface below the disc head to the relative position along the head:

$$\int_{H(L)}^{H(x)} \left(K - H - H^2(L)H^{-1}\right)^{-\frac{1}{2}} dH = \lambda(x - L). \tag{2.11}$$

We will now solve this elliptic integral equation using numerical integration.

We divide the region under the body $[0, L]$ into N uniform subintervals (x_{j-1}, x_j) where $x_0 = 0$ and $x_N = L$ and denote the unknown displacement under the head by

$$H(x) = H(x_j) = H_j. \tag{2.12}$$

Using this notation, equation (2.11) can be written as

$$\sum_{j=i}^{N} \int_{H_j}^{H_{j-1}} \left(K - H - H^2(L)H^{-1}\right)^{-\frac{1}{2}} dH = \lambda(x_i - L), \quad i = 0, \ldots, N. \tag{2.13}$$

We can determine all the unknown clearances H_j from this equation.

Firstly, we determine H_{N-1} by applying an iterative scheme to

$$\int_{H_N}^{H_{N-1}} F(H)\, dH = \lambda(x_{N-1} - L), \tag{2.14}$$

in which $F(H) = \left(K - H - H^2(L)H^{-1}\right)^{-\frac{1}{2}}$. When the plate is situated with positive angle of attack, λ takes the negative sign and we estimate the value of H_{N-1} to be $g_2 = H_N + 2\Delta g$, where Δg is less than the accuracy required. We then evaluate

$$I_1 = \int_{H_N}^{g_2} F(H)\, dH \tag{2.15}$$

using Simpson's rule; that is,

$$I_1 = \frac{\Delta g}{3}\Big(F(H_N) + 4F(g_1) + F(g_2)\Big). \tag{2.16}$$

If $I_1 < \lambda(x_{N-1} - L)$, the estimation of H_{N-1} is increased to $g_4 = H_N + 4\Delta g$ and we compute

$$I_2 = I_1 + \int_{g_2}^{g_4} F(H)\, dH. \tag{2.17}$$

This process is repeated until we find n for which I_n is closest to $\lambda(x_{N-1} - L)$. Thus, the clearance H_{N-1} is given by $H_{N-1} = g_{2n}$. In the same way, the other clearances H_j can be computed. We note that for negative angle of attack, the same method is used but with λ taking the positive sign and the H_j's decreasing as j decreases.

As an example, we consider a flat plate held above the disc surface with positive angle of attack and trailing edge clearance of 0.1 cm. The horizontal length is chosen to be 1 cm and the uniform stream is 10 cm/sec. If we assume that the air has density 1.29 x 10^{-3} g/cm^3 (Batchelor (1970)), then for any given T and K, we can determine the leading edge clearance and the displacement of the disc surface. If K takes the value 2 and the flexibility parameter T is chosen to be

10 g/sec^{-2}, then the leading edge clearance is found to be 0.25 cm and the surface displacement η is almost symmetrical. These results are illustrated in figure 2.2.

After we have solved for $\eta(x)$ and $h_0(x)$, we can use equations (2.3) and (2.2) to find the gap velocity $u(x)$ and the gap pressure $p(x)$. Figure 2.3 contains graphs of both $u(x)$ and $p(x)$ plotted against x. As the surface displacement produced in this example is very small, the results are very close to those for the same plate over a rigid surface. These graphs are as expected, with the minimum pressure and maximum velocity being located at the trailing edge, and the maximum pressure and minimum velocity at the leading edge.

Figures 2.4 and 2.5 illustrate the relationship between the various parameters involved when a plate is held above an elastic surface in a stream of moving air. We denote the ratio between the leading edge clearance and the trailing edge clearance by μ and determine how this varies with λ for a fixed value of K. In any given stream of air, ρ and U are constant and λ changes at a rate inversely proportional to $T^{1/2}$. Hence, the horizontal axis can also be thought of as representing T.

One feature apparent in figures 2.4 and 2.5 is that each plot has both an upper bound and a lower bound. We can readily predict these limiting values by finding the zeros of equation (2.10). These graphs may be used to determine in which way the parameters should be changed in order to satisfy different aims. For example, if we require greater surface deformation for a given angle of attack, we can reduce the value of K, enabling us to use a smaller value of T. As previously

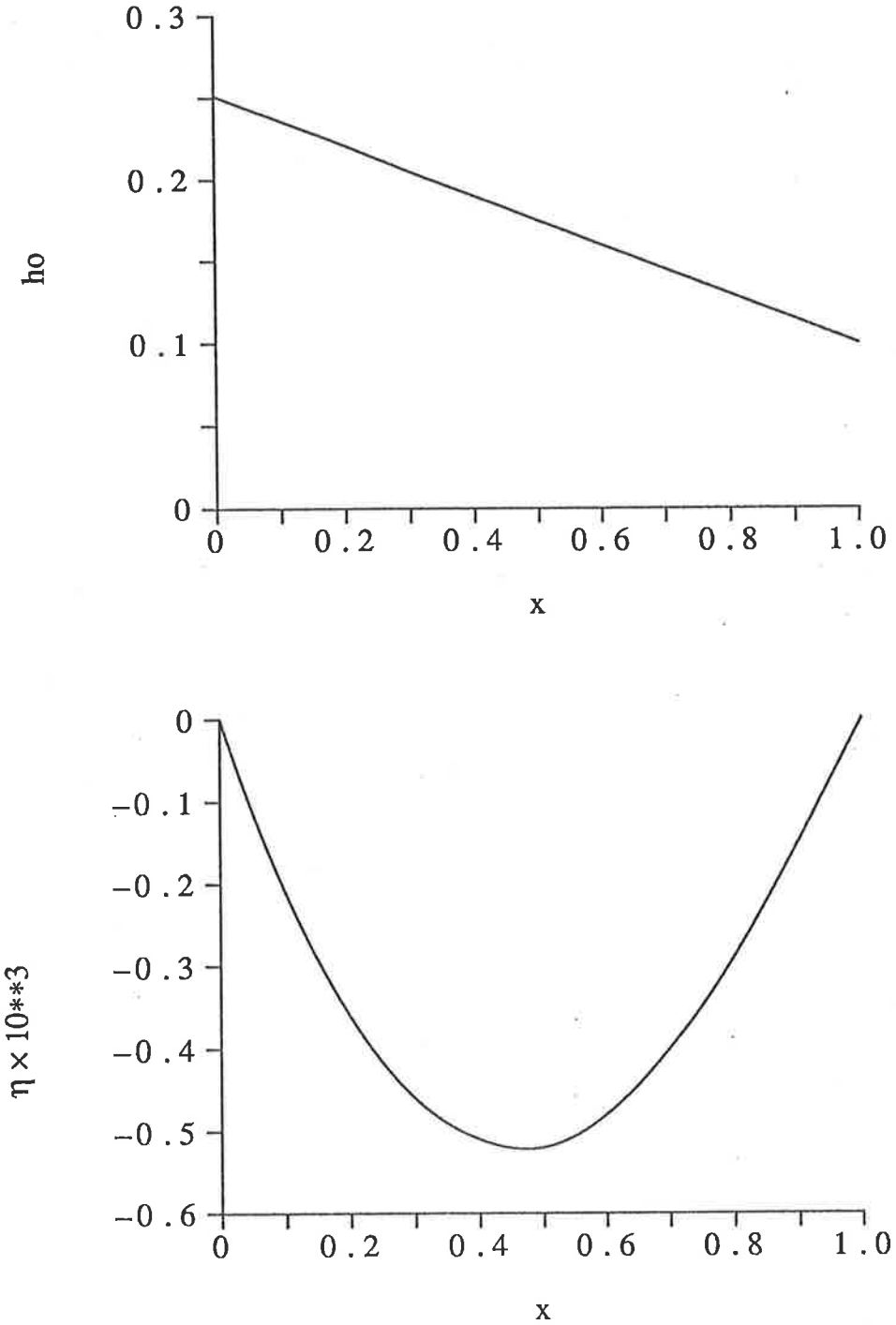

Figure 2.2 The top graph represents the height h_0 of the plate above the undisplaced surface $y = 0$. The lower graph is a plot of the displaced disc surface $\eta(x)$ against x.

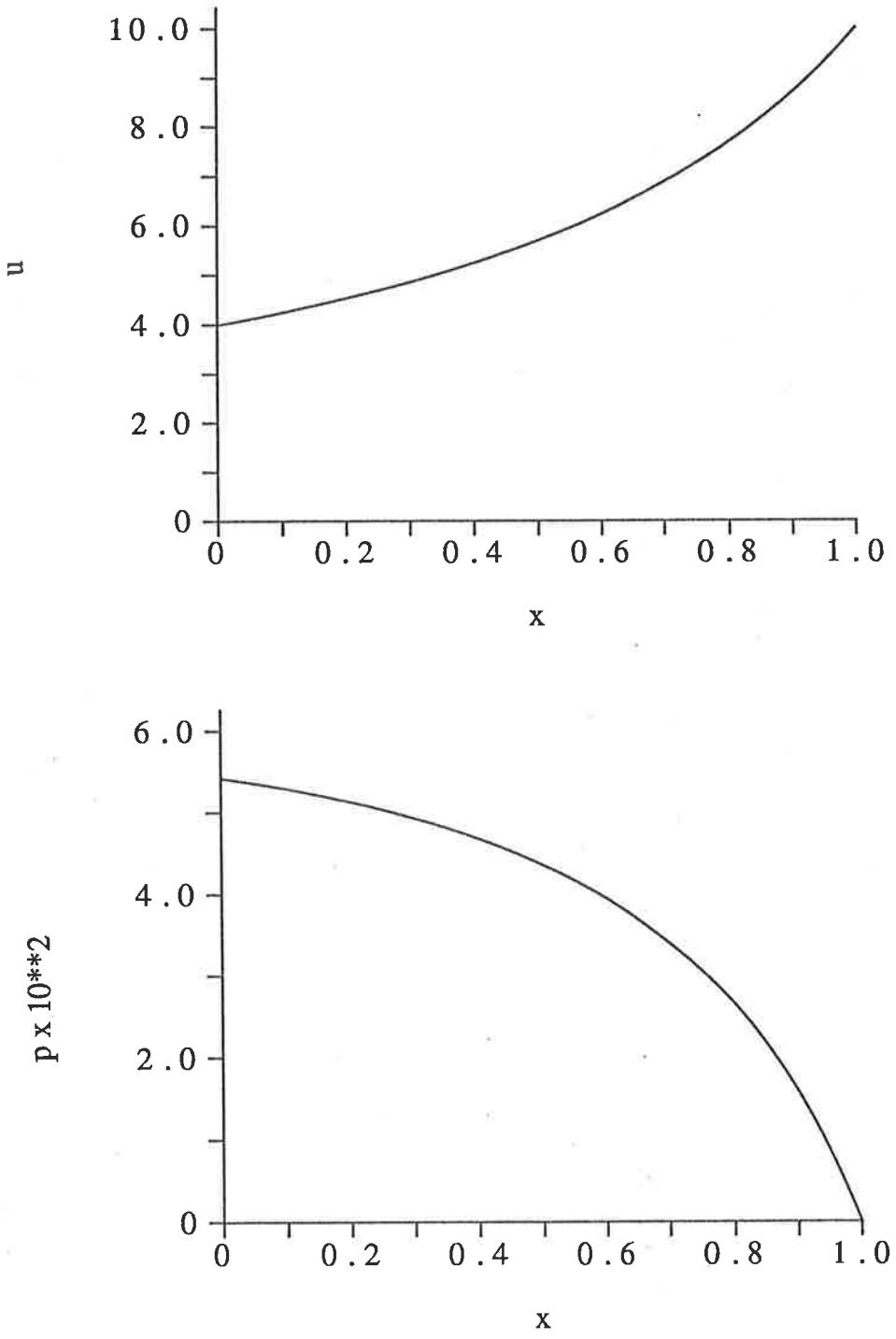

Figure 2.3 Plots of the pressure p and the velocity u in the gap between the plate and the disc surface against x.

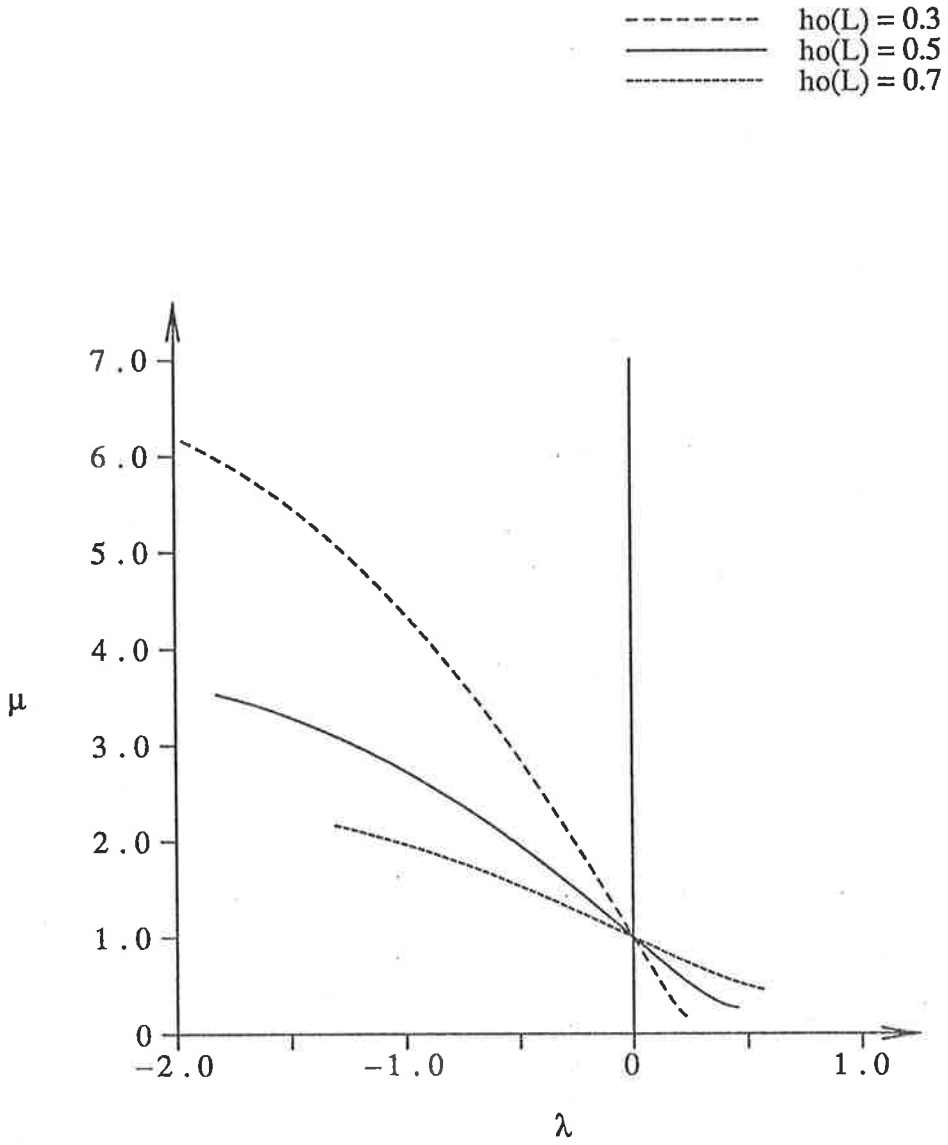

Figure 2.4 This graph represents the relationship between the parameters involved in the problem of the plate above the elastic disc. The ratio μ between the leading and trailing edge heights has been plotted against the parameter λ, which describes the flexibility of the disc for $K = 2.0$. The length L takes the value one in this example.

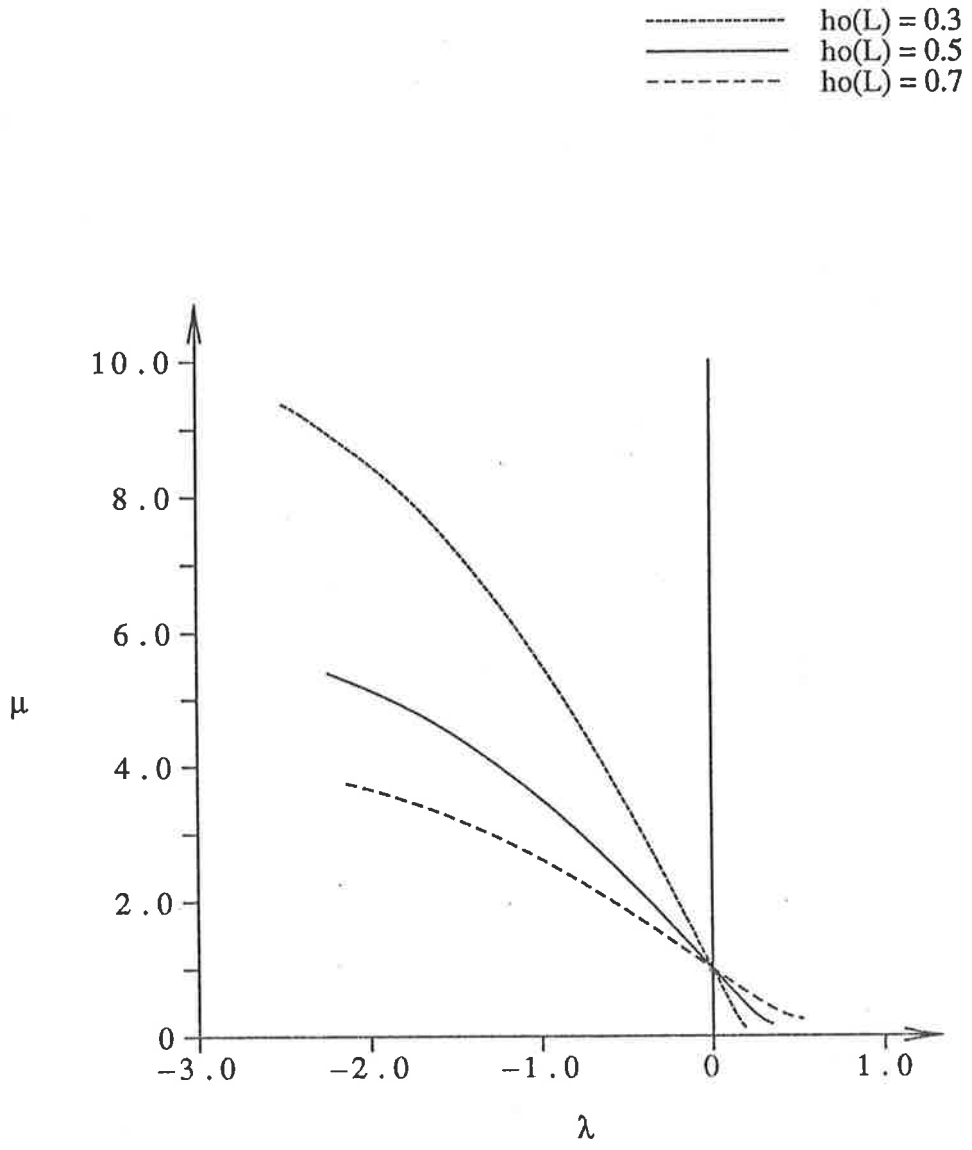

Figure 2.5 This graph is as described in the previous figure but with K taking the value 3.0.

mentioned, this would be beneficial as the moving surface would fling off any debris.

2.2 Conventional and Aerodynamically–retarded Head Crashes

In the previous section, we examined the problem of a read–write head held above an elastic disc surface. We will now consider disc heads which read and write information on hard discs, and investigate what happens when they crash. When the discs are at rest, the heads are in contact with the surface and as the disc moves, the lubrication pressure causes them to rise above the disc. They are constructed in an inverted U–shape (see figure 2.6) with the ends of the U containing the magnetic elements, and designed to be very close to the disc surface. The bridge of the U is much further from the disc and, therefore, not usually considered when examining the aerodynamics of the head. The faster the disc moves, the greater the lubrication forces and hence the greater the clearance. Since the success of reading and writing information depends on the head being very close to the disc surface, some method of counteracting this movement is required.

Tuck (1985) showed that by using a suitably designed head, the aerodynamics of the whole disc head could provide such a method. He considered the head in two separate portions – the ends or Reynolds portion subject to viscous forces proportional to speed, and the bridge or Bernoulli portion subject to inertial forces proportional to speed squared. The first of these forces must be positive

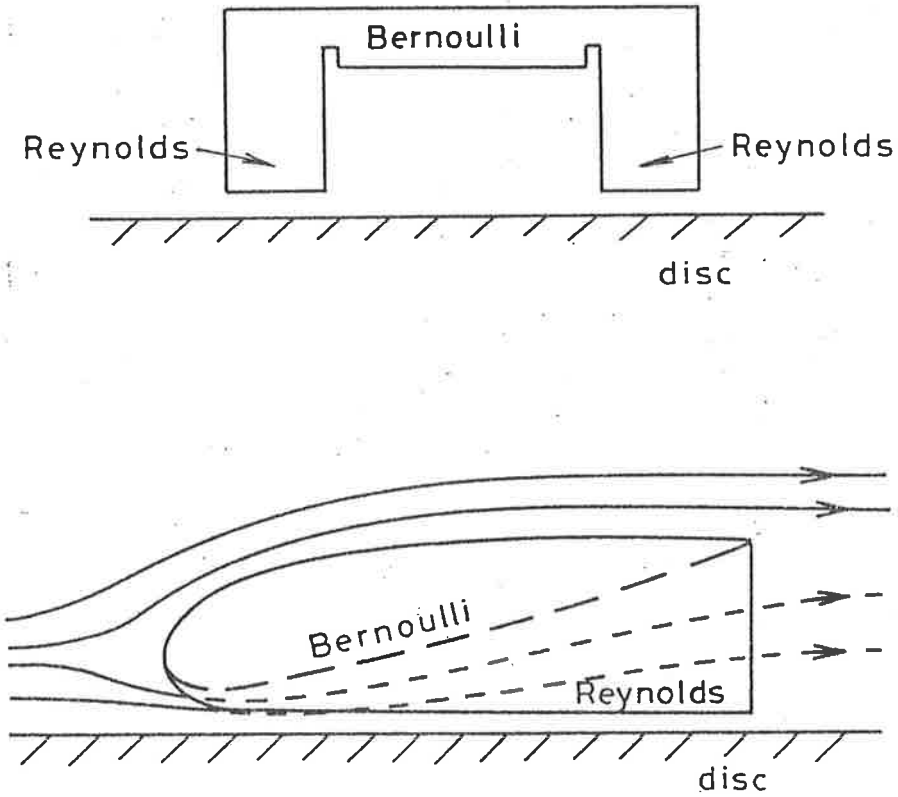

Figure 2.6 Sketch of computer disc head showing Reynolds portion and Bernoulli portion.

to provide the lubrication between the head and the disc, and the second, which could be of either sign, was chosen by Tuck to be negative. This means that the bridge is, in effect, a negative–lift wing in extreme ground effect.

When the disc is started up from rest, the Bernoulli forces are negligible. If the Reynolds portion has a positive angle of attack, the head will rise under positive Reynolds forces. This increases the Reynolds clearance, resulting in a reduction in the Reynolds forces, since these are proportional to the inverse cube of clearance. The proportional increase in the Bernoulli clearance will be much smaller and as the disc speed increases, the Bernoulli forces will become more significant. Since the Bernoulli portion of the head has a negative lift coefficient, its contribution to the net force will be a downward force. Thus, as the disc speed increases, the Bernoulli portion of the head keeps the disc head close to the disc surface.

In formulating the problem mathematically, Tuck balanced the forces acting on the head to obtain the simplified equation

$$M\frac{d^2}{dt^2}H(t) = -F + C_R U(t) H(t)^{-3} - C_B U(t)^2, \tag{2.18}$$

where $H(t)$ is the Reynolds clearance, M is the mass of the head, $U(t)$ is the speed of the disc and C_R and C_B are the coefficients for the Reynolds and Bernoulli forces respectively. The term F denotes the force of the spring which holds the head in position. If the two portions of the head are flat plates at small angles of attack α_R and $-\alpha_B$, then

$$C_R = \mu \alpha_R w_R L_R^3 \tag{2.19}$$

and

$$C_B = \frac{1}{2}\rho\alpha_B w_B L_B^2/h_B, \tag{2.20}$$

in which μ is the air viscosity, ρ is the air density, w and L denote widths and lengths of the respective portions and h_B is the Bernoulli clearance.

When the system crashes, the disc slows down and the head is dropped onto the disc. If we assume that the disc velocity U changes slowly, then the solution to equation (2.18) will be a small amplitude oscillation about a slowly varying mean. This slowly varying part is found by assuming that, for all time, the forces are balanced. The period of oscillation is obtained by linearizing about the local height and velocity values. We can show that the solution is of this form by expressing H as a power series in a small parameter ϵ; that is,

$$H = H_0 + H_1 + H_2 + \ldots, \tag{2.21}$$

in which the subscript indicates the power of ϵ. This series form is substituted into equation (2.18), and then, after equating powers of ϵ, we find that

$$H_0^3 = \frac{C_R U}{F + C_B U^2} \tag{2.22}$$

and

$$H_1 = A\cos(\omega t + \theta), \tag{2.23}$$

in which $\omega^2 = (3C_R U)/(MH_0^4)$ and θ is the unknown phase. The exponentially–decaying velocity is described by

$$U(t) = \exp(-\epsilon t). \tag{2.24}$$

As an example, we will solve this problem for a head weighing 10g. To determine the order of magnitude of the two force coefficients, we assume that the air has density 1.29 x 10^{-3} g/cm^3 and viscosity 1.7 x 10^{-4} g/cm sec (Batchelor (1970)). Suitable values for C_R and C_B are then 10^{-6} g cm^3/sec and 10^{-4} g/cm respectively. Of interest is the ratio γ between the Bernoulli coefficient C_B and the spring force F.

Figures 2.7, 2.8 and 2.9 show how the height of the head varies with time for different values of the ratio γ and ϵ. We can see that as ϵ increases, the time taken to crash decreases. The important feature shown in these figures is that when the aerodynamic force exceeds the spring force, the head initially rises as the velocity U decreases. It may then be possible to design a read–write head to take advantage of this increase in clearance to provide safer crashes.

2.3 Falling Flat Plate with Degree of Angular Freedom

Tuck (1980) derived a nonlinear, unsteady, one dimensional theory for the gap flow induced by a body moving in extreme ground effect. The flow is irrotational except for the vortex sheet representing the wake and as an illustration of the unsteady theory, he solved the problem of a flat plate falling towards the ground under its own weight without rotation (that is, remaining parallel to the ground), while moving forward at uniform speed.

In this section, we shall use this theory to solve a more general dynamical problem, namely for a flat plate at an angle of attack $\alpha(t)$ with lower surface

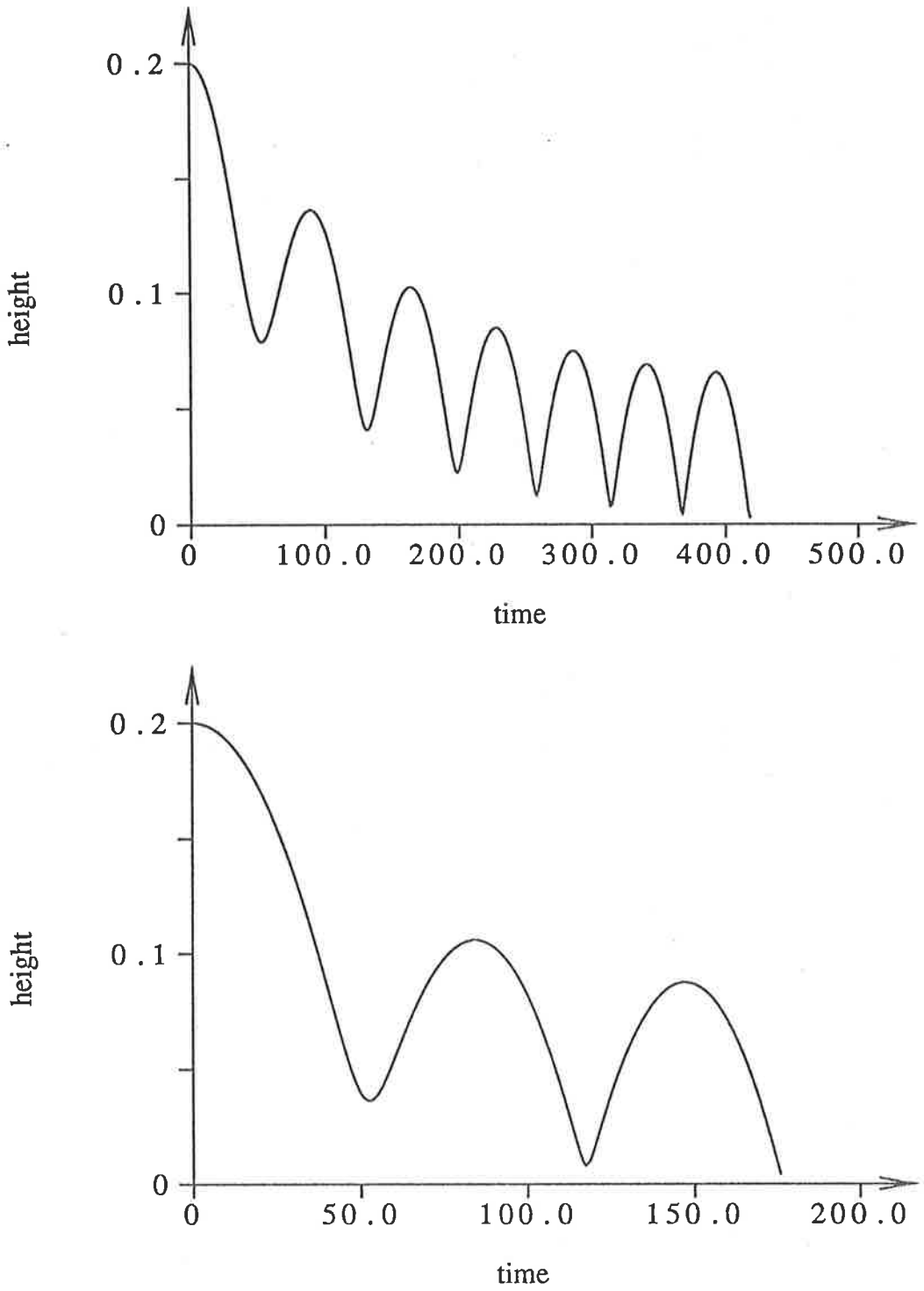

Figure 2.7 Plots of the height of the head against time. The top graph is for $\epsilon = 0.01$ and the lower graph is for $\epsilon = 0.025$. The ratio γ between the Bernoulli coefficient C_B and the spring force F is 0.2.

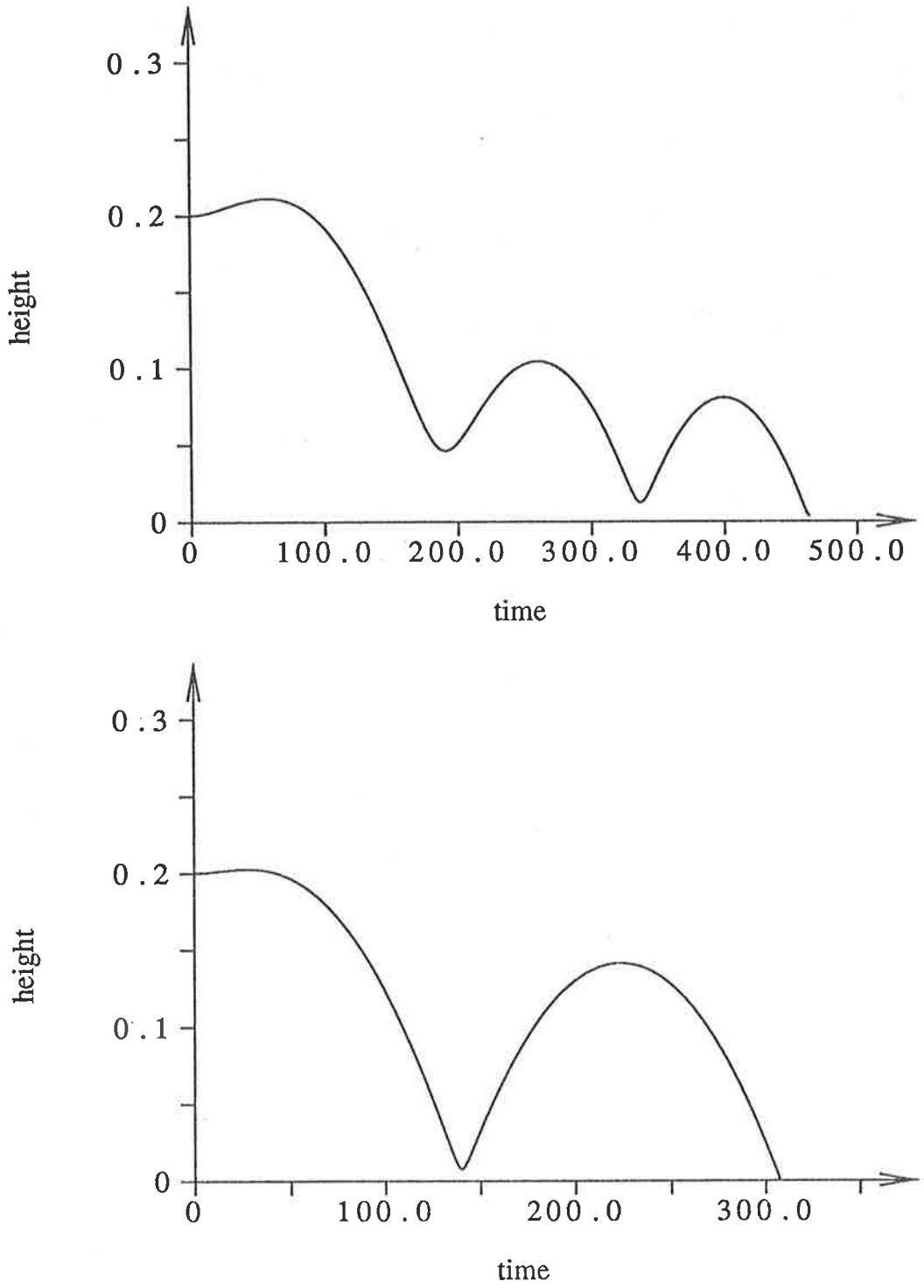

Figure 2.8 Plots of the height of the head against time. The top graph is for $\epsilon = 0.01$ and the lower graph is for $\epsilon = 0.025$. The ratio γ between the Bernoulli coefficient C_B and the spring force F is one.

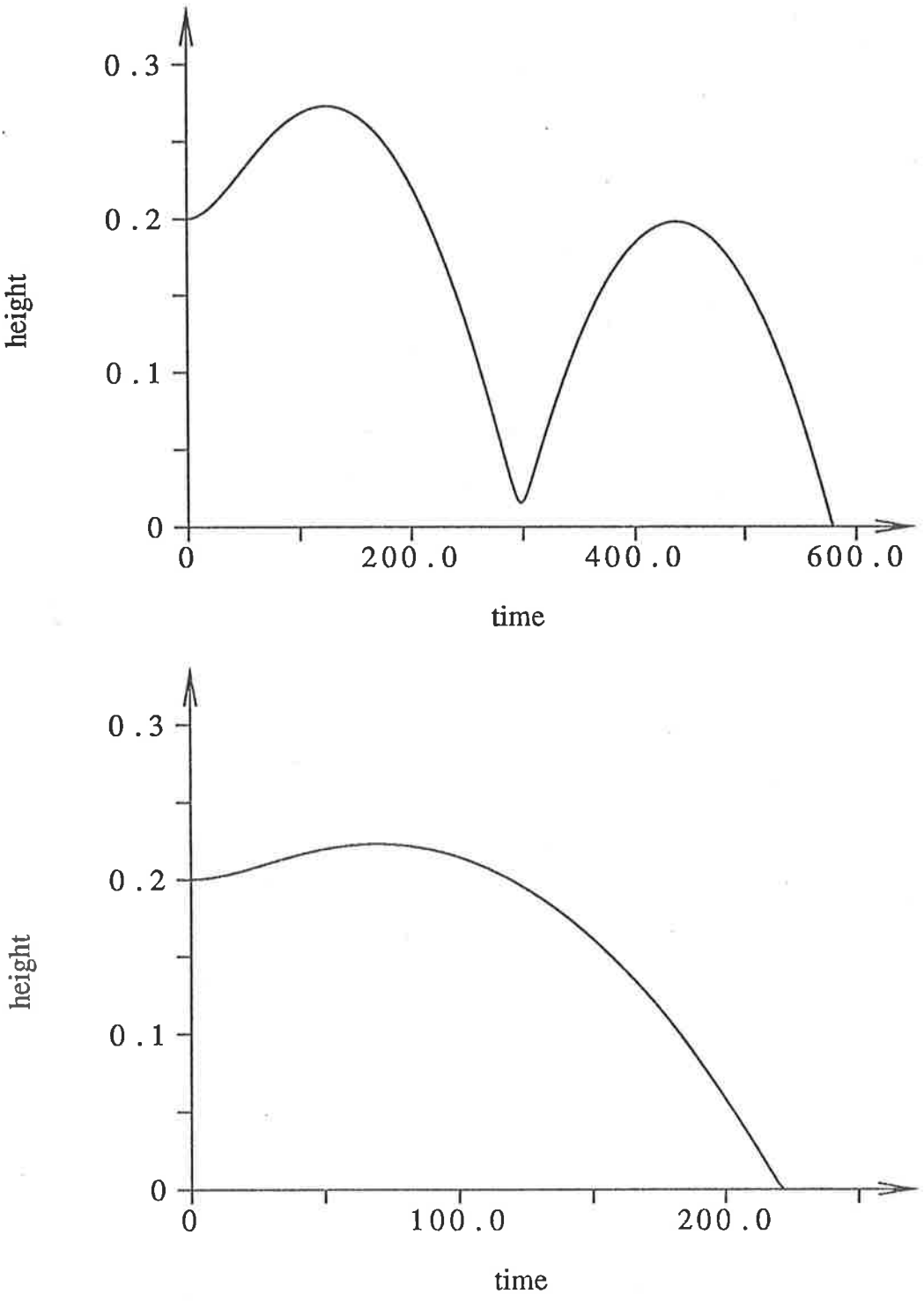

Figure 2.9 Plots of the height of the head against time. The top graph is for $\epsilon = 0.01$ and the lower graph is for $\epsilon = 0.025$. The ratio γ between the Bernoulli coefficient C_B and the spring force F is two.

$f^-(x,t)$ as illustrated in figure 2.10. This theory could be applied to problems such as computer disc heads flying above hard discs, the stacking of glass plates (Yih, 1974), or planes crashing from a low altitude.

We shall define the geometry of the problem in the following way. The leading edge or bow is at $x = x_L$ and the trailing edge or stern is at $x = x_T$. The plate is of length $2l = x_L - x_T$ and is everywhere close to a plane boundary at $y = 0$. Our task is to solve Laplace's equation

$$\frac{\partial^2 \phi}{\partial x^2} + \frac{\partial^2 \phi}{\partial y^2} = 0 \tag{2.25}$$

subject to appropriate boundary conditions. The first of these boundary conditions is that at infinity, the fluid must return to a state of rest; that is,

$$\phi, \nabla\phi \to 0 \qquad \text{as} \qquad x, y \to \infty. \tag{2.26}$$

The wall or ground plane at $y = 0$ is impermeable and, consequently, the second condition is that there is no flow normal to this wall:

$$\frac{\partial}{\partial y}\phi(x, 0, t) = 0. \tag{2.27}$$

The third condition, which applies on the moving body surface, requires that

$$\frac{\partial \phi}{\partial y} = \frac{\partial f}{\partial t} + \frac{\partial \phi}{\partial x}\frac{\partial f}{\partial x} \qquad \text{on} \qquad f = f^-. \tag{2.28}$$

The final condition results from applying the Kutta condition. The trailing edge $x = x_T$ is assumed to shed vortices which remain behind the body in a vortex sheet, with equation

$$y = f^W(x, t), \tag{2.29}$$

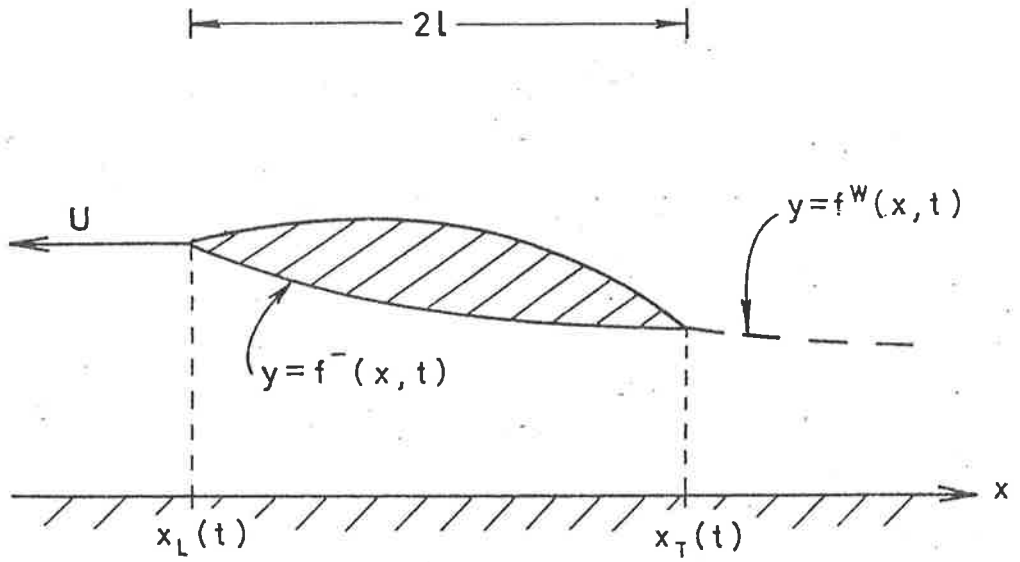

Figure 2.10 Sketch of flow situation and coordinate system for a thin body moving in extreme ground effect above the ground.

the function f^W being unknown. The kinematic boundary condition across the surface is given by equation (2.28) with $f = f^W$ and the dynamic condition is that the pressure must be continuous across the sheet. From Bernoulli's equation, $p(x, y, t)$, the excess of pressure over the value at infinity, is given by

$$p = -\rho\left(\frac{\partial\phi}{\partial t} + \frac{1}{2}\left[\frac{\partial\phi}{\partial x}\right]^2 + \frac{1}{2}\left[\frac{\partial\phi}{\partial y}\right]^2\right) \tag{2.30}$$

everywhere in the fluid. Thus the dynamic condition on the wake is

$$p(x, f^W + 0, t) = p(x, f^W - 0, t). \tag{2.31}$$

Equation (2.31) holds in the wake for $x > x_T(t)$ and also holds at the trailing edge $x_T(t)$, where it defines the Kutta condition.

Tuck found that the velocity potential ϕ for this one dimensional, unsteady problem is given by

$$\phi(x,t) = q(t)A(x,t) + B(x,t) \tag{2.32}$$

where $q(t)$ is the, as yet unknown, net flux through the gap at the stern,

$$A(x,t) = \int_{x_L(t)}^{x} \frac{d\xi}{f^-(\xi,t)} \tag{2.33}$$

and

$$B(x,t) = \int_{x_L(t)}^{x} \frac{d\xi}{f^-(\xi,t)} \int_{\xi}^{x_T(t)} \frac{\partial}{\partial t} f^-(\xi^*,t)d\xi^*. \tag{2.34}$$

In the gap and the wake, Bernoulli's equation (2.30) simplifies to

$$p = -\rho\left(\frac{\partial\phi}{\partial t} + \frac{1}{2}\left[\frac{\partial\phi}{\partial x}\right]^2\right), \tag{2.35}$$

as $\frac{\partial \phi}{\partial y} = \mathrm{O}(\epsilon)$. Outside the gap and the wake, the velocity potential ϕ is $\mathrm{O}(\epsilon)$ and therefore the pressure $p = \mathrm{O}(\epsilon)$. Hence, for continuity of p across the wake, we require that

$$\frac{\partial \phi}{\partial t} + \frac{1}{2}\left[\frac{\partial \phi}{\partial x}\right]^2 = 0, \quad x \geq x_T(t). \tag{2.36}$$

When we substitute the velocity potential (2.32) into this Kutta condition, we obtain the nonlinear, first–order ordinary differential equation defined at $x = x_T$

$$A(x,t)\frac{dq}{dt} + q\frac{d}{dt}A(x,t) + \frac{d}{dt}B(x,t) + \frac{q^2}{2f^2(x,t)} = 0. \tag{2.37}$$

We now assume that the lower surface of the body is of the form

$$f^{-}(x,t) = y_0(t) - \alpha(t)\,(x + Ut)\,, \tag{2.38}$$

thereby allowing a degree of angular freedom, and that there is uniform horizontal translation to the left at speed U; that is $x_L(t) = -l - Ut$, $x_T(t) = l - Ut$, with U constant. From equation (2.33), we find $A(x,t)$ to be given by

$$A(x,t) = -\frac{1}{\alpha}\log\left|\frac{y_0 - \alpha(x + Ut)}{y_0 + \alpha l}\right|, \tag{2.39}$$

and from equation (2.34), that $B(x,t)$ is of the form

$$\begin{aligned} B(x,t) =& \frac{1}{\alpha}\left([x + l + Ut] - A[y_0 - \alpha l]\right)(\dot{y}_0 - \alpha U) \\ &+ \frac{\dot{\alpha}}{\alpha^2}\left(\frac{1}{2}A[y_0^2 - \alpha^2 l^2] - \frac{1}{4}[x + l + Ut][2y_0 + \alpha(x + Ut - l)]\right), \end{aligned} \tag{2.40}$$

in which $A = A(x,t)$, $\alpha = \alpha(t)$, $y_0 = y_0(t)$ and $\dot{}$ refers to differentiating with respect to t. We can express $B(x,t)$ more concisely as

$$B(x,t) = B_{\dot{y}_0}(\dot{y}_0 - \alpha U) + B_{\dot{\alpha}}\dot{\alpha}, \tag{2.41}$$

where $B_{\dot{y}_0}$ denotes the coefficient of the $\dot{y}_0$ term:

$$B_{\dot{y}_0} = \frac{1}{\alpha}([x + l + Ut] - A[y_0 - \alpha l]) \tag{2.42}$$

and $B_{\dot{\alpha}}$ denotes the coefficient of the $\dot{\alpha}$ term:

$$B_{\dot{\alpha}} = \frac{1}{4\alpha^2}\Big(2A\left[y_0^2 - \alpha^2 l^2\right] - \left[x + l + Ut\right]\left[2y_0 + \alpha(x + Ut - l)\right]\Big). \tag{2.43}$$

Therefore, the velocity potential (2.32) becomes

$$\phi = q(t)A + B_{\dot{y}_0}(\dot{y}_0 - \alpha U) + B_{\dot{\alpha}}\dot{\alpha}. \tag{2.44}$$

This form for the velocity potential ϕ can be substituted into equation (2.35) to get the following equation for the pressure:

$$\begin{aligned} p &= -\rho\Big(\dot{A}q + A\dot{q} + \dot{B} + \frac{1}{2}\left(q\frac{\partial A}{\partial x} + \frac{\partial B}{\partial x}\right)^2\Big) \\ &= -\rho\Big(\dot{A}q + A\dot{q} + (\ddot{y}_0 - \dot{\alpha}U)B_{\dot{y}_0} + (\dot{y}_0 - \alpha U)\dot{B}_{\dot{y}_0} + \ddot{\alpha}B_{\dot{\alpha}} \\ &\qquad + \dot{\alpha}\dot{B}_{\dot{\alpha}} + \frac{1}{2}\left(q\frac{\partial A}{\partial x} + \frac{\partial B}{\partial x}\right)^2\Big), \end{aligned} \tag{2.45}$$

where $\ddot{}$ refers to differentiating twice with respect to t, $\dot{A}$ is $\partial A/\partial t$, $\dot{B}_{\dot{y}_0}$ denotes the time derivative of the $B_{\dot{y}_0}$ term and $\dot{B}_{\dot{\alpha}}$ denotes the time derivative of the $B_{\dot{\alpha}}$ term. We find that these three time derivatives are given by

$$\dot{A} = -\frac{\dot{\alpha}}{\alpha}A + \frac{1}{\alpha}\left(\frac{\dot{y}_0 + \dot{\alpha}l}{y_0 + \alpha l}\right) - \frac{1}{\alpha}\left(\frac{\dot{y}_0 - \dot{\alpha}(x + Ut) - \alpha U}{y_0 - \alpha(x + Ut)}\right), \tag{2.46}$$

$$\dot{B}_{\dot{y}_0} = -\frac{\dot{\alpha}}{\alpha}B_{\dot{y}_0} - \frac{1}{\alpha}\Big[(\dot{y}_0 - l\dot{\alpha})A + (y_0 - \alpha l)\dot{A} - U\Big] \tag{2.47}$$

and

$$\dot{B}_{\dot{\alpha}} = \frac{1}{\alpha^2}\Big(A(y_0\dot{y}_0 - \alpha\dot{\alpha}l^2) + \frac{1}{2}(y_0^2 - \alpha^2 l^2)\dot{A} - \frac{1}{4}\left[x + Ut + l\right]\left[\dot{\alpha}(x + Ut - l) + 2\dot{y}_0 + \alpha U\right] - \frac{U}{4}\left[2y_0 + \alpha(x + Ut - l)\right]\Big) - \frac{2\dot{\alpha}}{\alpha}B_{\dot{\alpha}}. \tag{2.48}$$

Similarly, the terms $\frac{\partial A}{\partial x}$ and $\frac{\partial B}{\partial x}$ are given by

$$\frac{\partial A}{\partial x} = \frac{1}{y_0 - \alpha(x + Ut)} \tag{2.49}$$

and

$$\frac{\partial B}{\partial x} = \frac{2(\dot{y}_0 - U\alpha)(l - x - Ut) + \dot{\alpha}l^2 + \dot{\alpha}(x + Ut)^2}{2[y_0 - \alpha(x + Ut)]}. \tag{2.50}$$

At the stern, the pressure residue must vanish and so the right hand side of equation (2.45) must also vanish, giving the required Kutta condition at $x = x_T(t)$.

Using our pressure equation (2.45), we can determine the net upward force by balancing the forces acting on the body; that is,

$$\int p\ dx = m(\ddot{y}_0 + g), \tag{2.51}$$

in which m represents the mass of the plate and g represents gravity. In the same way, the moment equation is found to be

$$\int xp\ dx = I\ddot{\alpha}, \tag{2.52}$$

where I is the moment of inertia of the plate's mass.

If we assume for now that q, $\dot{y}_0$ and $\dot{\alpha}$ are known, then equations (2.45), (2.51) and (2.52) can be considered as a set of coupled equations in $\dot{q}$, $\ddot{y}_0$ and $\ddot{\alpha}$

and can be written in matrix form as

$$C\mathbf{y} = \mathbf{h}, \tag{2.53}$$

where

$$C = \begin{pmatrix} A & B_{\dot{y}_0} & B_{\dot{\alpha}} \\ \int A dx & \frac{m}{\rho} + \int B_{\dot{y}_0} dx & \int B_{\dot{\alpha}} dx \\ \int xA dx & \int xB_{\dot{y}_0} dx & \int xB_{\dot{\alpha}} dx - \frac{I}{\rho} \end{pmatrix}, \tag{2.54}$$

$$\mathbf{y} = \begin{pmatrix} \dot{q} \\ \ddot{y}_0 \\ \ddot{\alpha} \end{pmatrix} \tag{2.55}$$

and

$$\mathbf{h} = \begin{pmatrix} P(x) \\ \int P(x)dx - \frac{mg}{\rho} \\ \int xP(x)dx \end{pmatrix} \tag{2.56}$$

in which

$$P(x) = -\dot{A}q + B_{\dot{y}_0}\dot{\alpha}U - \dot{B}_{\dot{y}_0}\dot{y}_0 + \alpha U\dot{B}_{\dot{y}_0} - \dot{B}_{\dot{\alpha}}\dot{\alpha} - \frac{1}{2}(qA_x + B_x)^2. \tag{2.57}$$

We can solve this system of equations for the unknowns $\dot{q}$, $\ddot{y}_0$ and $\ddot{\alpha}$ and the resulting formulae represent a fifth-order system of differential equations for our fundamental unknowns q, y_0, α, $\dot{y}_0$ and $\dot{\alpha}$.

We divide the region beneath the body $[-l-Ut, l-Ut]$ into N subintervals and discretize t as follows:

$$t_{n+1} = t_n + \Delta t, \qquad n = 0, 1, 2, \ldots \tag{2.58}$$

where Δt is a small, constant step in time. We select suitable initial values for the parameters α, y_0, $\dot{\alpha}$, $\dot{y}_0$ and q, and for these initial values, compute A, $B_{\dot{\alpha}}$ and $B_{\dot{y}_0}$ at each x_i beneath the body; that is, at

$$x_i = -l + i\frac{2l}{N} - Ut, \qquad i = 0, \ldots, N. \tag{2.59}$$

With these terms now known, the entries in the matrix C and the vector $\mathbf{h}$ can be evaluated using, where necessary, the trapezoidal rule for integration.

Our task is to solve the matrix equation (2.53) for $\dot{q}$, $\ddot{y}_0$ and $\ddot{\alpha}$ and this can be done quite easily using the packaged (IMSL) routine "LEQT2F". When we have found these unknowns, we apply the Euler–Cauchy method to our problem to solve for our initial parameters at the next time step in the following way:

$$\dot{y}_{0n+1} = \dot{y}_{0n} + \Delta t\ \ddot{y}_{0n}, \tag{2.60}$$

$$\dot{\alpha}_{n+1} = \dot{\alpha}_n + \Delta t\ \ddot{\alpha}_n, \tag{2.61}$$

$$q_{n+1} = q_n + \Delta t\ \dot{q}_n, \tag{2.62}$$

$$y_{0n+1} = y_{0n} + \Delta t\ \dot{y}_{0n}, \tag{2.63}$$

and

$$\alpha_{n+1} = \alpha_n + \Delta t\ \dot{\alpha}_n, \tag{2.64}$$

where the subscript n refers to the time level. At each step in time, we must check to see if the body has landed; that is, if it has touched the ground. If $y_0(t) + \alpha(t)l \leq 0$, then the leading edge has hit the ground and if $y_0(t) - \alpha(t)l \leq 0$,

then the trailing edge has touched the ground. In this way, we can determine the length of time in flight, the rate of descent, the flux at the trailing edge and the way in which the angle of attack affects the flight of the body.

We present some results for this problem in figures 2.11 and 2.12. The variables in these figures have been non–dimensionalized. The scale factors are those described by Tuck (1980); namely, time was scaled with $T = \sqrt{2h/g}$, the time taken to fall a distance h in a vacuum, y_0 was scaled with h, x with l, U with l/T and m with $\rho l^3/h$.

In figure 2.11, we consider a plate starting from rest at (scaled) height $y_0 = 1.0$ with a positive angle of attack $\alpha = 0.1$. We plot the length of (scaled) time in flight versus the scaled mass of the plate for various values of the scaled horizontal velocity U. It is clear that as the horizontal velocity U increases, the length of time in flight decreases. This result is not surprising since a plate's rate of rotation increases with the velocity of that plate. A more striking feature illustrated in figure 2.11, is that it is possible for the plate to fly forever. For almost all values of the scaled mass, the plate lands trailing edge down. However, if the scaled mass is sufficiently small, the plate continues to rises at constant angle of attack.

In figure 2.12, we determine how the length of time in flight changes with the initial angle of attack. The plate, which is of scaled mass $m = 1.0$, starts from rest at height $y_0 = 1.0$ and we consider two different values of the horizontal velocity, namely $U = 5.0$ and $U = 10.0$. Once again, the time in flight decreases

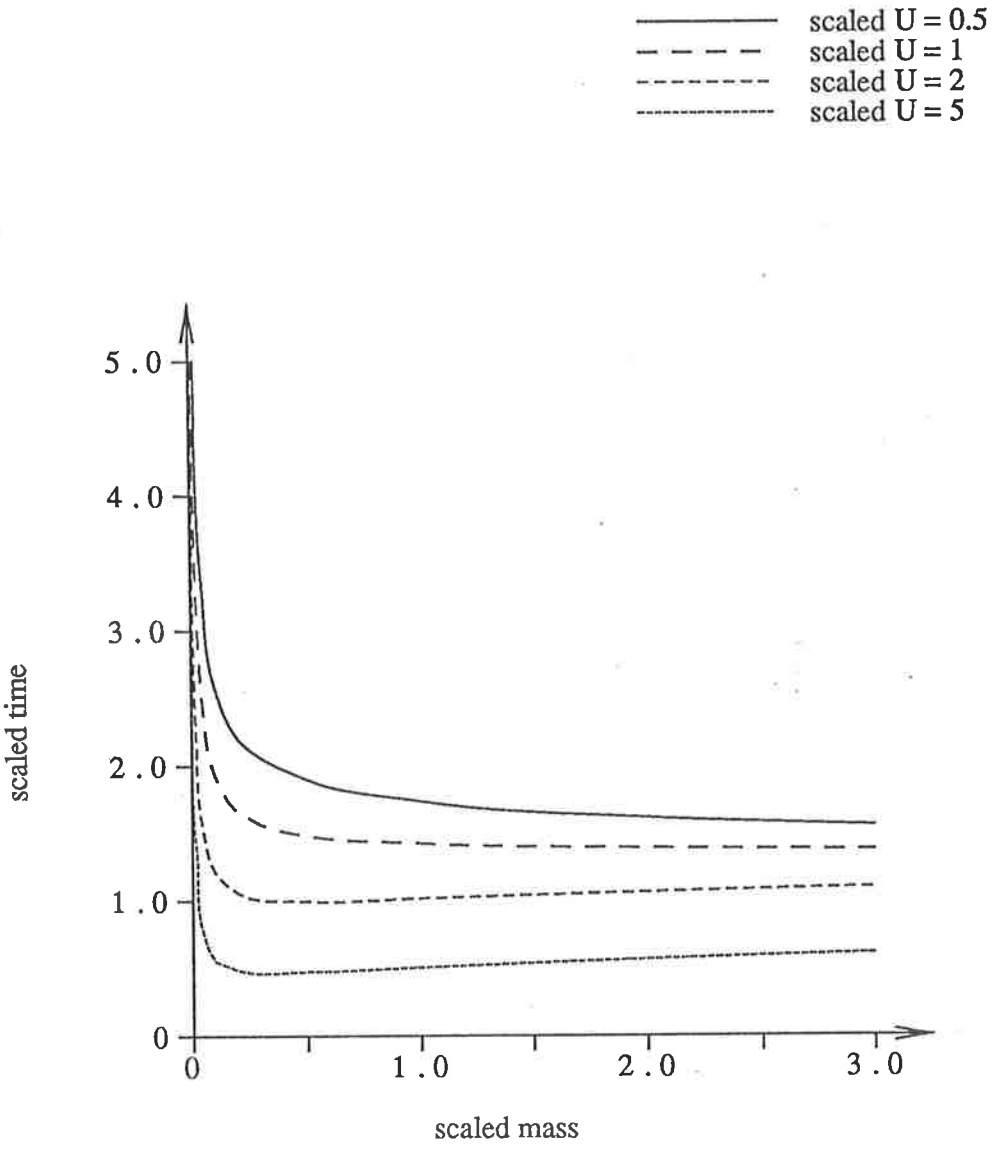

Figure 2.11 Plots of the scaled time taken for a plate to fall to the ground versus the scaled mass of the plate for various scaled horizontal speeds. In each case, the initial scaled height y_0 was one and the initial value of α was 0.1.

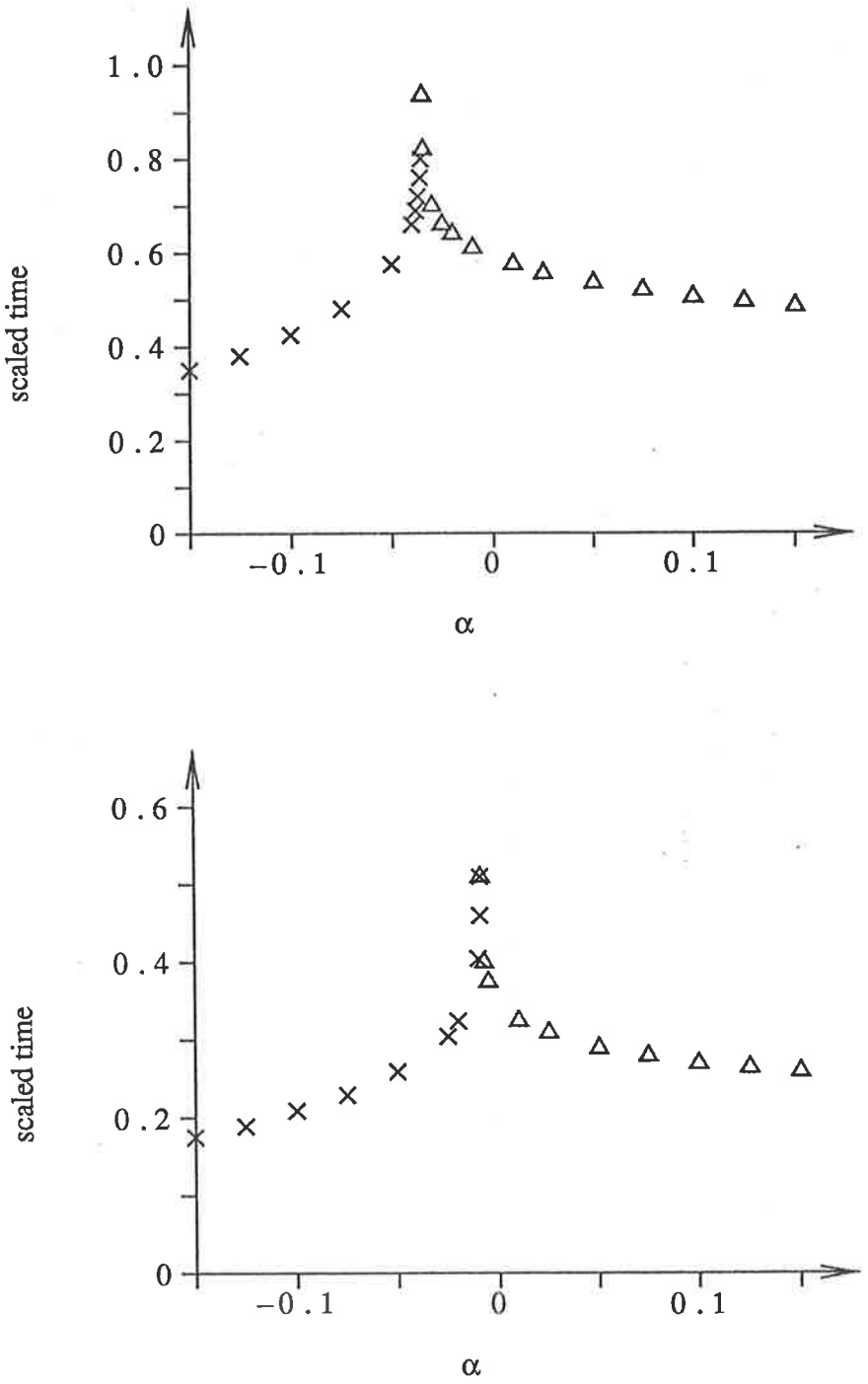

Figure 2.12 Plots of scaled time taken for a plate of scaled mass $m = 1.0$ to fall to the ground versus the initial angle of attack. In each case, the scaled initial height y_0 was one. The scaled horizontal velocity took the value five in the top graph and ten in the lower graph. The crosses indicate that the plate landed leading edge first and the triangles indicate that the plate landed trailing edge first.

as the horizontal velocity increases. We also note that as the magnitude of α increases, the length of time in flight decreases. The main feature illustrated in figure 2.12 is that there is a narrow range of values for α for which the flight time is significantly increased. In both examples, this occurs at very small negative angles of attack when the plate is flying almost parallel to the ground. For values of α below this critical range, the plate lands leading edge first and for values above this range, the plate lands trailing edge first.

In conclusion, it would appear from our results that, in general, a plate moving close to the ground with positive angle of attack will land trailing edge down. And conversely, a plate with negative angle of attack, will land leading edge down. However, as previously mentioned, there are two cases when this may not be true. The first of these is when the plate is initially almost parallel to the ground and the second is when the plate has a small scaled mass.

CHAPTER 3

DERIVATION OF THE TWO DIMENSIONAL GAP FLOW EQUATIONS

In this chapter, we examine the three dimensional, steady, irrotational flow of air past a thin body of general planform situated close to a plane surface. We assume that the air is inviscid and incompressible, and that the flow geometry, as illustrated in figures 3.1 and 3.2, is such that the non–uniform clearance of the body from the ground is small, $O(\epsilon)$, compared to its length. Our aim is to model some aspects of the aerodynamics of a body moving in such extreme ground effect.

We shall choose a frame of reference in which the body is fixed, relative to the ground, in a stream of air moving with velocity U. The upper surface of the body is given by $z = f^+(x, y)$ and the lower surface by $z = f^-(x, y)$.

3.1 The Governing Equations

Our task is to determine the velocity potential $\phi = \phi(x, y, z)$, which satisfies Laplace's equation; that is,

$$\frac{\partial^2 \phi}{\partial x^2} + \frac{\partial^2 \phi}{\partial y^2} + \frac{\partial^2 \phi}{\partial z^2} = 0 \tag{3.1}$$

(almost) everywhere in the flow region, subject to the following boundary conditions:

$$\phi \to Ux \qquad \text{at} \quad \infty, \tag{3.2}$$

that is, once the flow has past the body, it returns to a uniform stream;

$$\frac{\partial \phi}{\partial z} = 0 \qquad \text{on} \quad z = 0, \tag{3.3}$$

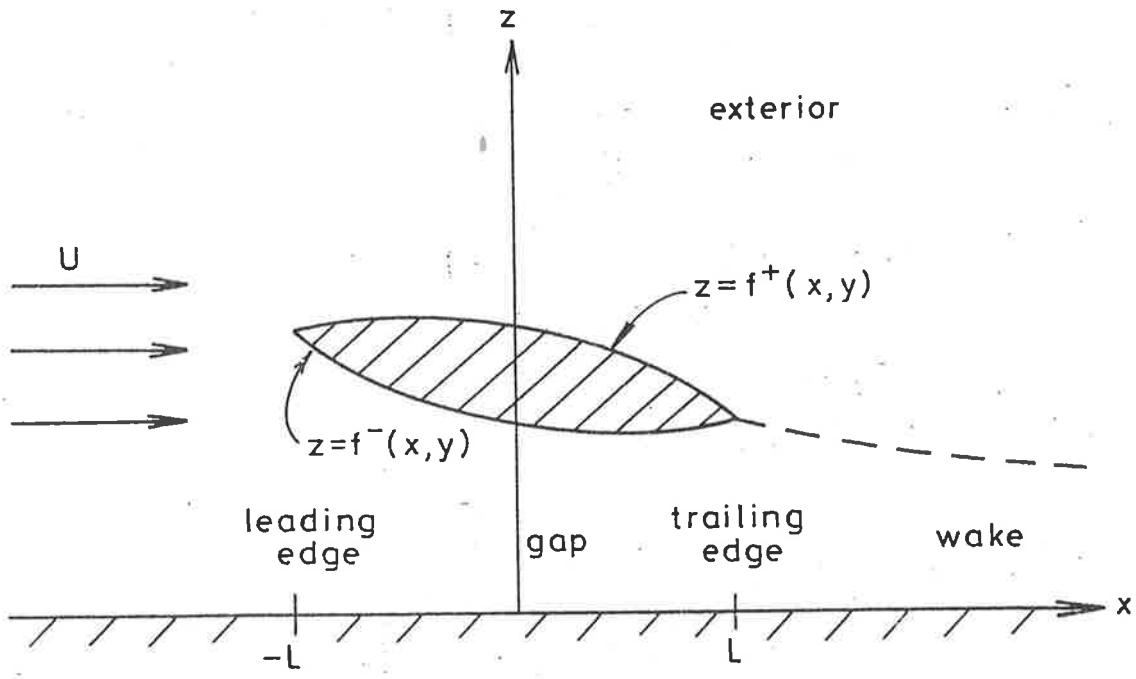

Figure 3.1 Side–on view of flow geometry and coordinate system.

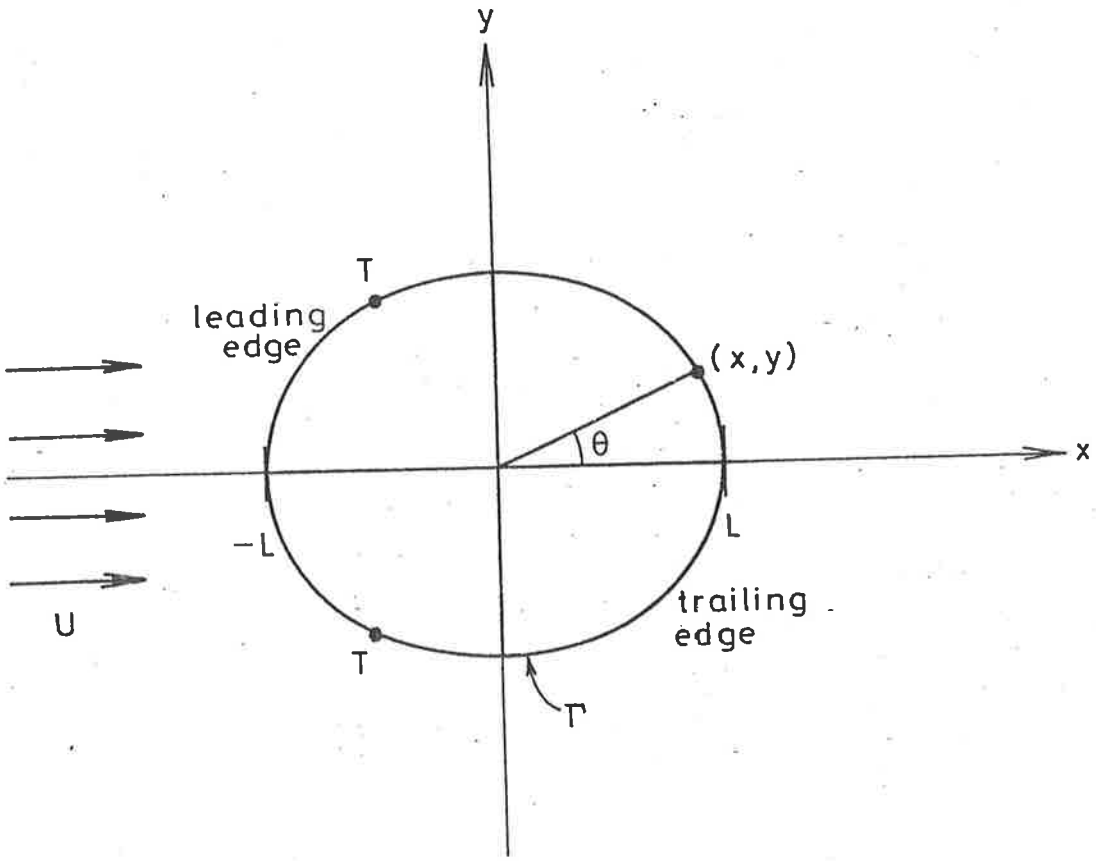

Figure 3.2 Planview of flow geometry and coordinate system.

that is, the ground is impermeable;

$$\frac{\partial \phi}{\partial z} = \frac{\partial \phi}{\partial x}\frac{\partial f^+}{\partial x} + \frac{\partial \phi}{\partial y}\frac{\partial f^+}{\partial y} \qquad \text{on} \quad z = f^+, \tag{3.4a}$$

and

$$\frac{\partial \phi}{\partial z} = \frac{\partial \phi}{\partial x}\frac{\partial f^-}{\partial x} + \frac{\partial \phi}{\partial y}\frac{\partial f^-}{\partial y} \qquad \text{on} \quad z = f^-; \tag{3.4b}$$

that is, the body is also impermeable.

Intuitively, the net disturbance to the uniform stream is small almost everywhere, since the body is thin and the clearance is $O(\epsilon)$; thus, almost everywhere

$$\phi = Ux + O(\epsilon). \tag{3.5}$$

It remains now to solve the flow problem in the region where this is not true; that is, in the gap.

In the limit as $\epsilon \to 0$ and setting in that limit $f(x,y) = f^-(x,y) = f^+(x,y)$, Tuck (1983) derived the partial differential equation which governs the two dimensional flow under the body

$$\frac{\partial}{\partial x}\left(f\frac{\partial \phi}{\partial x}\right) + \frac{\partial}{\partial x}\left(f\frac{\partial \phi}{\partial y}\right) = 0, \tag{3.6}$$

subject to the leading edge boundary condition

$$\phi = Ux, \tag{3.7}$$

and the trailing edge boundary condition

$$\left[\frac{\partial \phi}{\partial x}\right]^2 + \left[\frac{\partial \phi}{\partial y}\right]^2 = U^2, \tag{3.8}$$

although no derivation was given of equations (3.7) or (3.8).

Before using these results to solve the gap–region flow problem, we shall formally prove that the boundary conditions used by Tuck are correct. To do this, we must match the gap flow to the exterior flow. As $\epsilon \to 0$, this can be done by dividing the flow region into appropriate sub–regions: the exterior region, the gap region, the wake region and the edge region. This last region must be considered in two sections – the leading edge and the trailing edge. Physically, the leading edge is the section where fluid passes from outside the perimeter of the body, denoted by Γ, to inside the perimeter of the body and this occurs wherever the normal component of the mean horizontal plane velocity is negative. The opposite is true for the trailing edge. The points T at the junctions of the two types of edge regions are known as transition points and satisfy the conditions for both regions. Therefore, to match the gap flow to the exterior flow, we shall divide the flow region into the following sub–regions (as illustrated in figures 3.1, 3.2 and 3.3):

(a) the exterior region E: $x = O(L)$, $y = O(L)$, $z = O(L)$

(b) the gap region G: $x = O(L)$, $y = O(L)$, $z = O(\epsilon)$

(c) the wake W: $x = O(L)$, $y = O(L)$, $z = O(\epsilon)$

(d) the leading edge L: $x - X_L(l) = O(\epsilon)$, $y - Y_L(l) = O(\epsilon)$, $z = O(\epsilon)$

(e) the trailing edge T: $x - X_L(l) = O(\epsilon)$, $y - Y_L(l) = O(\epsilon)$, $z = O(\epsilon)$.

The appropriate equations are obtained by the method of matched asymp-

totic expansions (Van Dyke (1964)). In each region, we represent the velocity potential by an asymptotic expansion; that is, $\phi = \phi_0 + \phi_1 + \phi_2 + \ldots$ where the subscript indicates an ordering with respect to powers of ϵ. A superscript, for example E for exterior, will be used to identify the region concerned. We now consider each region in turn.

3.2 The Exterior Region

The series form for the potential ϕ is given by

$$\phi^E = \phi_0^E + \phi_1^E + \phi_2^E + \ldots \quad . \tag{3.9}$$

The full Laplace equation (3.1) holds for all terms in the exterior expansion as does the boundary condition at infinity (3.2). The boundary condition on the body yields, after equating powers in ϵ

$$\frac{\partial \phi_0^E}{\partial z} = 0, \tag{3.10a}$$

and

$$\frac{\partial \phi_1^E}{\partial z} = \frac{\partial \phi_0^E}{\partial x}\frac{\partial f}{\partial x} + \frac{\partial \phi_0^E}{\partial y}\frac{\partial f}{\partial y}. \tag{3.10b}$$

The leading order potential ϕ_0^E has the unique solution $\phi_0^E = Ux$ unless there is a contribution from singularities (sources and sinks), which model the edge Γ of the body and the disturbance to the uniform stream by the body. This will only occur if the sources and sinks are of O(1) strength as $\epsilon \to 0$. However, any such flux squeezes through a gap of $O(\epsilon)$ and must then have edge and gap velocities of $O(\epsilon^{-1})$. These velocities would tend to infinity as ϵ approached zero and this is

physically unacceptable. Hence, the singularities are at most $O(\epsilon)$ and only affect ϕ_1^E. Thus,

$$\phi^E = Ux + \phi_1^E, \tag{3.11}$$

and

$$\frac{\partial}{\partial z}\phi_1^E(x, y, 0^+) = U\frac{\partial}{\partial x}f(x, y). \tag{3.12}$$

3.3 The Gap Region

The velocity potential ϕ in this region is

$$\phi^G = \phi_0^G + \phi_1^G + \phi_2^G + \dots \quad . \tag{3.13}$$

In the gap region, the vertical coordinate z must be stretched relative to the plane coordinates x and y; that is, $z = O(\epsilon)$ and $\frac{\partial}{\partial z} = O(\epsilon^{-1})$. We substitute the asymptotic expansions for ϕ^G into Laplace's equation (3.1) and equate like powers of ϵ, giving

$$\frac{\partial^2 \phi_0^G}{\partial z^2} = 0, \tag{3.14a}$$

$$\frac{\partial^2 \phi_1^G}{\partial z^2} = 0, \tag{3.14b}$$

$$\frac{\partial^2 \phi_2^G}{\partial z^2} = -\frac{\partial^2 \phi_0^G}{\partial x^2} - \frac{\partial^2 \phi_0^G}{\partial y^2}. \tag{3.14c}$$

Since $\frac{\partial \phi}{\partial z} = 0$ on $z = 0$, the solutions to the first two equations are simply functions of x and y. Therefore,

$$\phi_0^G = \phi_0^G(x, y), \tag{3.15a}$$

and

$$\phi_1^G = \phi_1^G(x, y), \tag{3.15b}$$

and the third equation has the solution

$$\phi_2^G = \phi_2^G(x,y,0) - \frac{1}{2}z^2\left(\frac{\partial^2}{\partial x^2}\phi_0^G(x,y) + \frac{\partial^2}{\partial y^2}\phi_0^G(x,y)\right). \tag{3.15c}$$

Similarly, the boundary condition (3.4) yields

$$\frac{\partial \phi_0^G}{\partial z} = 0, \tag{3.16a}$$

$$\frac{\partial \phi_1^G}{\partial z} = 0, \tag{3.16b}$$

and

$$\frac{\partial \phi_2^G}{\partial z} = \frac{\partial \phi_0^G}{\partial x}\frac{\partial f}{\partial x} + \frac{\partial \phi_0^G}{\partial y}\frac{\partial f}{\partial y}. \tag{3.16c}$$

The first two of these conditions are clearly satisfied and the third is satisfied if, and only if, equation (3.6), derived less formally by Tuck, holds.

3.4 The Wake Region

The series form for the potential ϕ in the wake is

$$\phi^W = \phi_0^W + \phi_1^W + \phi_2^W + \ldots \quad . \tag{3.17}$$

There is no formal difference between the wake region and the gap region except for the fact that the boundary surface $z = f^W(x,y)$ is unknown. This is because the wake trailing from a thin body will itself be thin. Thus Laplace's equation (3.1) holds everywhere except within a wake of vanishing thickness which becomes a vortex sheet. This vortex sheet must be such that there is no pressure jump across it. The wake condition of zero pressure jump must also hold at the trailing edge – this condition being the Kutta condition.

Thus the same solutions apply to the wake as for the gap:

$$\phi_0^W = \phi_0^W(x,y), \tag{3.18a}$$

$$\phi_1^W = \phi_1^W(x,y), \tag{3.18b}$$

$$\phi_2^W = \phi_2^W(x,y,0) - \frac{1}{2}z^2\left(\frac{\partial^2}{\partial x^2}\phi_0^W(x,y) + \frac{\partial^2}{\partial y^2}\phi_0^W(x,y)\right), \tag{3.18c}$$

subject to

$$\frac{\partial}{\partial x}\left(f^W\frac{\partial\phi}{\partial x}\right) + \frac{\partial}{\partial y}\left(f^W\frac{\partial\phi}{\partial y}\right) = 0. \tag{3.19}$$

If we consider Bernoulli's equation

$$\frac{p}{\rho} + \frac{1}{2}\left(\left[\frac{\partial\phi}{\partial x}\right]^2 + \left[\frac{\partial\phi}{\partial y}\right]^2 + \left[\frac{\partial\phi}{\partial z}\right]^2\right) = \frac{p_\infty}{\rho} + \frac{1}{2}U^2, \tag{3.20}$$

then the condition on the wake

$$p(x,y,f^W+0) = p(x,y,f^W-0) \tag{3.21}$$

implies that

$$\frac{1}{2}U^2 + O(\epsilon) = \frac{1}{2}\left(\left[\frac{\partial}{\partial x}\phi_0^W(x,y)\right]^2 + \left[\frac{\partial}{\partial y}\phi_0^W(x,y)\right]^2\right) + O(\epsilon) \tag{3.22}$$

or

$$\left[\frac{\partial}{\partial x}\phi_0^W(x,y)\right]^2 + \left[\frac{\partial}{\partial y}\phi_0^W(x,y)\right]^2 = U^2; \tag{3.23}$$

that is, we substitute the exterior region expansion into the left hand side of equation (3.21) and the wake region expansion into the right hand side, assuming pressure to be continuous.

3.5 The Leading Edge Region

In this region, we define a stretched coordinate system (τ, η, ζ) as follows:

$$x = X_L(l) - \frac{h_0}{\epsilon}\tau \sin\theta_l + h_0\eta\cos\theta_l, \tag{3.24a}$$

$$y = Y_L(l) + \frac{h_0}{\epsilon}\tau \cos\theta_l + h_0\eta\sin\theta_l, \tag{3.24b}$$

$$z = h_0\zeta, \tag{3.24c}$$

where $h_0 = f(X_L(l), Y_L(l), 0) = O(\epsilon)$ and θ_l is the angle between the local normal at $(X_L(l), Y_L(l), 0)$ and the x–axis. (See figure 3.3). The full Laplace equation (3.1) must now be written in terms of these new variables and becomes

$$\epsilon^2\frac{\partial^2\phi}{\partial\tau^2} + \frac{\partial^2\phi}{\partial\eta^2} + \frac{\partial^2\phi}{\partial\zeta^2} = 0. \tag{3.25}$$

For the flow in the leading edge region, we substitute the velocity potential in its series form

$$\phi^L = \phi_0^L + \phi_1^L + \phi_2^L + \ldots \tag{3.26}$$

into Laplace's equation (3.25) and, after equating like powers of ϵ, this yields

$$\frac{\partial^2\phi_0^L}{\partial\eta^2} + \frac{\partial^2\phi_0^L}{\partial\zeta^2} = 0. \tag{3.27a}$$

$$\frac{\partial^2\phi_1^L}{\partial\eta^2} + \frac{\partial^2\phi_1^L}{\partial\zeta^2} = 0. \tag{3.27b}$$

$$\epsilon^2\frac{\partial^2\phi_0^L}{\partial\tau^2} + \frac{\partial^2\phi_2^L}{\partial\eta^2} + \frac{\partial^2\phi_2^L}{\partial\zeta^2} = 0. \tag{3.27c}$$

The boundary equation (3.3) on $z = 0$ gives

$$\frac{\partial\phi_m^L}{\partial\zeta} = 0, \qquad m = 0, 1, 2, \ldots \tag{3.28}$$

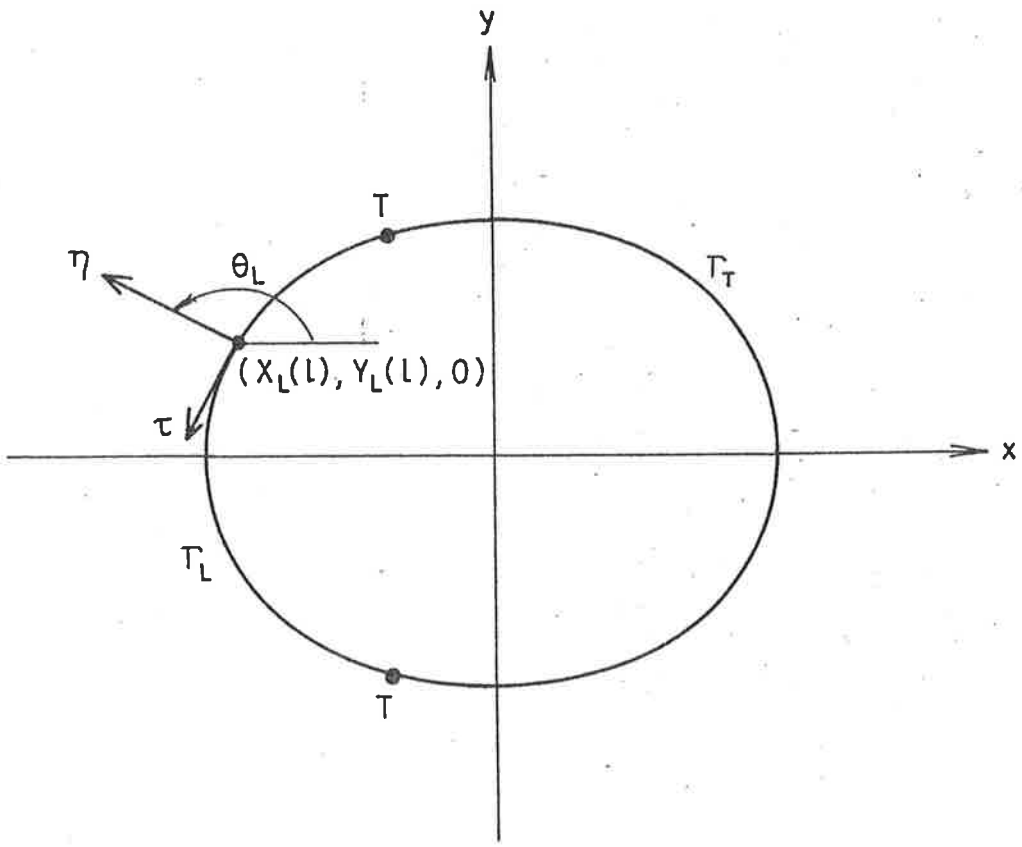

Figure 3.3 Planview of the stretched coordinate system used to define the leading edge region.

on the surface described by $\zeta = 0$.

The boundary condition on the leading edge of the body, $z = f^{\pm}(x,y)$, can be determined by means of a Taylor series expansion about h_0. That is, as $(x,y,z) \to (X_L(l), Y_L(l), 0)$,

$$\begin{aligned} z = f(x,y) \to h_0 + (x - X_L(l))\frac{\partial}{\partial x} f(X_L(l), Y_L(l)) \\ + (y - Y_L(l))\frac{\partial}{\partial y} f(X_L(l), Y_L(l)), \end{aligned} \tag{3.29}$$

or, in terms of the stretched coordinates,

$$\begin{aligned} \zeta = 1 + \left(\eta \cos\theta_l - \frac{\tau}{\epsilon}\sin\theta_l\right)\frac{\partial}{\partial x} f(X_L(l), Y_L(l)) \\ + \left(\eta \sin\theta_l + \frac{\tau}{\epsilon}\cos\theta_l\right)\frac{\partial}{\partial y} f(X_L(l), Y_L(l)). \end{aligned} \tag{3.30}$$

Hence, the limiting thin body is the semi-infinite flat plate $\zeta = 1 + O(\epsilon)$ and the limiting boundary conditions for that plate are found from equation (3.4) to be

$$\frac{\partial \phi_0^L}{\partial \zeta} = 0, \tag{3.31a}$$

and

$$\frac{\partial \phi_1^L}{\partial \zeta} = \cos\theta_l \frac{\partial f}{\partial x}\frac{\partial \phi_0^L}{\partial \eta} + \sin\theta_l \frac{\partial f}{\partial y}\frac{\partial \phi_0^L}{\partial \eta}. \tag{3.31b}$$

The leading edge solution must now be matched to the exterior solution (3.11). ϕ_1^E represents a distribution of sources of varying $O(\epsilon)$ strength $m(l)$ over Γ and is thus

$$\phi_1^E = \oint_\Gamma m(l) G(x,y,z : X_L(l), Y_L(l), 0) dl. \tag{3.32}$$

The Green's function $G(x,y,z; X_L(l), Y_L(l), 0)$, since it is a unit source potential, must have the property that as $(x,y,z) \to (X_L(l), Y_L(l), 0)$,

$$G \to -\frac{1}{4\pi}\left[(x - X_L(l))^2 + (y - Y_L(l))^2 + z^2\right]^{-\frac{1}{2}} + G_1, \tag{3.33}$$

where G_1 is bounded. Substitution of equation (3.33) into equation (3.11) gives

$$\phi^E = Ux + \oint_\Gamma m(l) \left[-\frac{1}{4\pi} \left[(x - X_L(l))^2 + (y - Y_L(l))^2 + z^2 \right]^{-\frac{1}{2}} + G_1 \right] dl. \quad (3.34)$$

In order to match with the leading edge flow, we need the edge behaviour of ϕ^E; that is, its limit as (x, y, z) moves close to Γ. This limit was obtained by Tuck (1975). The flow is considered to be in a plane normal to Γ at a fixed value of the arc–length coordinate l. If r is a plane polar coordinate centred on Γ in that plane, the limiting flow is

$$\phi^E \to UX_L(l) + \frac{m(l)}{2\pi} \log r + g(l) + O(r^2 \log r), \quad (3.35)$$

where

$$g(l) = -\frac{1}{4\pi} \int_\Gamma \log 2 \mid \mathbf{R}(l) - \mathbf{R}(l^*) \mid \frac{d}{dl^*} \left[\frac{m(l^*) \mid \mathbf{R}(l) - \mathbf{R}(l^*) \mid}{\mathbf{R}'(l^*) \cdot (\mathbf{R}(l) - \mathbf{R}(l^*))} \right] dl^* \quad (3.36)$$

$$+ \int_\Gamma m(l^*) G_1(X_L(l), Y_L(l), 0; X_L(l^*), Y_L(l^*), 0) dl^*,$$

$$r^2 = \eta^2 + \zeta^2, \quad (3.37)$$

and

$$\mathbf{R}(l) = X_L(l)\mathbf{i} + Y_L(l)\mathbf{j}. \quad (3.38)$$

The flow near such an edge will be two dimensional in the plane normal to Γ as rates of change parallel to Γ must be small compared to rates of change normal to Γ. Therefore, the leading edge flow is a two dimensional flow around a

semi–infinite flat plate. If $Z = \eta + \mathrm{i}\zeta$ (where $\mathrm{i} = \sqrt{-1}$), then this two–dimensional flow can be solved using the following conformal mapping (Kober (1952))

$$-\pi h_0 Z = w + \log w + 1, \tag{3.39}$$

which maps the flow region into the lower–half w plane. (See figure 3.4)

The relationship between the polar coordinate r and the complex variable Z is such that

$$\log r = \Re e\{\log Z\}, \tag{3.40}$$

and equation (3.35) becomes

$$\phi^E \to UX_L(l) + \frac{m(l)}{2\pi}\Re e\{\log Z\} + g(l). \tag{3.41}$$

In the w plane, the solution is a sink at $w = 0$ and therefore, on matching the leading edge potential to the exterior potential,

$$\phi^L = \frac{m(l)}{2\pi}\log w + C, \tag{3.42}$$

which matches equation (3.35) as $w \to \infty$ if

$$C = -\frac{m(l)}{2\pi}\log(\pi h_0) + UX_L(l) + g(l). \tag{3.43}$$

Thus the edge limit (equation (3.35)) of the outer solution becomes the outer boundary condition for the edge solution at $r = \infty$.

The leading edge potential must now be matched to the gap solution (that is, as $w \to 0$) and in this limit, we find that

$$\phi^L \to -\frac{h_0 m(l)}{2}\eta - \frac{m(l)}{2\pi}\log(\pi e h_0) + UX_L(l) + g(l). \tag{3.44}$$

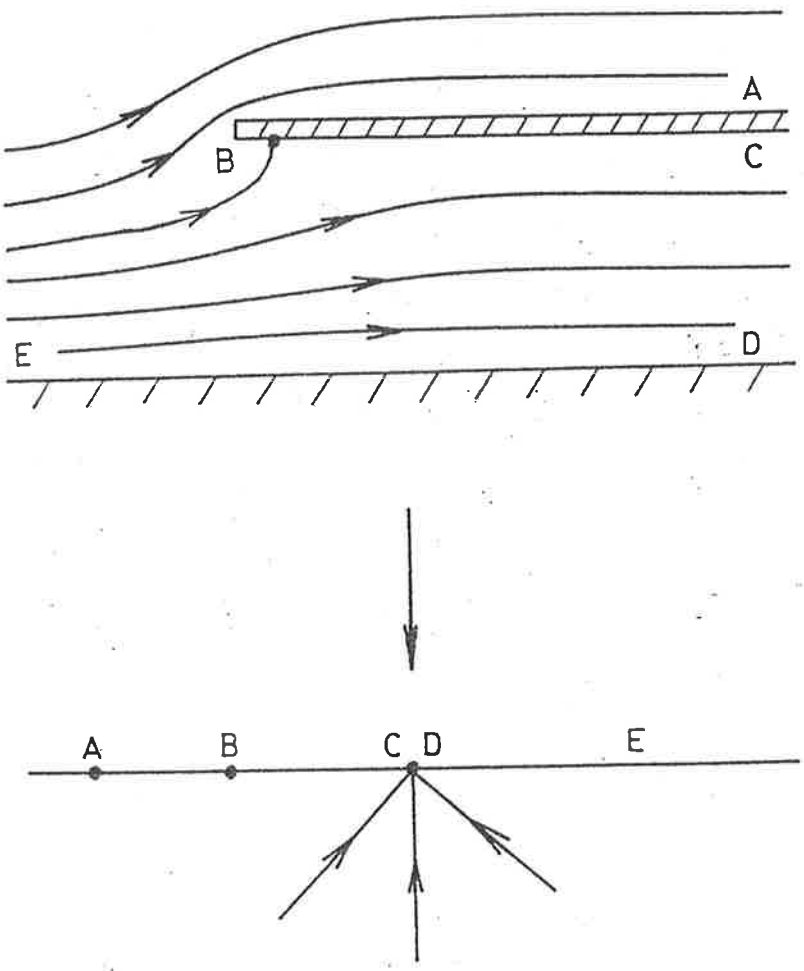

Figure 3.4 Flow in the leading edge region and its conformal mapping into the lower–half w plane.

Hence, the boundary conditions for the leading edge are

$$\phi^L \to UX_L(l) + g(l) - \frac{m(l)}{2\pi}\log(\pi e h_0), \tag{3.45a}$$

and

$$\frac{\partial \phi^L}{\partial n} = -\frac{h_0 m(l)}{2}, \tag{3.45b}$$

since η is a coordinate normal to Γ in the (x, y) plane. We note here that there is an alternative flow plan to the one shown in figure 3.4 and this arises when the normal component of velocity near the leading edge is positive; that is,

$$h_0\left(U\cos\theta_l - \frac{m(l)}{2}\right) > 0. \tag{3.45c}$$

This situation, illustrated in figure 3.5, has the notable feature that the stagnation point is located not on the body, but on the ground. However, although this is mathematically feasible, it is physically unlikely to occur and so, with the exception of the inverse solutions in chapter 6, we will not consider this situation as a viable alternative.

We conclude from equation (3.45a) that, to leading order, the boundary condition on the leading edge is given by equation (3.7). Physically, this condition ensures continuity of the velocity component tangent to the leading edge with that of the exterior flow.

3.6 The Trailing Edge Region

In this region, we define a similar stretched coordinate system (τ, η, ζ) as follows:

$$x = X_T(l) - \frac{h_0}{\epsilon}\tau\sin\theta_l + h_0\eta\cos\theta_l, \tag{3.46a}$$

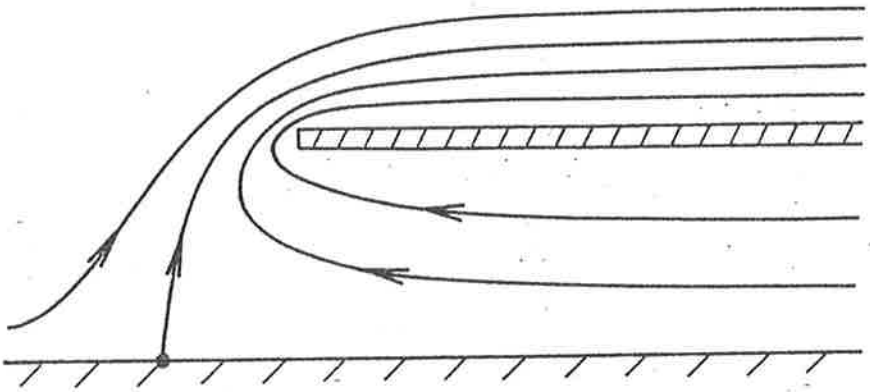

Figure 3.5 Flow in the leading edge region when $\frac{\partial \phi}{\partial n}^L > 0$. Note that the stagnation point lies on the ground and not on the body.

$$y = Y_T(l) + \frac{h_0}{\epsilon}\tau\cos\theta_l + h_0\eta\sin\theta_l, \tag{3.46b}$$

$$z = h_0\zeta. \tag{3.46c}$$

Laplace's equation transforms as in the leading edge to the following equations:

$$\frac{\partial^2\phi_0^T}{\partial\eta^2} + \frac{\partial^2\phi_0^T}{\partial\zeta^2} = 0, \tag{3.47a}$$

$$\frac{\partial^2\phi_1^T}{\partial\eta^2} + \frac{\partial^2\phi_1^T}{\partial\zeta^2} = 0, \tag{3.47b}$$

and

$$\epsilon^2\frac{\partial^2\phi_0^T}{\partial\tau^2} + \frac{\partial^2\phi_2^T}{\partial\eta^2} + \frac{\partial^2\phi_2^T}{\partial\zeta^2} = 0. \tag{3.47c}$$

The boundary equation (3.3) on $z = 0$ yields

$$\frac{\partial\phi_m^T}{\partial\zeta} = 0, \qquad m = 0, 1, 2, \ldots \tag{3.48}$$

on the surface $\zeta = 0$.

The boundary conditions on the body are found as in the leading edge case to be

$$\frac{\partial\phi_0^T}{\partial\zeta} = 0 \tag{3.49a}$$

and

$$\frac{\partial\phi_1^T}{\partial\zeta} = \cos\theta_l\frac{\partial f}{\partial x}\frac{\partial\phi_0^T}{\partial\eta} + \sin\theta_l\frac{\partial f}{\partial y}\frac{\partial\phi_0^T}{\partial\eta}. \tag{3.49b}$$

The trailing edge solutions must now be matched to both the gap solutions and the wake solutions. However, since these solutions are as yet unknown, this

matching must be done using Taylor series expansions and then applying the Kutta condition.

Therefore, to match the trailing edge potential to the gap potential, we expand as follows:

$$\begin{aligned}\phi^T \rightarrow & \phi_0^G(X_T(l), Y_T(l)) + \phi_1^G(X_T(l), Y_T(l)) \\ & + (x - X_L(l)) \frac{\partial}{\partial x}\phi_0^G(X_T(l), Y_T(l)) \\ & + (y - Y_L(l)) \frac{\partial}{\partial y}\phi_0^G(X_T(l), Y_T(l)) + O(\epsilon^2).\end{aligned} \tag{3.50}$$

After equating like powers of ϵ and substituting from equations (3.46), we find that

$$\phi_0^T \rightarrow \phi_0^G(X_T(l), Y_T(l)), \tag{3.51a}$$

and

$$\begin{aligned}\phi_1^T \rightarrow & \phi_1^G(X_T(l), Y_T(l)) \\ & + \left(-\frac{h_0}{\epsilon}\tau \sin\theta_l + h_0\eta\cos\theta_l\right) \frac{\partial}{\partial x}\phi_0^G(X_T(l), Y_T(l)) \\ & + \left(\frac{h_0}{\epsilon}\tau \cos\theta_l + h_0\eta\sin\theta_l\right) \frac{\partial}{\partial y}\phi_0^G(X_T(l), Y_T(l));\end{aligned} \tag{3.51b}$$

that is, in the limit as $\eta \rightarrow -\infty$ and $\zeta = O(1)$.

Matching of the velocity requires that

$$\begin{aligned}\nabla\phi_0^T(\tau, \eta) \rightarrow & \left(\frac{\partial\phi_0^G}{\partial x}\frac{\partial x}{\partial \eta} + \frac{\partial\phi_0^G}{\partial y}\frac{\partial y}{\partial \eta}\right)\mathbf{e}_\eta \\ & + \left(\frac{\partial\phi_0^G}{\partial x}\frac{\partial x}{\partial \tau} + \frac{\partial\phi_0^G}{\partial y}\frac{\partial y}{\partial \tau}\right)\mathbf{e}_\tau,\end{aligned} \tag{3.52a}$$

and

$$\begin{aligned}\nabla\phi_1^T(\tau,\eta) \to & \mathbf{e}_\tau\left[-\frac{h_0}{\epsilon}\sin\theta_l\frac{\partial\phi_0^G}{\partial x}+\frac{h_0}{\epsilon}\cos\theta_l\frac{\partial\phi_0^G}{\partial y}\right.\\ &\left.+\left(-\frac{h_0}{\epsilon}\tau\sin\theta_l+h_0\eta\cos\theta_l\right)\left(\frac{\partial\phi_0^G}{\partial x}\frac{\partial x}{\partial\tau}+\frac{\partial\phi_0^G}{\partial y}\frac{\partial y}{\partial\tau}\right)\right]\\ &+\mathbf{e}_\eta\left[h_0\sin\theta_l\frac{\partial\phi_0^G}{\partial x}+h_0\cos\theta_l\frac{\partial\phi_0^G}{\partial y}\right.\\ &\left.+\left(\frac{h_0}{\epsilon}\tau\cos\theta_l+h_0\eta\sin\theta_l\right)\left(\frac{\partial\phi_0^G}{\partial x}\frac{\partial x}{\partial\eta}+\frac{\partial\phi_0^G}{\partial y}\frac{\partial y}{\partial\eta}\right)\right],\end{aligned} \tag{3.52b}$$

in which $\mathbf{e}_\eta$ and $\mathbf{e}_\tau$ are unit vectors in the (τ,η,ζ) coordinate system.

Similar results follow for the matching of the velocity potential in the trailing edge to potential in the wake region:

$$\phi_0^T \to \phi_0^W(X_T(l),Y_T(l)), \tag{3.53a}$$

and

$$\begin{aligned}\phi_1^T \to & \phi_1^W(X_T(l),Y_T(l))\\ &+\left(-\frac{h_0}{\epsilon}\tau\sin\theta_l+h_0\eta\cos\theta_l\right)\frac{\partial}{\partial x}\phi_0^W(X_T(l),Y_T(l))\\ &+\left(\frac{h_0}{\epsilon}\tau\cos\theta_l+h_0\eta\sin\theta_l\right)\frac{\partial}{\partial y}\phi_0^W(X_T(l),Y_T(l));\end{aligned} \tag{3.53b}$$

that is, in the limit as $\eta\to\infty$ and $\zeta=O(1)$.

Matching the velocity with the wake flow results in

$$\begin{aligned}\nabla\phi_0^T(\tau,\eta) \to & \left(\frac{\partial\phi_0^W}{\partial x}\frac{\partial x}{\partial\eta}+\frac{\partial\phi_0^W}{\partial y}\frac{\partial y}{\partial\eta}\right)\mathbf{e}_\eta\\ &+\left(\frac{\partial\phi_0^W}{\partial x}\frac{\partial x}{\partial\tau}+\frac{\partial\phi_0^W}{\partial y}\frac{\partial y}{\partial\tau}\right)\mathbf{e}_\tau,\end{aligned} \tag{3.54a}$$

and

$$\begin{aligned}\nabla\phi_1^T(\tau,\eta) \rightarrow & \mathbf{e}_\tau\left[-\frac{h_0}{\epsilon}\sin\theta_l\frac{\partial\phi_0^W}{\partial x}+\frac{h_0}{\epsilon}\cos\theta_l\frac{\partial\phi_0^W}{\partial y}\right.\\ & \left.+\left(-\frac{h_0}{\epsilon}\tau\sin\theta_l+h_0\eta\cos\theta_l\right)\left(\frac{\partial\phi_0^W}{\partial x}\frac{\partial x}{\partial\tau}+\frac{\partial\phi_0^W}{\partial y}\frac{\partial y}{\partial\tau}\right)\right]\\ & +\mathbf{e}_\eta\left[h_0\sin\theta_l\frac{\partial\phi_0^G}{\partial x}+h_0\cos\theta_l\frac{\partial\phi_0^W}{\partial y}\right.\\ & \left.+\left(\frac{h_0}{\epsilon}\tau\cos\theta_l+h_0\eta\sin\theta_l\right)\left(\frac{\partial\phi_0^W}{\partial x}\frac{\partial x}{\partial\eta}+\frac{\partial\phi_0^W}{\partial y}\frac{\partial y}{\partial\eta}\right)\right].\end{aligned} \tag{3.54b}$$

Instead of matching with the exterior region, we must satisfy the pressure jump condition

$$\left[\frac{\partial\phi}{\partial x}\right]^2+\left[\frac{\partial\phi}{\partial y}\right]^2+\left[\frac{\partial\phi}{\partial z}\right]^2=U^2+O(\epsilon). \tag{3.55}$$

Transforming into the (τ,η,ζ) coordinate system, this means that

$$\frac{1}{h_0^2}\left(\left[\frac{\partial\phi^T}{\partial\eta}\right]^2+\epsilon^2\left[\frac{\partial\phi^T}{\partial\tau}\right]^2+\left[\frac{\partial\phi^T}{\partial\zeta}\right]^2\right)=U^2. \tag{3.56}$$

Substitution of the asymptotic expansion for ϕ^T into equation (3.56) yields

$$\frac{1}{h_0^2}\left(\left[\frac{\partial\phi_0^T}{\partial\eta}\right]^2+\epsilon^2\left[\frac{\partial\phi_0^T}{\partial\tau}\right]^2+\left[\frac{\partial\phi_0^T}{\partial\zeta}\right]^2\right)=U^2, \tag{3.57a}$$

and

$$\frac{2}{h_0^2}\left(\frac{\partial\phi_0^T}{\partial\eta}\frac{\partial\phi_1^T}{\partial\eta}+\epsilon^2\frac{\partial\phi_0^T}{\partial\tau}\frac{\partial\phi_1^T}{\partial\tau}+\frac{\partial\phi_0^T}{\partial\zeta}\frac{\partial\phi_1^T}{\partial\zeta}\right)=O(\epsilon). \tag{3.57b}$$

All of the boundary equations described above can be satisfied as $(x,y,z)\rightarrow(X_T(l),Y_T(l),0)$ by the solutions

$$\phi_0^T(\tau,\eta)=\phi_0^G(X_T(l),Y_T(l))=\phi_0^W(X_T(l),Y_T(l)), \tag{3.58a}$$

and

$$\begin{aligned}\phi_1^T(\tau,\eta) =& \phi_1^T + \left(-\frac{h_0}{\epsilon}\tau\sin\theta_l + h_0\eta\cos\theta_l\right)u_T \\ &+ \left(\frac{h_0}{\epsilon}\tau\cos\theta_l + h_0\eta\sin\theta_l\right)v_T,\end{aligned} \tag{3.58b}$$

providing

$$\phi_1^T = \phi_1^G(X_T(l), Y_T(l)) = \phi_1^W(X_T(l), Y_T(l)), \tag{3.59a}$$

$$u_T = \frac{\partial}{\partial x}\phi_0^G(X_T(l), Y_T(l)) = \frac{\partial}{\partial x}\phi_0^W(X_T(l), Y_T(l)), \tag{3.59b}$$

and

$$v_T = \frac{\partial}{\partial y}\phi_0^G(X_T(l), Y_T(l)) = \frac{\partial}{\partial y}\phi_0^W(X_T(l), Y_T(l)). \tag{3.59c}$$

The left hand side of the pressure equation (3.57a) can now be written as

$$\begin{aligned}\frac{1}{h_0^2}\left(\left[\frac{\partial\phi_0^T}{\partial\eta}\right]^2 + \epsilon^2\left[\frac{\partial\phi_0^T}{\partial\tau}\right]^2 + \left[\frac{\partial\phi_0^T}{\partial\zeta}\right]^2\right) &= \frac{1}{h_0^2}(u_T^2h_0^2 + v_T^2h_0^2) \\ &= u_T^2 + v_T^2 \\ &= U^2.\end{aligned} \tag{3.60}$$

Hence, the boundary condition, to leading order, on the trailing edge is given by equation (3.8).

CHAPTER 4

AN INTEGRAL EQUATION METHOD FOR EXPONENTIAL CLEARANCE

In this chapter, the full problem described by equations (3.6), (3.7) and (3.8) is solved using a boundary integral method in the special case when the clearance between the body and the ground is independent of y and exponential in x; that is,

$$f(x,y) = f_0 e^{-2kx}, \tag{4.1}$$

where f_0 is the clearance at x=0, and k is a parameter that controls the effective angle of attack of the body.

4.1 The Governing Equations

If the form for $f(x,y)$ described in equation (4.1) is substituted into equation (3.6), the resulting equation is

$$\frac{\partial^2 \phi}{\partial x^2} - 2k\frac{\partial \phi}{\partial x} + \frac{\partial^2 \phi}{\partial y^2} = 0. \tag{4.2}$$

Substitution of

$$\Phi(x,y) = e^{-kx}\phi(x,y) \tag{4.3}$$

into equation (4.2) results in the Helmholtz–type equation:

$$\frac{\partial^2 \Phi}{\partial x^2} + \frac{\partial^2 \Phi}{\partial y^2} = k^2 \Phi, \tag{4.4}$$

which has to be solved together with the appropriate boundary conditions derived from equations (3.7) and (3.8). This "potential" Φ can therefore be given a Green's integral representation (Bigg (1983)).

By considering a version of Green's theorem

$$\iint \left(A\nabla^2 B - B\nabla^2 A\right) dxdy = \oint_\Gamma \left(A\frac{\partial B}{\partial n} - B\frac{\partial A}{\partial n}\right) dl, \tag{4.5}$$

together with the properties of the Green's function and equation (4.4), we find that Φ at any interior point (x, y) of Γ may be written as

$$\Phi(x,y) = \int_\Gamma \left[\Phi(x',y')\frac{\partial}{\partial n}G(x',y';x,y) - G(x',y';x,y)\frac{\partial}{\partial n}\Phi(x',y')\right] dl, \tag{4.6}$$

where $G(x', y'; x, y)$ is the appropriate Green's function and $\frac{\partial}{\partial n}$ is an outward normal derivative with respect to (x', y').

However, equation (4.6) does not hold on Γ itself, and so must be modified using a limiting method described by Lee (1969) to enable the "velocity potential" Φ to be determined on the boundary. Thus, at (x, y) on the boundary Γ,

$$\Phi(x,y) = 2\oint_\Gamma \left[\Phi(x',y')\frac{\partial}{\partial n}G(x',y';x,y) - G(x',y';x,y)\frac{\partial}{\partial n}\Phi(x',y')\right] dl, \tag{4.7}$$

the integral taking its Cauchy principal value.

For the problem described by equation (4.4), the Green's function is a multiple of the zeroth order modified Bessel function of the second kind; that is,

$$G(x',y';x,y) = -\frac{1}{2\pi}K_0(kr'), \tag{4.8}$$

where r' is the distance between the interior point (x', y') and the boundary point (x, y) or

$$r' = \left[(x - x')^2 + (y - y')^2\right]^{\frac{1}{2}}. \tag{4.9}$$

The method used to determine the Green's function for such a partial differential equation is detailed by Chester (1971).

4.2 Discretization

We must now discretize equation (4.7) to solve for Φ along the boundary. This is accomplished firstly by dividing the boundary Γ into N subintervals. Then along each of these segments, Φ and $\frac{\partial \Phi}{\partial n}$ are considered to be constant and their values at the midpoint of a given segment are used. Thus, the integral equation (4.7) is approximated by

$$\begin{aligned}\Phi(x_i, y_i) = &\sum_{j=1}^{N} \Phi(x_j, y_j) \int_{\Delta l_j} -\frac{1}{\pi} \frac{\partial}{\partial n} K_0(kr')dl \\ &- \sum_{j=1}^{N} \frac{\partial}{\partial n} \Phi(x_j, y_j) \int_{\Delta l_j} -\frac{1}{\pi} K_0(kr')dl, \quad i = 1, 2, \ldots, N,\end{aligned} \tag{4.10}$$

where (x_i, y_i) is the midpoint of the i^{th} segment, and Δl_j denotes the j^{th} segment.

This can be rewritten in matrix form as

$$\Phi = A\Phi - B\Phi_n, \tag{4.11}$$

in which

$$[A]_{i,j} = -\frac{1}{\pi} \int_{\Delta l_j} \frac{\partial}{\partial n} K_0(kr')dl, \qquad i, j = 1, 2, \ldots, N, \tag{4.12a}$$

$$[B]_{i,j} = -\frac{1}{\pi} \int_{\Delta l_j} K_0(kr')dl, \qquad i,j = 1,2,\ldots,N, \tag{4.12b}$$

$$[\Phi]_i = \Phi(x_i, y_i), \qquad i = 1,2,\ldots,N, \tag{4.12c}$$

and

$$[\Phi_n]_i = \frac{\partial}{\partial n}\Phi(x_i, y_i). \qquad i = 1,2,\ldots,N. \tag{4.12d}$$

Assuming the coefficients of A and B are known, equation (4.11) provides the framework for evaluating Φ and hence our velocity potential ϕ. We can rewrite equation (4.11) as

$$\Phi_n = B^{-1}(A - I)\Phi, \tag{4.13}$$

where I is the N x N identity matrix, and this equation together with equation (4.3) gives the relationship between the velocity potential ϕ and its normal derivative $\frac{\partial \phi}{\partial n}$:

$$\phi_n = D[B^{-1}(A - I) + E]D^{-1}\phi, \tag{4.14}$$

in which

$$[\phi]_i = \phi(x_i, y_i), \qquad i = 1,2,\ldots,N, \tag{4.15a}$$

$$[\phi_n]_i = \frac{\partial}{\partial n}\phi(x_i, y_i), \qquad i = 1,2,\ldots,N, \tag{4.15b}$$

$$D = \mathrm{diag}(e^{kx_1}, e^{kx_2}, \ldots, e^{kx_N}), \tag{4.15c}$$

and

$$E = \mathrm{diag}\left(\frac{\partial x_1}{\partial n}, \frac{\partial x_2}{\partial n}, \ldots, \frac{\partial x_N}{\partial n}\right). \tag{4.15d}$$

4.3 Evaluation of Matrix Coefficients

The coefficients of the matrices A and B can be evaluated by a combination of numerical and analytic techniques (Bigg (1983)). The kernels of each integral can be split into their singular and nonsingular components; the singular parts then being integrated exactly, and the nonsingular parts being integrated numerically.

Firstly, we split the Green's function $K_0(kr')$ into its singular and nonsingular parts (Abramowitz and Stegun (1964)):

$$K_0(kr') = -\log r' + M(k, r'), \tag{4.16}$$

$M(k, r')$ being the nonsingular component. The general coefficient of A is then

$$[A]_{i,j} = -\frac{1}{\pi} \int_{\Delta l_j} \left[\frac{\partial}{\partial n} M(k, r') - \nabla \log r' \cdot \mathbf{n} \right] dl, \quad i, j = 1, 2, \ldots, N. \tag{4.17}$$

We shall represent the segment by the following parametric form:

$$\mathbf{R}(l) = X(l)\mathbf{i} + Y(l)\mathbf{j}, \tag{4.18}$$

in which

$$X(l) = \begin{cases} X_L(l) & \text{on the leading edge} \\ X_T(l) & \text{on the trailing edge,} \end{cases}$$

and

$$Y(l) = \begin{cases} Y_L(l) & \text{on the leading edge} \\ Y_T(l) & \text{on the trailing edge.} \end{cases}$$

From the definition of r' given by equation (4.9), the singular part of equation (4.17) may be written as

$$A_s = -\frac{1}{\pi} \int_{l_j}^{l_{j+1}} \frac{[x_i - X(l)]Y'(l) - [y_i - Y(l)]X'(l)}{(x_i - X(l))^2 + (y_i - Y(l))^2} dl, \tag{4.19}$$

since $\mathbf{n} = Y'(l)\mathbf{i} - X'(l)\mathbf{j}$. Making the change of variable

$$\vartheta = \frac{[y_i - Y(l)]}{[x_i - X(l]}, \tag{4.20}$$

where

$$d\vartheta = dl\left[\frac{X'(l)[y_i - Y(l)] - Y'(l)[x_i - X(l)]}{[x_i - X(l)]^2}\right], \tag{4.21}$$

equation (4.19) becomes

$$\begin{aligned} A_s &= \frac{1}{\pi}\fint_{l_j}^{l_{j+1}} \frac{1}{1+\vartheta^2} d\vartheta \\ &= \begin{cases} \frac{1}{\pi}\left[\arctan\left(\frac{y_i - Y_{j+1}}{x_i - X_{j+1}}\right) - \arctan\left(\frac{y_i - Y_j}{x_i - X_j}\right)\right] & i \neq j, \\ 0 & i = j, \end{cases} \end{aligned} \tag{4.22}$$

in which (X_j, Y_j) is the coordinate of the j^{th} grid–point.

The nonsingular part of equation (4.17) may be integrated by Simpson's three point rule using packaged (IMSL) Bessel functions modified to eliminate the singular terms.

In the same way as for matrix A, the general coefficient of B becomes

$$[B]_{i,j} = -\frac{1}{\pi}\fint_{\Delta l_j} [M(k, r') - \log r']\, dl, \qquad i, j = 1, 2, \ldots, N. \tag{4.23}$$

Once again, the nonsingular part may be integrated using Simpson's rule, but the singular part requires different treatment using complex variables. Thus,

$$B_s = \frac{1}{\pi}\int_{\Delta l_j} \fint 1 \log r'\, dl = \Re e\left\{\frac{1}{\pi}\int_{\xi_1}^{\xi_2} \log \xi\, d\xi e^{-\mathrm{i}\beta}\right\}, \tag{4.24}$$

where

$$e^{-\mathrm{i}\beta} = \frac{[(X_{j+1} - X_j) - \mathrm{i}(Y_{j+1} - Y_j)]}{\Delta l_j}, \tag{4.25}$$

$$\xi_1 = (X_j - x_i) + \mathrm{i}(Y_j - y_i) \tag{4.26a}$$

and

$$\xi_2 = (X_{j+1} - x_i) + \mathrm{i}(Y_{j+1} - y_i) \tag{4.26b}$$

as illustrated in figure 4.1. Simplifying equation (4.24) gives

$$B_s = \frac{1}{\pi}\Re e\Big\{ e^{-\mathrm{i}\beta}\left[\xi_2(\log \xi_2 - 1) - \xi_1(\log \xi_1 - 1)\right]\Big\}. \tag{4.27}$$

With the coefficients of matrices A and B now known, equations (4.14), (3.7) and (3.8) form the framework for our numerical scheme. At this stage, we note that it is more convenient to consider equation (3.8) in the following form:

$$\left[\frac{\partial \phi}{\partial n}\right]^2 + \left[\frac{\partial \phi}{\partial s}\right]^2 = U^2, \tag{4.28}$$

where $\frac{\partial \phi}{\partial s}$ is the tangential derivative of ϕ, and is represented by a weighted finite difference approximation in terms of ϕ.

We begin our numerical scheme by selecting a starting value for the velocity potential ϕ at the mid–point of each segment around the boundary Γ and calculate $\frac{\partial \phi}{\partial n}$ from equation (4.14). For potentially leading edge segments, an accurate initial estimate is given by equation (3.7). We must now determine which segments of Γ are leading edge segments and which are trailing edge segments in order to apply the boundary conditions (3.7) and (4.28) to the N segments. This may be done by keeping track of the mean normal velocity u_n, defined by

$$u_n = \frac{1}{2}\left(\frac{\partial \phi}{\partial n} + U\cos\theta\right), \tag{4.29}$$

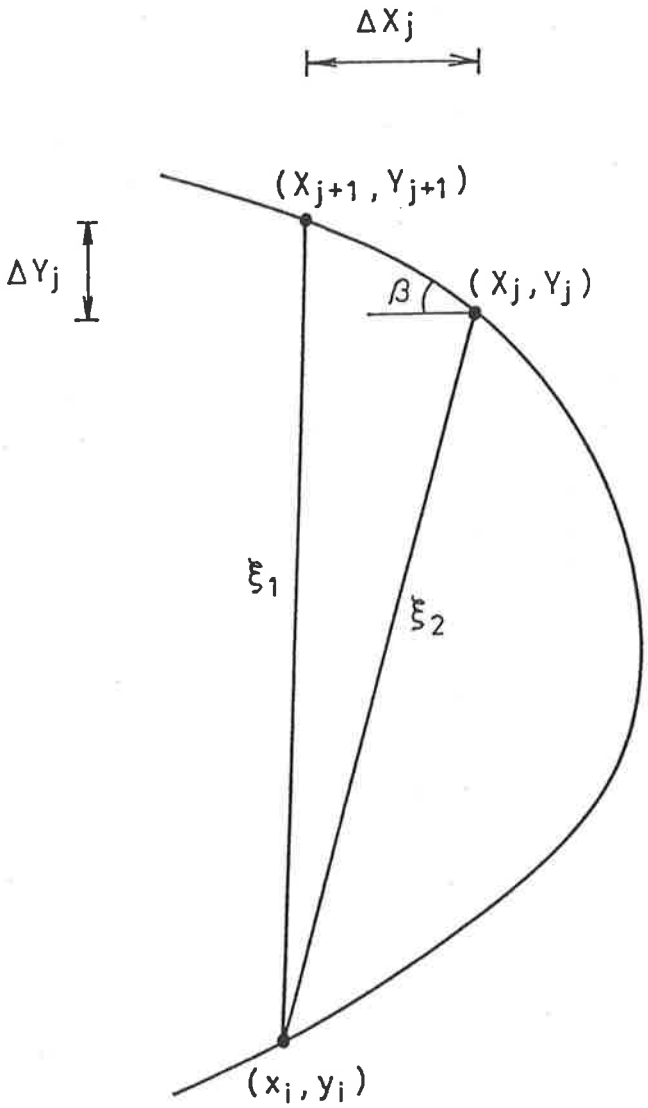

Figure 4.1 Illustration of the coordinates used to calculate the entries in the singular matrix B_s.

in which the first term on the right hand side of the equation represents the normal component of velocity under the body, and the second term is the normal component over the body. As previously discussed, the mean normal velocity u_n is negative in the leading edge regime and positive in the trailing edge regime. Hence, at each segment on the boundary Γ, we compute the mean normal velocity and note the value of i such that u_n changes sign between (x_i, y_i) and (x_{i+1}, y_{i+1}). The transition point T may then be determined by linear interpolation in this interval. Having found T, we can determine the appropriate boundary condition for each segment.

An iterative scheme is now used to solve the N nonlinear boundary equations for the velocity potential ϕ. At each step, the value of $\frac{\partial \phi}{\partial n}$ is found using equation (4.14) and the current ϕ values, keeping track of u_n as we go. We then substitute the new $\frac{\partial \phi}{\partial n}$ into the appropriate boundary equation and thus calculate the new value of the velocity potential ϕ.

Therefore, by rewriting the governing partial differential equation (3.6) in the Helmholtz–type form (4.4), we can use the above integral equation method to find the velocity potential ϕ, around the boundary Γ. If we consider only planforms symmetric about the x–axis, then, after some manipulation of the coefficients of the matrices A and B, we need only solve $N/2$ nonlinear boundary equations resulting in a significant reduction in the time taken to compute solutions and the storage space required.

4.4 Interior Points

It may also be necessary to compute the velocity potential ϕ at points under the body; that is, inside Γ. Equation (4.6) is similar to equation (4.7) and may be discretized in the same way to give the matrix equation:

$$\Theta = \frac{1}{2}\left(\bar{A}\phi - \bar{B}\phi_n\right), \tag{4.30}$$

in which Θ is the vector of the interior ϕ values at N selected points, and the barred matrices $\bar{A}$ and $\bar{B}$ have coefficients which contain integrals of regular, rather than Cauchy principle value, interpretation. Therefore, once the velocity potential is known on the boundary Γ, it can be found at any point inside Γ by matrix multiplication.

4.5 Confirmation of Numerical Analysis

In this chapter, the theory has been presented for a thin body of arbitrary planform and with clearance independent of y and exponential in x. Before applying this theory, it is necessary to ensure that the theory is correct and that the numerical scheme is accurate. There are no examples of exact solutions (to the full problem) with which to compare the approximate solution obtained using the method developed, and so we will consider testing the method in two stages.

Firstly, we can test the accuracy with which the method produces a solution to the governing partial differential equation (4.4) as there are known theoretical

solutions that satisfy this equation. In the special case when the planform is a circle, one such solution is

$$\Phi = I_1(kr)\cos\theta, \tag{4.31}$$

in which I_1 is the first order modified Bessel function of the first kind. Differentiating equation (4.31) with respect to r, we obtain the normal derivative of this "potential" Φ

$$\Phi_n = k\cos\theta\left(I_0(kr) - \frac{1}{kr}I_1(kr)\right), \tag{4.32}$$

where I_0 is the zeroth order modified Bessel function of the first kind.

Once the boundary of the circle has been divided into N segments, exact values of the "potential" Φ and its normal derivative Φ_n are calculated at the midpoints of all the segments. Approximate values of Φ_n are then computed from equation (4.13) and compared to the exact values. Any difference between these two sets of solutions is due to the discretization of the integral equation (4.7). Figure 4.2 shows a graph of the relative error between the exact and approximate solutions plotted against $(100/N)^2$ for $N = 40, 60, 80, 100, 120$. From the graph, it can be seen that the error produced by the method described is a linear function of N^{-2}. Therefore, the method used to discretize equation (4.7) is second order.

Secondly, we must examine how well the computed velocity potential ϕ satisfies the boundary conditions, and determine the convergence of the results as we increase N, the number of segments. As previously mentioned, there are no exact solutions to the full problem and so we will look at the behaviour of the

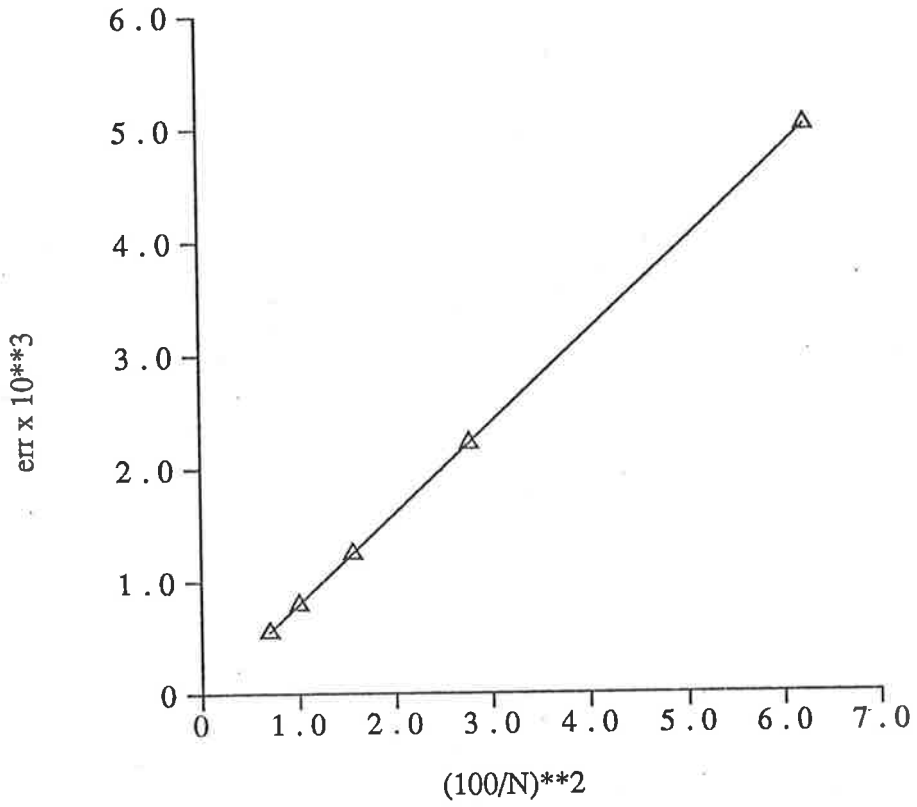

Figure 4.2 Graph of relative error between the approximate solution and the exact solution versus $(100/N)^2$. This illustrates the accuracy with which the program models the Helmholtz–like equation.

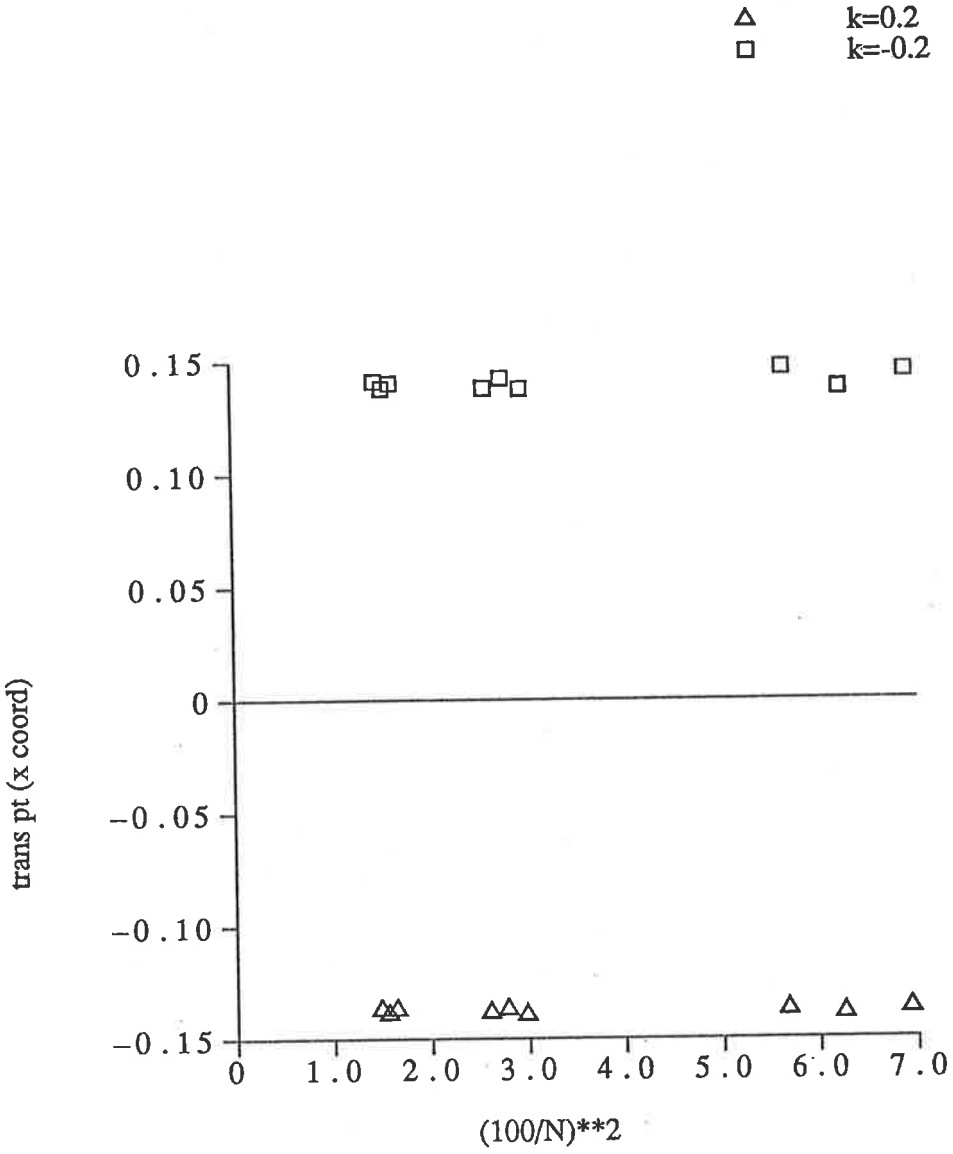

Figure 4.3 Graph of transition point versus $(100/N)^2$ for two values of k to determine the convergence of the boundary conditions.

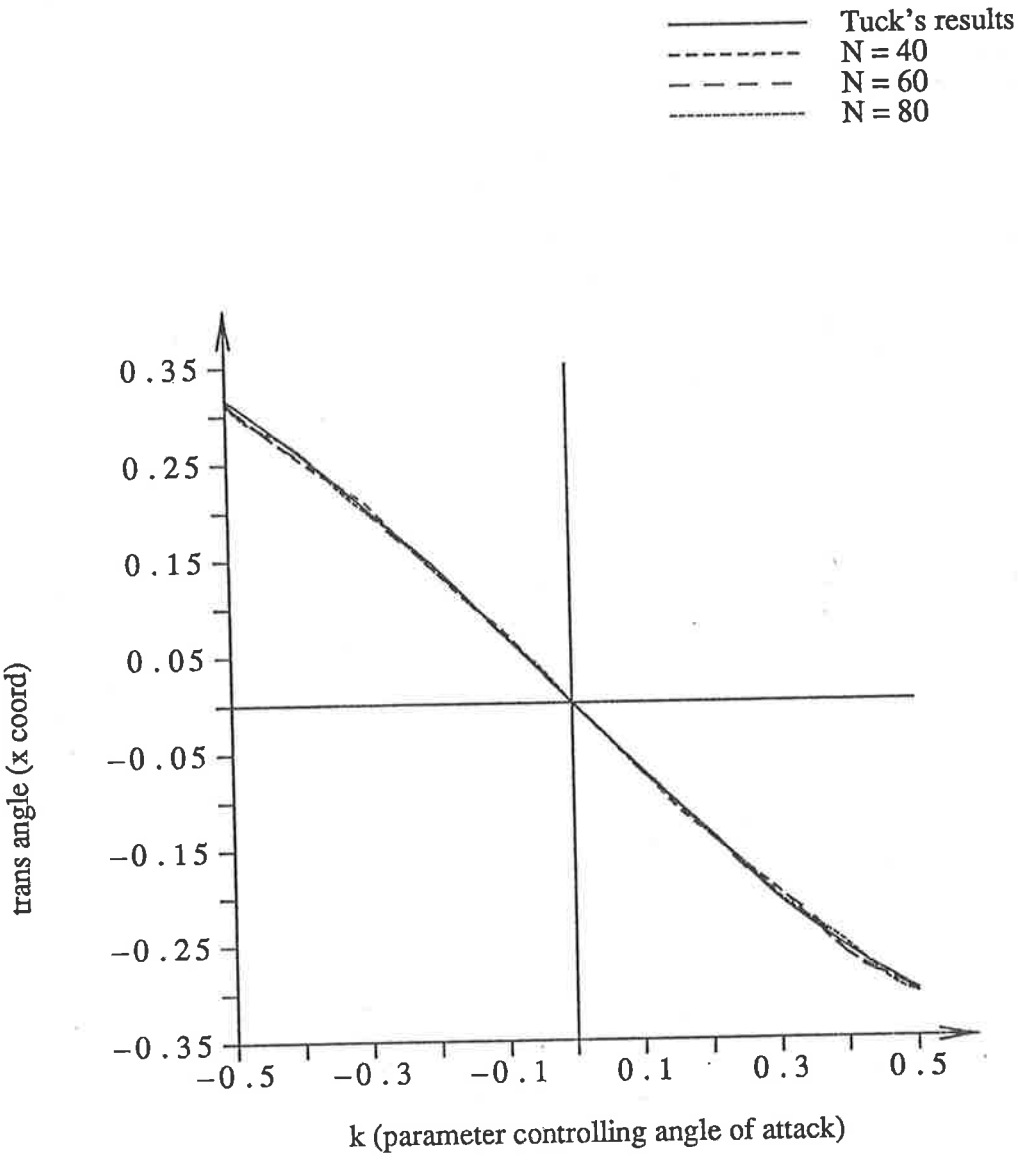

Figure 4.4 Comparison of numerical scheme to results produced by Tuck in the special case of a circular planform.

transition point between the leading edge and the trailing edge to give an indication of the convergence of the method. Figure 4.3 is a graph of the x–coordinate of the transition point (since the problem is symmetric in y) plotted against $(100/N)^2$ for various values of N. From this graph, it can be seen that there is little change in the transition point as we increase N. In fact, the relative difference between the computed values when $N = 40$ and when $N = 80$ is less than 1 % for values of k ranging from –0.5 through to 0.5.

One final check on the numerical method is to compare the results produced to those computed by Tuck (1983) using a series form in polar coordinates for the velocity potential ϕ:

$$\phi(r,\theta) = e^{kr\cos\theta} \sum_{j=0}^{\infty} \gamma_j \frac{I_j(|k|r)}{I_j(|k|)} \cos\theta, \tag{4.33}$$

where I_j is the j^{th} order modified Bessel function of the first kind. Figure 4.4 shows a direct comparison of the transition points produced by the method described here for various values of N with the results from the method devised by Tuck. The graph shows little significant difference between the results from the two methods and also emphasizes the convergence of the numerical scheme described here.

Thus, we have established that our numerical scheme can be used to solve the governing partial differential equation and boundary conditions with reasonable accuracy and can now apply the method with confidence to various problems in ground effect.

CHAPTER 5

TRANSITION FOR LOW ASPECT RATIO ELLIPSES AND NEAR–RECTANGLES

One point of interest with the extreme ground effect problem is the location of transition between the leading edge region and the trailing edge region. The linearized problem in which the gap flow is almost undisturbed by the body; that is,

$$f(x,y) = f_0 + f_1(x,y), \tag{5.1}$$

$$\phi(x,y) = Ux + \phi_1(x,y), \tag{5.2}$$

where $f_0 \ll f_1$ and $\phi_1 \ll Ux$, was first discussed by Widnall and Barrows (1970). They derived an explicit solution for a semi–elliptical planform with a uniformly sloping bottom; that is, for a straight trailing edge $x = 0$, a semi–elliptical leading edge in $x < 0$, and transition points fixed at the junctions of the two regions. Tuck (1983) also investigated the linearized problem and showed that for convex planforms, the transition points will occur at the widest points of the body; for example, wing tips. This result was formally proved by Pryde and van der Hoek (1984).

5.1 Low Aspect Ratio Theory

This result is no longer true when the problem is nonlinear. Newman (1982) solved the nonlinear, unsteady problem for planforms with low aspect ratio and

with clearance dependent on x and t, and, in particular, considered the steady motion of a planar delta wing with constant angle of attack. He found that for sufficiently large angles of attack, transition occurs forward of the wing tips and for smaller (and negative) angles of attack, transition is confined to the abrupt tail.

It is relatively straight–forward to derive a transition point condition for a thin body with low aspect ratio when the clearance is dependent on both x and y and there is no dependence on time. The flow under such a thin body is governed by the partial differential equation (3.6) in which $f = f(x, y)$. If we assume that the velocity potential ϕ is given by equation (5.2), then to leading order, our partial differential equation becomes

$$\frac{\partial f}{\partial x}U + \frac{\partial}{\partial y}\left(f\frac{\partial \phi_1}{\partial y}\right) = 0. \tag{5.3}$$

We can rearrange this equation to obtain

$$\frac{\partial}{\partial y}\left(f\frac{\partial \phi_1}{\partial y}\right) = -\frac{\partial f}{\partial x}U \tag{5.4}$$

and after integrating twice with respect to y, we have the solution

$$\phi_1(x, y) = -U\int \frac{1}{f(x, Y)}\int \frac{\partial}{\partial x}f(x, y^*)dy^*dY + C(x) + D(x)\int \frac{dY}{f(x, Y)}. \tag{5.5}$$

If we assume that the body is symmetric in y, then

$$D(x) \equiv 0. \tag{5.6}$$

Therefore, our velocity potential ϕ is given by

$$\phi = Ux - U\int \frac{1}{f(x, Y)}\int \frac{\partial}{\partial x}f(x, y^*)dy^*dY + C(x). \tag{5.7}$$

The associated boundary conditions for the partial differential equation (3.6) are the leading edge condition (3.7) and the trailing edge condition (3.8). Hence, on the leading edge

$$C(x) = U \int \frac{1}{f(x,Y)} \int \frac{\partial}{\partial x} f(x,y^*) dy^* dY. \tag{5.8}$$

The Kutta condition (3.8) requires that on the trailing edge

$$\left(U + \frac{\partial \phi_1}{\partial x}\right)^2 + \left(\frac{\partial \phi_1}{\partial y}\right)^2 = U^2, \tag{5.9}$$

or, to leading order,

$$2U \frac{\partial \phi_1}{\partial x} + \left(\frac{\partial \phi_1}{\partial y}\right)^2 = 0. \tag{5.10}$$

After substituting equation (5.5) into equation (5.10), we arrive at the following trailing edge condition:

$$\begin{aligned} 2U \Bigg(& -U \int \frac{1}{f(x,Y)} \int \frac{\partial^2}{\partial x^2} f(x,y^*) dy^* dY \\ & + U \int \frac{1}{f(x,Y)^2} \frac{\partial}{\partial x} f(x,Y) \int \frac{\partial}{\partial x} f(x,y^*) dy^* dY + \frac{d}{dx} C(x) \Bigg) \\ & + \left(-\frac{U}{f(x,y)} \int \frac{\partial}{\partial x} f(x,Y) dY \right)^2 = 0. \end{aligned} \tag{5.11}$$

We can now rearrange equation (5.11) to obtain the following expression for $\frac{d}{dx}C(x)$:

$$\begin{aligned} \frac{d}{dx} C(x) = & -\frac{1}{2U} \left(-\frac{U}{f(x,y)} \int \frac{\partial}{\partial x} f(x,Y) dY \right)^2 \\ & + U \int \frac{1}{f(x,Y)} \int \frac{\partial^2}{\partial x^2} f(x,y^*) dy^* dY \\ & - U \int \frac{1}{f(x,Y)^2} \frac{\partial}{\partial x} f(x,Y) \int \frac{\partial}{\partial x} f(x,y^*) dy^* dY. \end{aligned} \tag{5.12}$$

At the transition point between the leading edge and the trailing edge, both conditions (5.8) and (5.12) must be satisfied. By differentiating equation (5.8) with respect to x, and comparing this to equation (5.12), we can determine the condition for the point of transition; that is, from equation (5.8) we find that

$$\begin{aligned}\frac{d}{dx}C(x) = &-U\int\frac{1}{f(x,Y)^2}\frac{\partial}{\partial x}f(x,Y)\int\frac{\partial}{\partial x}f(x,y^*)dy^*dY\\ &+U\int\frac{1}{f(x,Y)}\int\frac{\partial^2}{\partial x^2}f(x,y^*)dy^*dY\\ &+\frac{U}{f(x,y)}\frac{d}{dx}y(x)\int\frac{\partial}{\partial x}f(x,Y)dY,\end{aligned}\tag{5.13}$$

and comparing this to equation (5.12), both conditions are satisfied if

$$\frac{U}{f(x,y)}\frac{d}{dx}y(x)\int\frac{\partial}{\partial x}f(x,Y)dY = -\frac{U}{2f(x,y)^2}\left(\int\frac{\partial}{\partial x}f(x,Y)dY\right)^2.\tag{5.14}$$

There are two solutions to this equation, namely

$$\int\frac{\partial}{\partial x}f(x,Y)dY = 0\tag{5.15}$$

and

$$\frac{d}{dx}y(x) = -\frac{1}{2}\frac{1}{f(x,y)}\int\frac{\partial}{\partial x}f(x,Y)dY.\tag{5.16}$$

This last solution simplifies to

$$\frac{d}{dx}y(x) = -\frac{1}{2}\frac{y(x)}{f(x)}\frac{d}{dx}f(x),\tag{5.17}$$

when $f = f(x)$ and this result agrees with Newman's low aspect ratio theory.

We shall now apply this low aspect ratio theory to our problem, which has clearance constant in y and exponential in x, and for thin bodies with "low" aspect ratio, we should be able to produce the predicted transition points. This

entails both solving for some "low" aspect ratio planform and determining the range of values of aspect ratios which can be considered as "low". We can do this by selecting a family of planforms and gradually decreasing the aspect ratio until the solutions converge (to the low aspect ratio solutions).

A suitable choice of planforms is the following family of ellipses:

$$x^2 + (y/b)^2 = 1. \tag{5.18}$$

As these bodies are symmetric in y, we will restrict our attention to the transition point in the positive y domain. The low aspect ratio theory predicts that if

$$0 < f(x) \ll y(x) \ll 1, \tag{5.19}$$

then transition occurs when equation (5.17) is satisfied. For our problem, y is determined from equation (5.18) and $f(x)$ is defined by equation (4.1). Solving equation (5.17) for the chosen family of planforms, we find the relationship between k (the parameter controlling the angle of attack) and the x–coordinate of the transition point is given by

$$k = -\frac{x}{1-x^2}. \tag{5.20}$$

By considering the ellipses produced using $b = 1.0$, 0.5, 0.4, 0.3 and 0.2 (illustrated in figure 5.1), we can determine, for a range of values of k, the x–coordinate of the transition point. Figure 5.2 shows the results for these ellipses and also the results predicted by the low aspect ratio theory. As the aspect ratio decreases, the results converge to those predicted by the low aspect ratio theory and if b is less than 0.4, then the body has a sufficiently low aspect ratio to be included in the low aspect ratio analysis.

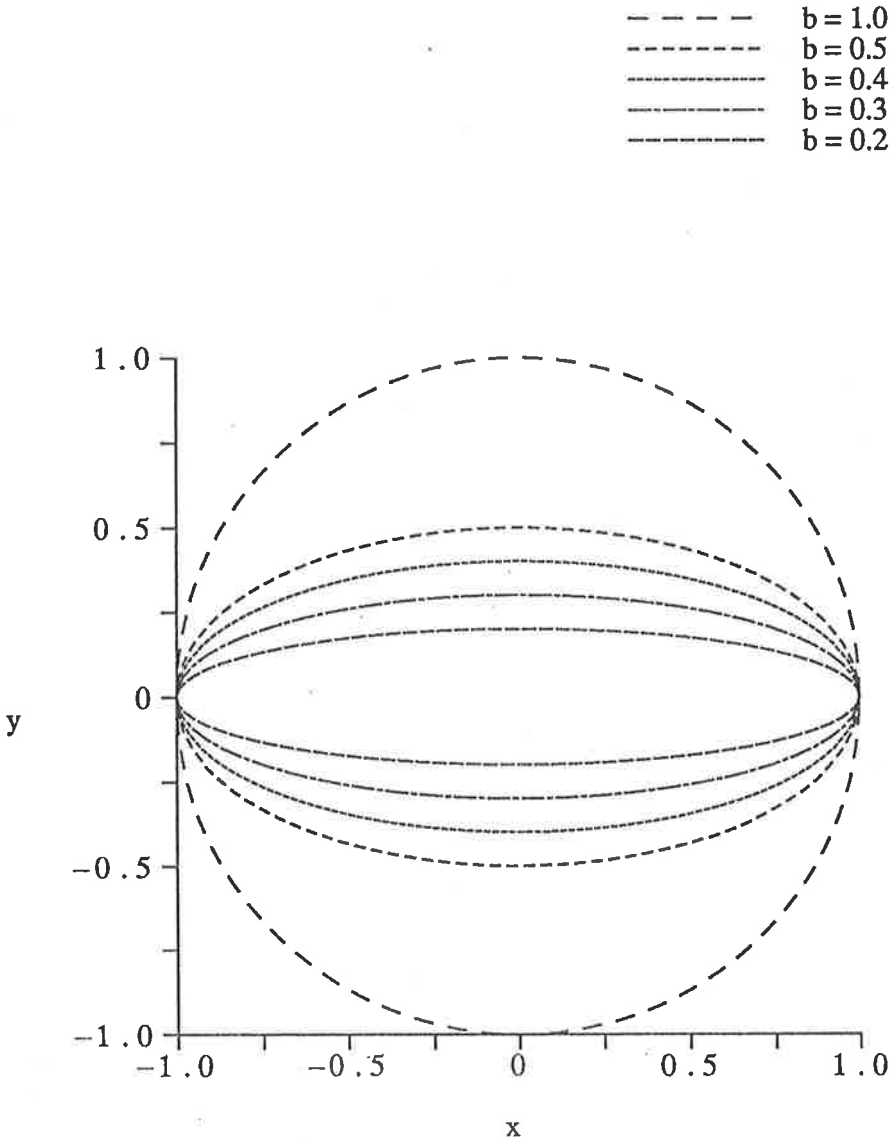

Figure 5.1 Family of ellipses with varying aspect ratios (or b values) to be used in comparison with low aspect ratio theory.

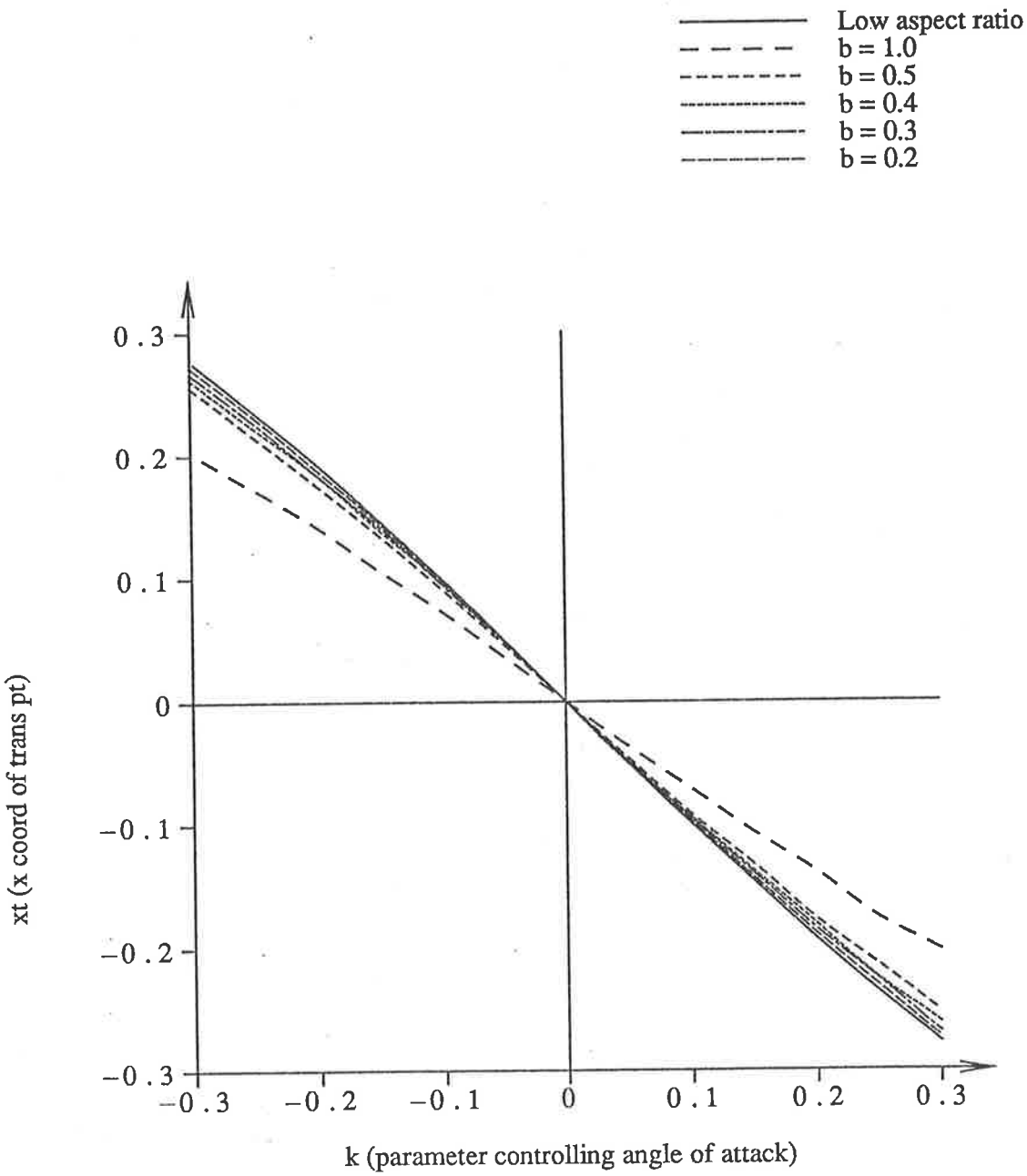

Figure 5.2 Graph of the x–coordinate of the transition point plotted against k, the parameter controlling the angle of attack, for the elliptic planforms illustrated in Figure 5.1. The solid line represents the values predicted by the low aspect ratio theory.

5.2 Transition for Near–rectangles

Tuck (1983) extended the nonlinear theory to include planforms with arbitrary aspect ratio and illustrated it by solving the problem of the circular planform with clearance constant in y and exponential in x briefly described in the previous chapter. For this example, the transition points were again located forward of the widest points for positive angle of attack, and conversely, for negative angle of attack, downstream from the widest points (see figure 4.4).

Thus, it appears that for the nonlinear ground effect on thin wings of arbitrary aspect ratio, the points of transition depend on both the angle of attack and the planform of the thin body.

From figure 4.4, it can be seen that for the circle, the relationship between the angle of attack and the transition point is almost linear. But how would this change as the shape becomes more rectangular? And what affect does the aspect ratio of the thin body have on the position of the transition point? By using the following family of planforms:

$$x^{2q} + (y/b)^{2q} = 1, \tag{5.21}$$

in which q and b are positive constants, we can determine how the locations of the transition points depend on these factors. Once again, as these bodies are symmetric in y, we will restrict our attention to the transition point in the positive y region. When $q = 1$ and $b = 1$, the planform described is a circle and as q increases, the planform becomes more rectangular. By varying b, we can change

the aspect ratio of the planform to see how it affects the transition between leading edge and trailing edge.

Figure 5.3 contains the first three planforms which were used. Each has an aspect ratio of one and was generated from equation (5.21) using $q = 1, 1.5$ and 3.0 respectively. The case $q = 1$ has already been solved and the computed values for the velocity potential ϕ can be used as initial guesses for the velocity potential for the subsequent values of q. Figure 5.4 shows three planforms with aspect ratio of 0.5. Once again, the example with $q = 1$ was solved first and the values of the velocity potential used as starting values for the other examples. In the same way, we would also like to test planforms with high aspect ratio and figure 5.5 contains three such planforms, each with an aspect ratio of two.

The calculations were repeated for each of these planforms and the $x-$coordinate of the transition point was recorded for values of k ranging from -0.5 to 0.5. Figures 5.6, 5.7 and 5.8 show, for each of the three sets of planforms, the graph of the $x-$coordinate of the transition point plotted against k. In each case, it can be seen that for the elliptic shape ($q = 1$), the relationship is almost linear and as q increases, or the planform becomes more rectangular, the graph becomes increasingly nonlinear for small values of k; that is, for small values of k, the location of the transition point rapidly varies. In fact, as the body shape becomes more rectangular, the profile of the graph becomes more like a step function, and we postulate that if the planform were rectangular, the graph would indeed assume a profile like that of a step function. This would mean that for a rectangular thin

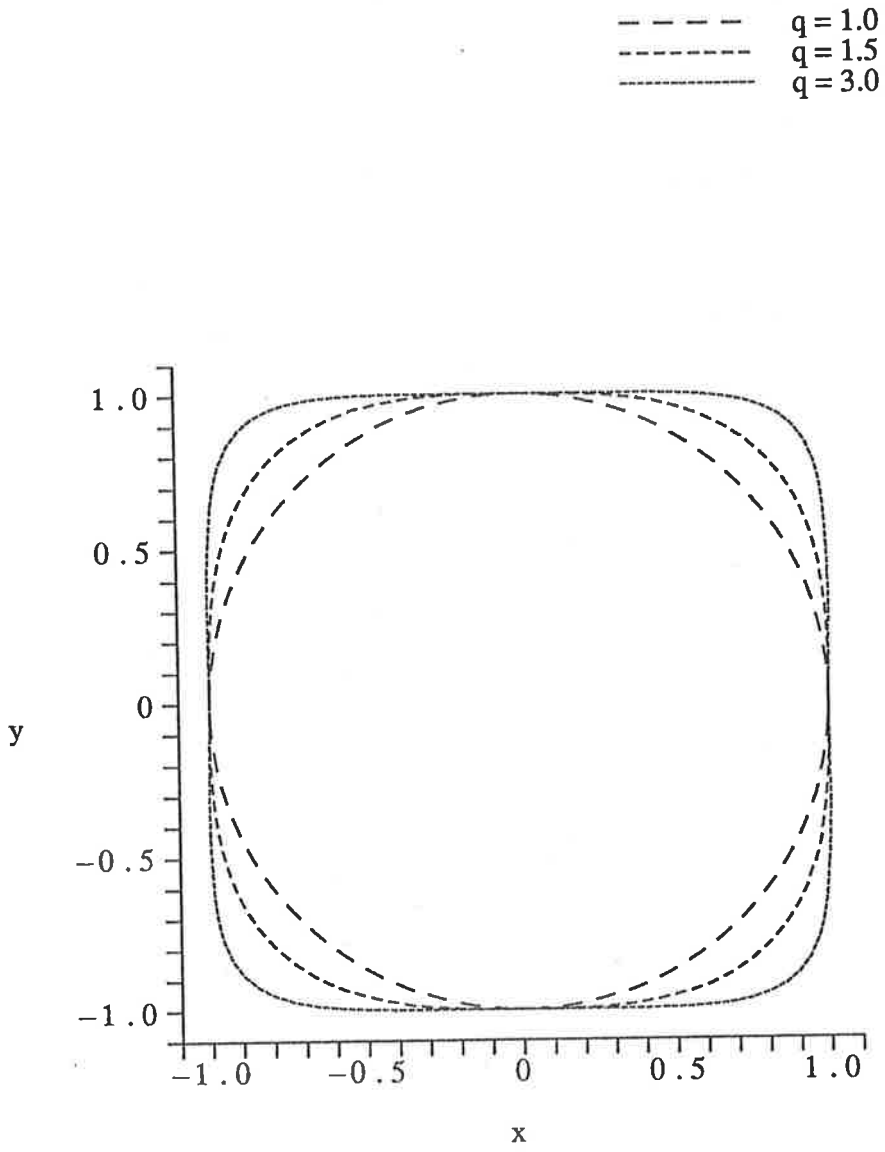

Figure 5.3 Planforms of aspect ratio one used to illustrate the behaviour of the transition point as the planform becomes more rectangular.

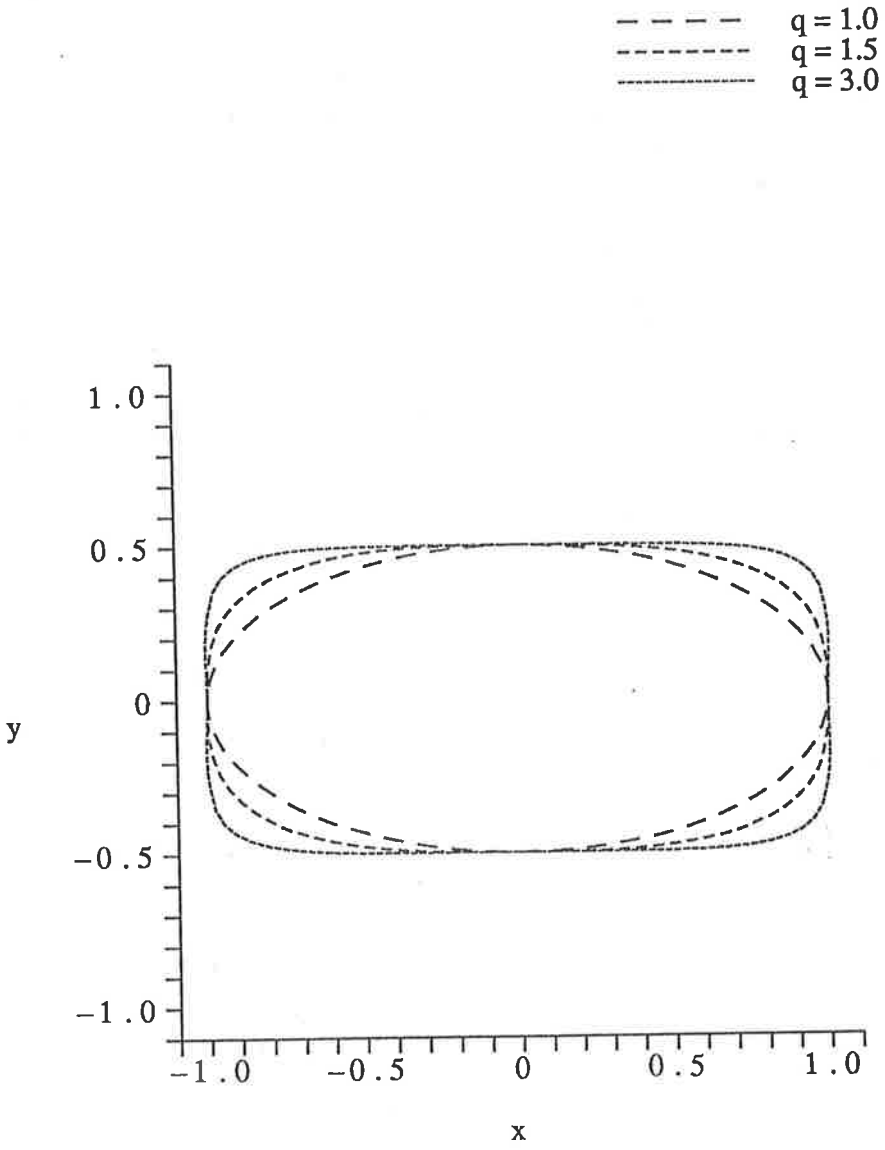

Figure 5.4 Planforms of aspect ratio 0.5 used to illustrate the behaviour of the transition point as the planform becomes more rectangular.

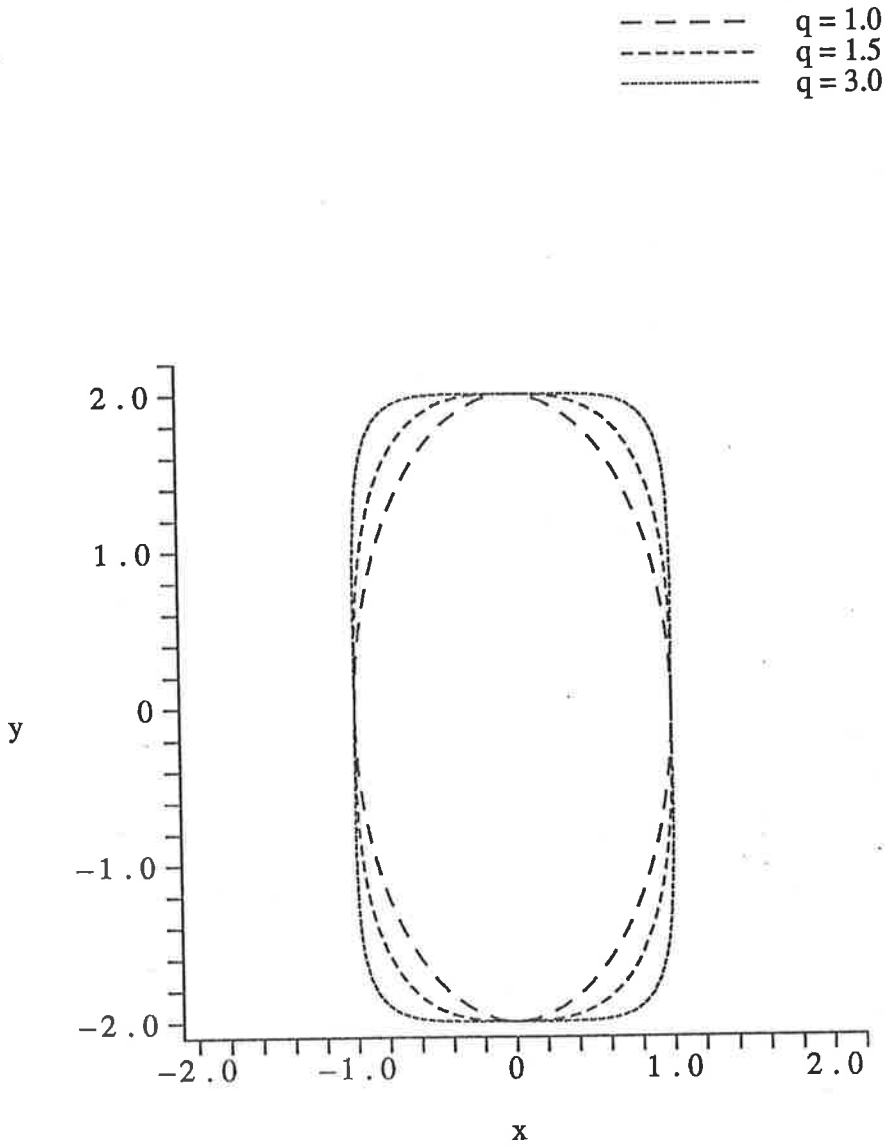

Figure 5.5 Planforms of aspect ratio two used to illustrate the behaviour of the transition point as the planform becomes more rectangular.

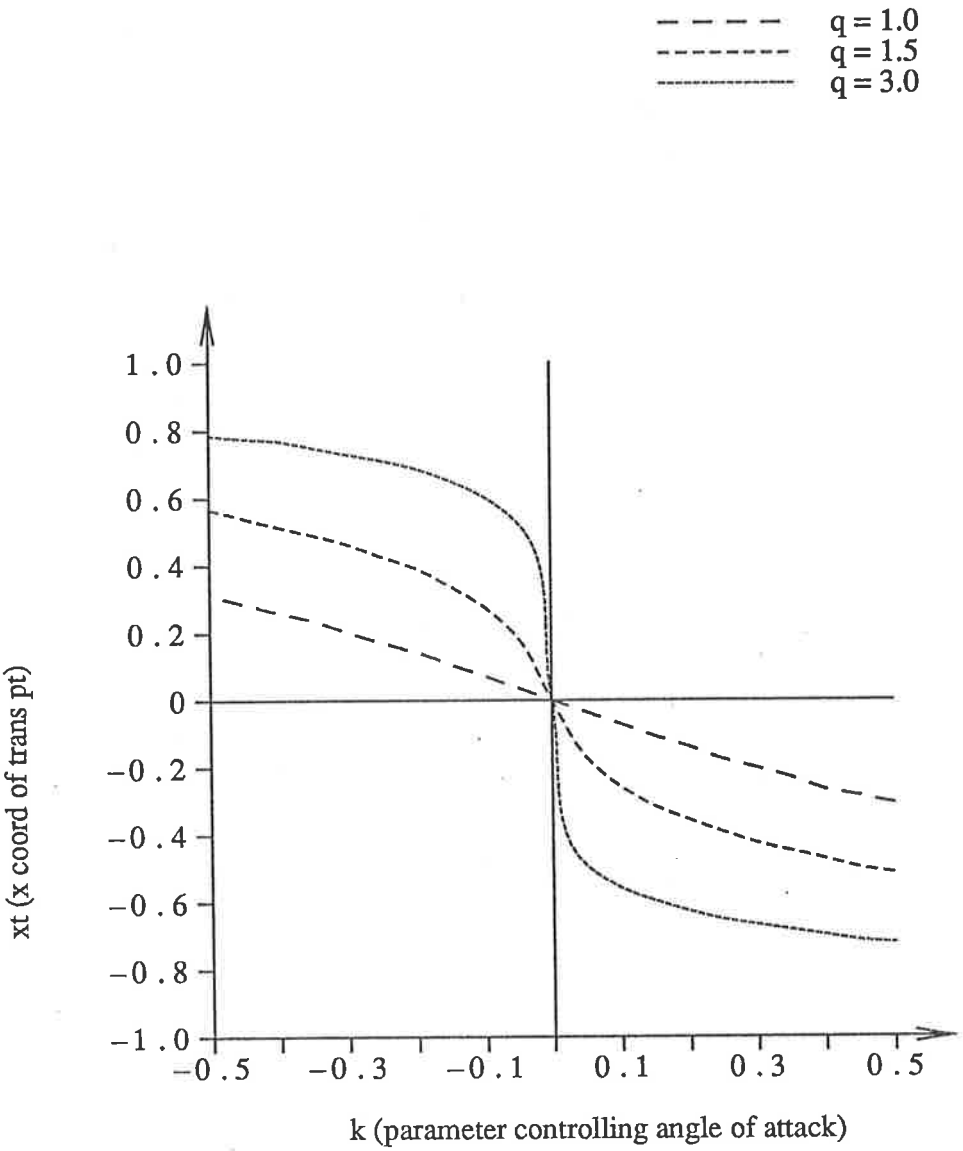

Figure 5.6 Graph of the x–coordinate of the transition point plotted against k, the parameter controlling the angle of attack, for the planforms illustrated in Figure 5.3.

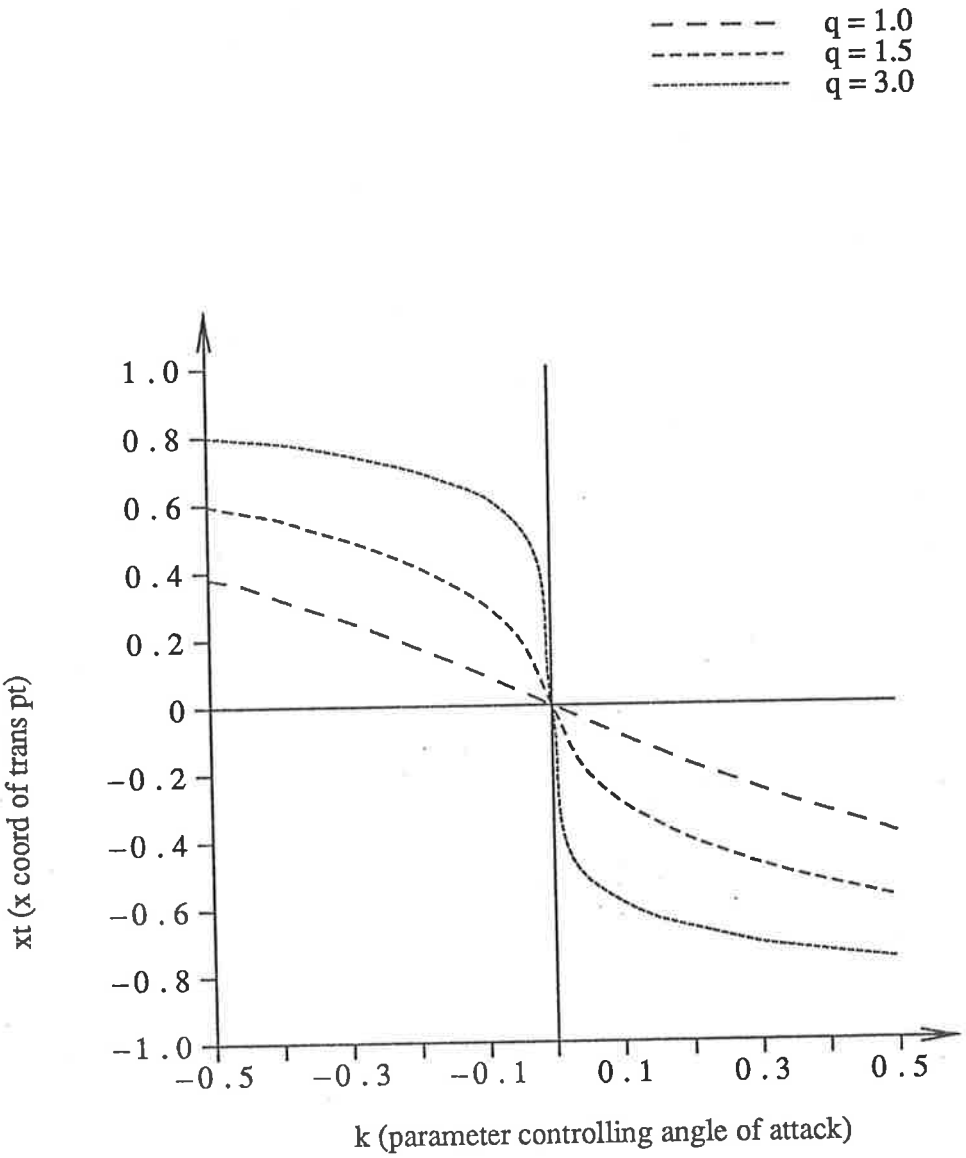

Figure 5.7 Graph of the x–coordinate of the transition point plotted against k, the parameter controlling the angle of attack, for the planforms illustrated in Figure 5.4.

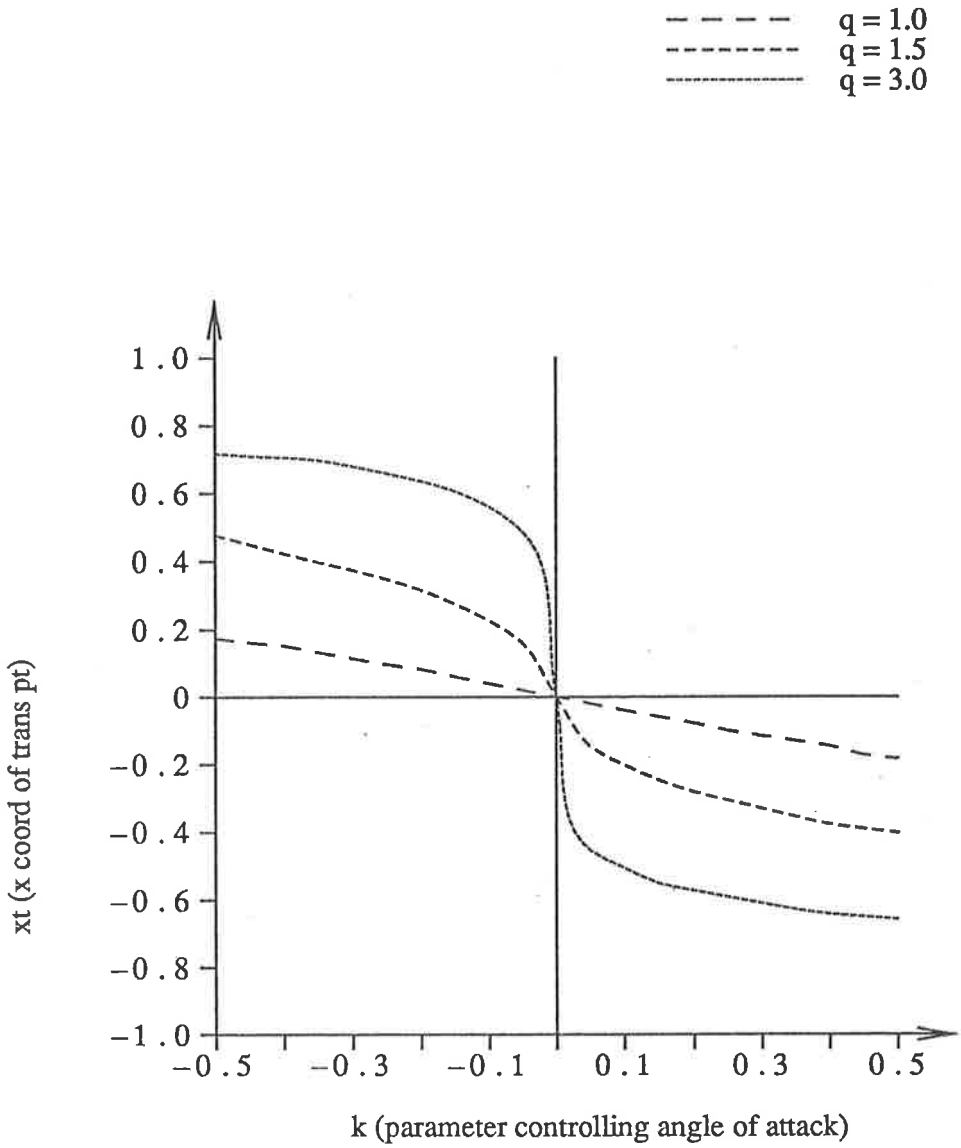

Figure 5.8 Graph of the x–coordinate of the transition point plotted against k, the parameter controlling the angle of attack, for the planforms illustrated in Figure 5.5.

body with negative angle of attack, the transition point would be located at the rear (downstream) corner and with positive angle of attack, at the front (upstream) corner. When the angle of attack is zero, it would appear that for a rectangular planform, or one with edges parallel to the stream, we have non-unique solutions.

CHAPTER 6

FIXED TRANSITION AND SKIRTS

In chapter five, we examined the location of the transition point between the leading edge and the trailing edge for near–rectangular bodies. We postulated that for a thin body which was rectangular in planform, the transition point would be located at the rear (front) corner for negative (positive) angle of attack.

We shall now apply this conjecture to the problem of a rectangular thin body moving in ground effect at a negative angle of attack and fix the transition point at the rear corner. Although geometrically simplistic, such a thin body could represent a racing car or a large ground effect vehicle as described in the introduction.

6.1 Rectangular Planforms

For this rectangular body, we solve the partial differential equation governing the flow in the gap below the body (3.6) subject to the leading edge condition (3.7) at the front of the body and along the sides and the trailing edge condition (3.8) along the rear portion of the body.

Whilst solving this system of equations, difficulties became apparent near the corners. These were due to the normal derivatives at each side of the corners having different limiting values, resulting in the non–existence of the derivatives at the corners. By using an increasingly fine grid towards the corners, the numerical

errors caused by the discontinuities were confined to the immediate neighbourhood of the corners, and therefore had negligible effect on the rest of the flow.

Figure 6.1 illustrates the computed values of the velocity potential ϕ and its normal derivative $\frac{\partial \phi}{\partial n}$ plotted against the arc–length l for a square planform with $k = -0.5$ in a uniform stream U of magnitude one. The arc–length l starts at the middle of the trailing edge where it takes the value zero. As it traces the outline of the positive y half of the square in the anticlockwise direction, it increases in value. Figure 6.2 contains the velocity potential ϕ and its normal derivative $\frac{\partial \phi}{\partial n}$ for the same planform, but with $k = -0.1$ and $U = 2.0$. In both examples, the contour of the body was divided into 104 segments and the sides were of length two. The velocity potential ϕ is continuous, although not differentiable, at the corners and for the leading edge sections, is completely determined by equation (3.7). Its normal derivative jumps in value as it goes round both the front and rear corners.

To check the physical validity of the flow, the mean normal component of velocity u_n is also shown in figures 6.1 and 6.2. We require that on Γ_L, the leading edge, $u_n < 0$ and that on Γ_T, the trailing edge, $u_n > 0$. As can be seen, these requirements are satisfied. For both values of k, it can also be noted that the jump in the mean normal component of velocity u_n at each corner is of the same magnitude as the uniform stream U. This is to be expected as the flow of the uniform stream U is parallel to the sides of the body and perpendicular to the front and rear.

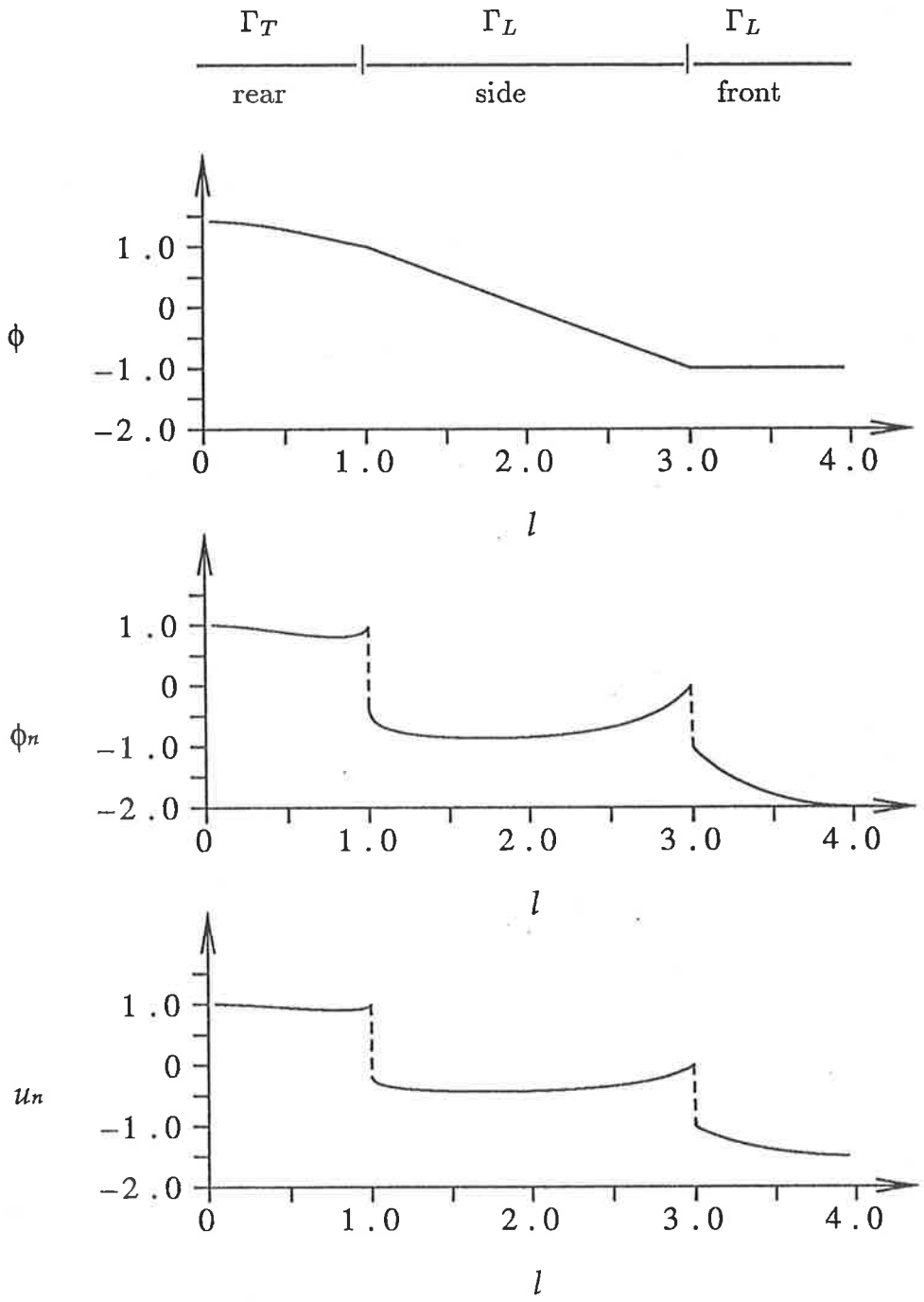

Figure 6.1 Plots of the velocity potential ϕ, its normal derivative ϕ_n and the mean normal component of velocity u_n against the arc–length l for a square planform with $k = -0.5$ and $U = 1.0$. The arc–length l starts at the middle of the trailing edge where it takes the value zero. As it traces the outline of the positive y half of the square in the anticlockwise direction, it increases in value. The square considered was of length two, and so the rear corner, where transition occurs, is situated at $l = 1.0$ and the front corner is situated at $l = 3.0$.

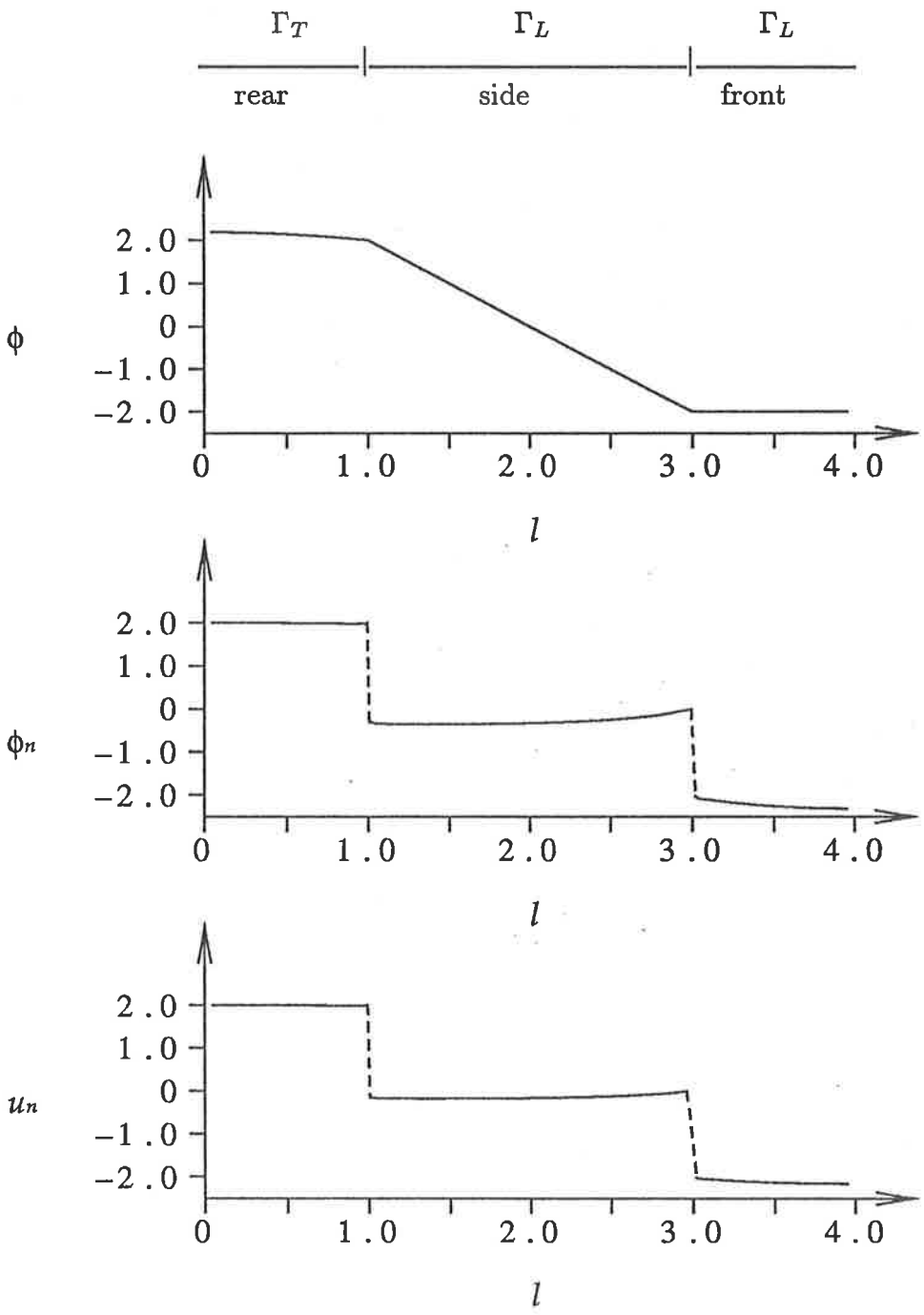

Figure 6.2 Plots of the velocity potential ϕ, its normal derivative ϕ_n and the mean normal component of velocity u_n against the arc–length l (as described in caption 6.1) for a square planform with $k = -0.1$ and $U = 2.0$. The square considered was of length two, and so the rear corner, where transition occurs, is situated at $l = 1.0$ and the front corner is situated at $l = 3.0$.

6.2 Rectangular Bodies with Skirts

The boundary value problem described by equations (3.6), (3.7) and (3.8), can be solved exactly if there is no dependence on y; that is, if $f = f(x)$ and $\phi = \phi(x)$. In this situation, the leading edge Γ_L is the point $x = -L$ and the trailing edge Γ_L is the point $x = L$ (Tuck (1983)). We find that

$$\frac{d\phi}{dx} = \frac{Uf(L)}{f(x)} \tag{6.1}$$

satisfies both equation (3.6) and the trailing edge boundary condition (3.8). We note that the negative of equation (6.1) also satisfies these equations but we will reject this possibility as it would involve inward rather than outward flow at the trailing edge.

This one dimensional channel flow problem has been discussed in various papers (see Tuck (1978), (1980), (1981), (1982b), (1983), Tuck and Bentwich (1983)). Tuck (1983) examined in detail the force generated on the thin body and found that the lift has an upper bound of $\frac{1}{2}\rho U^2 L$ per unit span. However, there is no lower bound on the force, and so the downward force can be made large. It is because of this ability to make the negative lift large that skirts were introduced to some racing cars. These skirts were solid sections built along the extreme sides of the car, filling the gap between the side and the ground. Therefore, they stopped air from escaping under the sides of the car, and the resulting channel–like flow beneath the car produced greater downward forces. The direct benefit of this was that the cars could go faster round corners with greater grip due to the downward

forces. They have since been banned partly because of instability problems in the situation where the car skids out of the two dimensional flow and partly due to political reasons.

We shall approximate the outline of the racing car by a rectangle to determine the effect skirts have on the racing cars and consequently will use only negative values of k. The problem described by equations (3.6), (3.7) and (3.8) can be modified to incorporate skirts by dividing the boundary Γ into three sections: the leading edge section, which must satisfy condition (3.7), the trailing edge section, which must satisfy condition (3.8) and, between these, the skirt section, which must satisfy a "no flow" condition. That is, on the skirt section Γ_s,

$$\frac{\partial \phi}{\partial n} = 0. \tag{6.2}$$

Therefore, equation (3.6), together with boundary conditions (3.7), (3.8) and (6.2), describes the flow below a rectangular body, which has a front leading edge, a rear trailing edge and skirts along the sides.

When the clearance between the thin body and the ground is constant in y and exponential in x, as described by equation (4.1), the differential equation (6.1) can be written as

$$\frac{d\phi}{dx} = Ue^{2k(x-L)}. \tag{6.3}$$

This equation can be solved directly for the velocity potential ϕ, and after applying the leading edge condition at $x = -L$, we find the solution to be

$$\phi(x) = \frac{U}{2k} e^{-2kL} \left(e^{2kx} - e^{-2kL}\right) - UL. \tag{6.4}$$

Figures 6.3, 6.4 and 6.5 contain comparisons of the exact solutions with the numerical solutions for the velocity potential ϕ, its normal derivative $\frac{\partial \phi}{\partial n}$ and the mean normal component of velocity u_n respectively. In this section, the body contour was divided into 104 segments with, as in the previous section, a finer spacing near the corners.

In each case, there is good agreement between the two sets of results. As with the rectangular bodies without skirts, the jump in the mean normal component of velocity u_n at the rear corner is of the same magnitude as the uniform stream U. However, at the front corner, the jump is larger. The one dimensional continuity equation demands that the velocity flux be constant through the gap and thus, for negative angle of attack, the velocity at the leading edge must be greater than the velocity at the trailing edge.

We can also consider skirts which do not go the full length of the body. However, the skirt must start at the rear corner as, in the limit as the length of the skirt tends to zero, the location of this limiting point is the transition point, which, as previously discussed, is at the rear corner for negative angle of attack and exponentially varying clearance. We find that when a skirt is placed part way along each of the sides of the body starting at the front corner, there is no physically feasible solution. In practice, the gap clearance beneath a racing car does not vary exponentially. The underbody of the car is designed in such a way that the gap clearance decreases from the front to a minimum value at some intermediate point along its body length, and from this point, the clearance remains (almost)

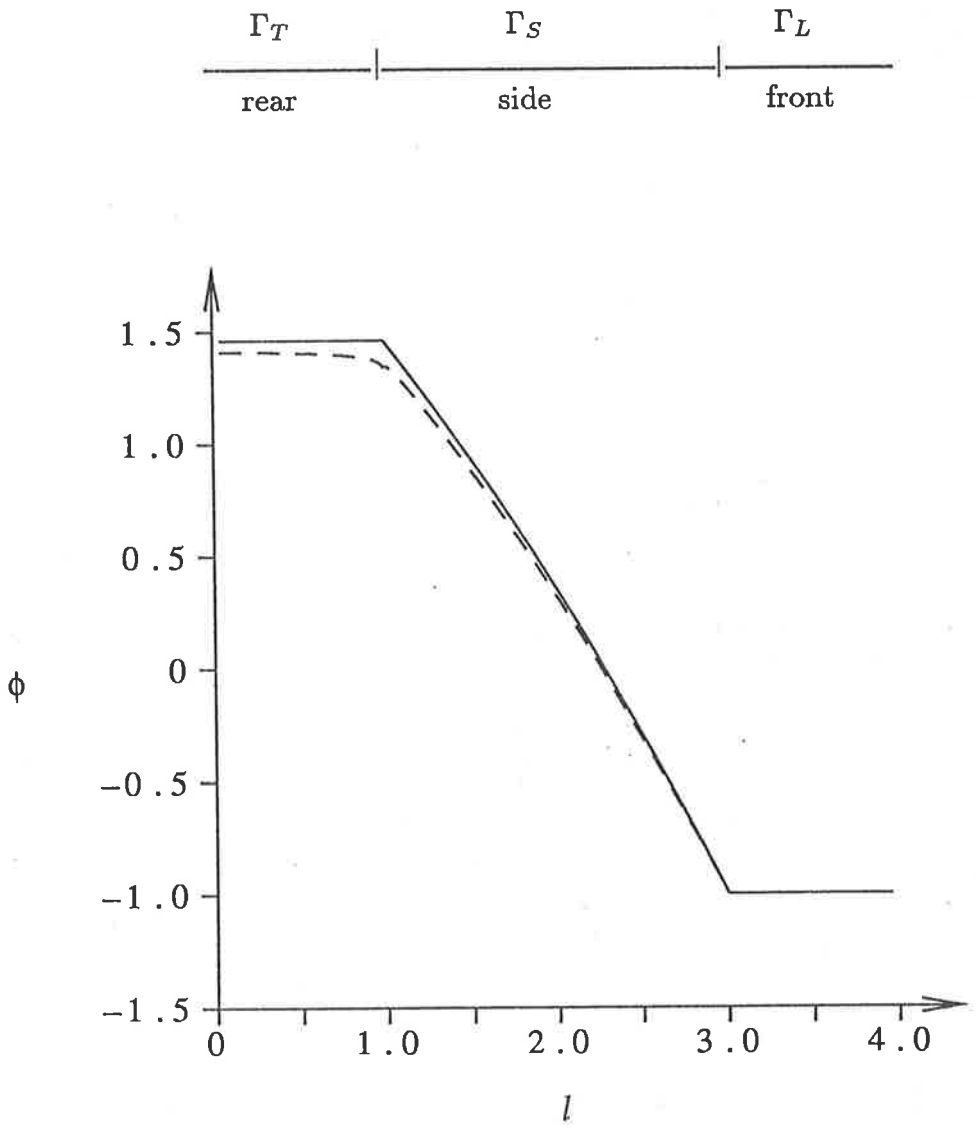

Figure 6.3 Comparison of the exact solution (——) for the velocity potential ϕ with the computed values (– – –) of ϕ against the arc–length l (as described in caption 6.1) for a body with a square planform with skirts the full length of the sides. In this example, the body was of length two and $k = -0.1$.

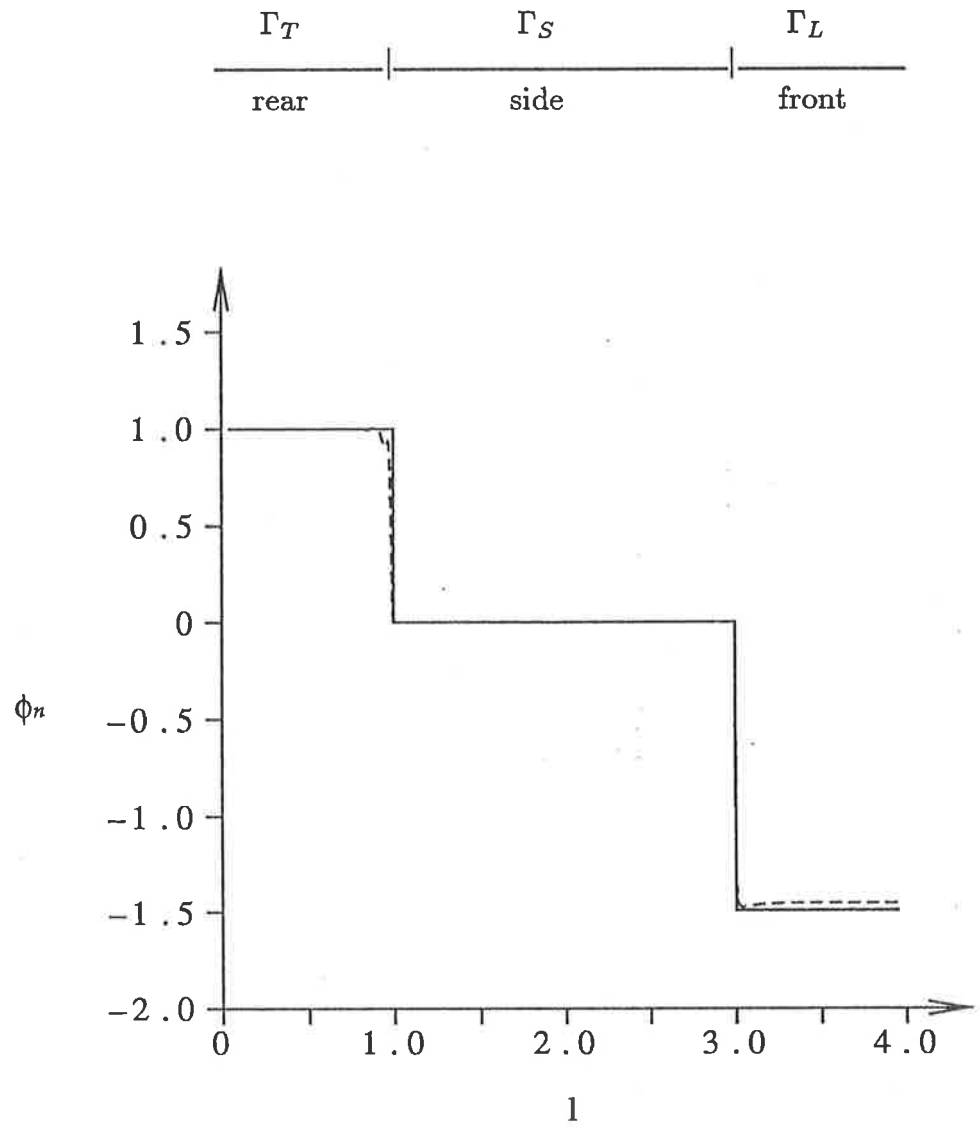

Figure 6.4 Comparison of the exact solution (——) for the normal derivative of the velocity potential ϕ_n with the computed values (– – –) of ϕ_n against the arc–length l (as described in caption 6.1) for a body with a square planform with skirts the full length of the sides. In this example, the body was of length two and $k = -0.1$.

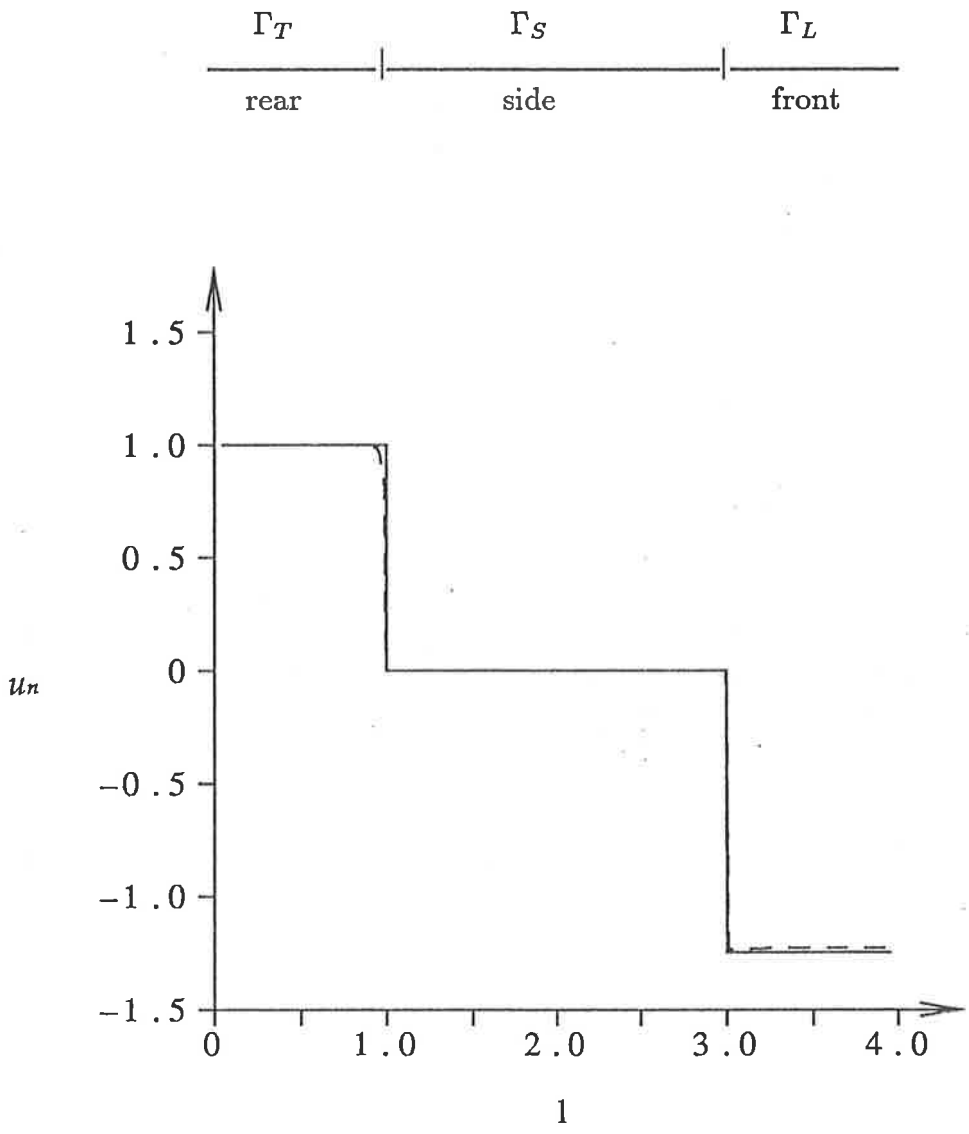

Figure 6.5 Comparison of the exact solution (——) for the mean normal component of velocity u_n with the computed values (– – –) of u_n against the arc–length l (as described in caption 6.1) for a body with a square planform with skirts the full length of the sides. In this example, the body was of length two and $k = -0.1$.

constant. In the rearward portion of constant clearance, the pressure is equal to the uniform stream pressure and, therefore, this portion has no effect on the net lift or the flow. Hence, to preserve the beneficial low pressure at the point of minimum clearance, skirts need only be attached along the section of the body forward of this point.

The velocity potential ϕ, its normal derivative $\frac{\partial \phi}{\partial n}$ and the mean normal component of velocity u_n for a square planform with skirts along the rear half of the sides and with $k = -0.1$ are shown, plotted against the arc–length l, in figure 6.6. As expected, the inclusion of the half–skirts has produced another discontinuity in the normal derivatives at the junction of the skirt with the leading edge.

As a measure of the effect of the skirts on the force, the pressure coefficient C_p, defined by

$$C_p = 1 - \frac{|\nabla \phi|^2}{U^2}, \tag{6.5}$$

has been computed at the centre of the front of the body. This is where the largest downward forces will be experienced and therefore, by considering various lengths of skirts, will give a good indication of the negative lift enhancement. Figure 6.7 shows the relationship between the proportion of the side which has a skirt, and the pressure coefficient C_p. It can be seen from this figure that having skirts the full length of the body produces four times as much lift as having no skirts. In order to generate half the lift of full skirts, the body must have skirts along nearly 70% of its sides. Also from this figure, it can be seen that the front 10% of the

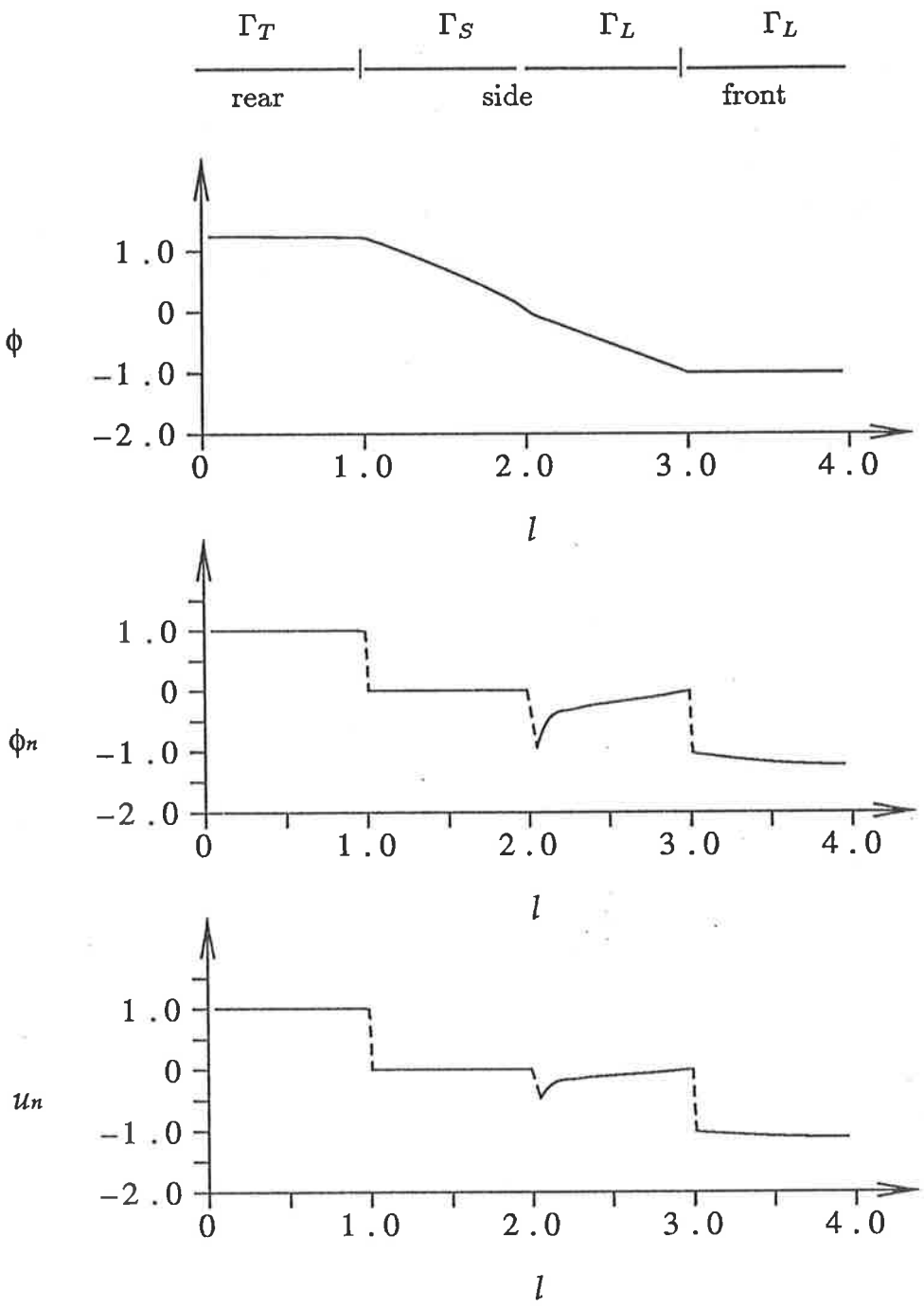

Figure 6.6 Plots of the velocity potential ϕ, its normal derivative ϕ_n and the mean normal component of velocity u_n against the arc–length l (as described in caption 6.1) for a square planform with $k = -0.1$. The body has skirts along the rear half of its sides.

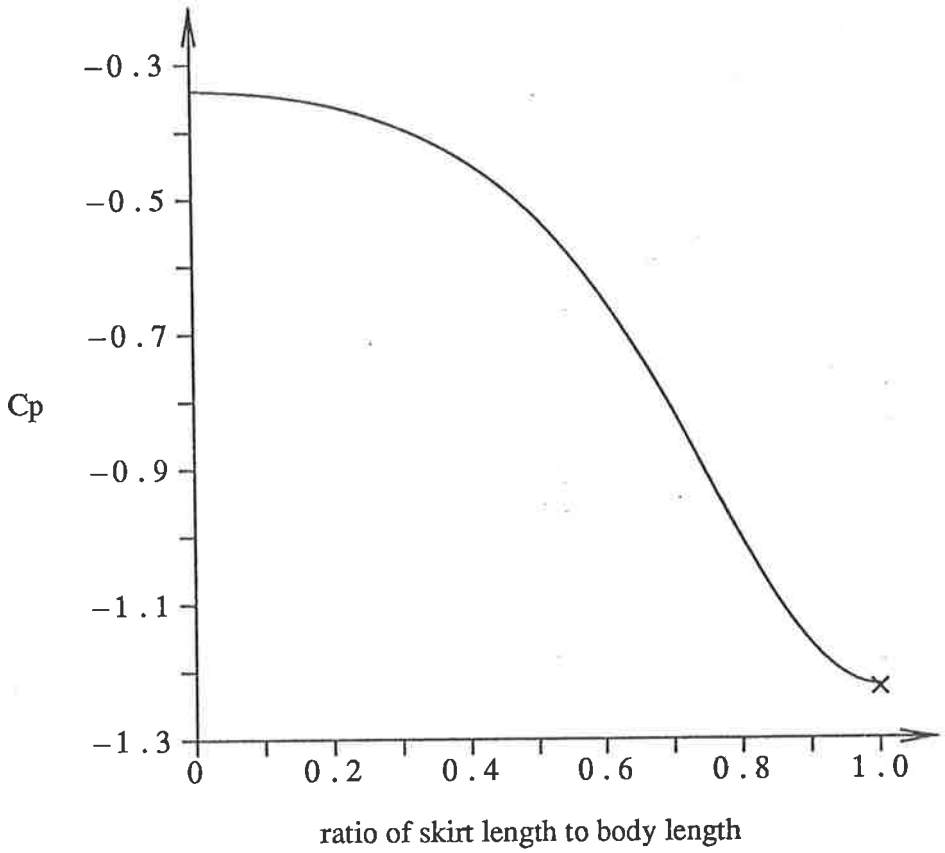

Figure 6.7 Plot of the pressure coefficient C_p (at the middle of the front of the body) versus the ratio of the length of the skirts, which must start at the rear corner, to the length of the sides of the body. In this example, the body was square in planform and of length two, and $k = -0.1$. The cross represents the exact solution for the case of full skirts.

skirts have negligible effect on the lift; that is, a body with skirts along 90% of its sides generates approximately the same lift as one with full skirts. When the body has full skirts, the flow in the gap is one dimensional and the pressure coefficient can be calculated exactly from the exact solution for the velocity potential ϕ. The exact pressure coefficient for the example of the square planform with $k = -0.5$ is represented in figure 6.7 by a cross, and is in good agreement with the computed pressure coefficient for full skirts.

6.3 Inverse Solutions

Our aim is to design the planform for a thin body in such a way that this design satisfies all the constraints for our extreme ground effect problem. We shall assume that the planform has a straight leading edge section at $x = 0$, a straight trailing edge section at $x = L$ and the, as yet unknown, sides of the body are leading edge sections; that is, the transition points between the leading edge and the trailing edge are fixed at the rear corners of the body. This means that the body must be flying with a negative angle of attack. We will also assume that the body is symmetrical about the x–axis and we will determine a solution of the form

$$\phi(x, y) = F(x) \cos \lambda y, \tag{6.6}$$

for which $F(x)$ is to be determined.

Firstly, this solution must satisfy the partial differential equation (3.6) governing the flow beneath the body. When we substitute this solution (6.6) into

equation (3.6), we find that $F(x)$ must be a solution to the differential equation

$$\frac{d^2}{dx^2}F(x) - 2k\frac{d}{dx}F(x) - \lambda^2 F(x) = 0. \tag{6.7}$$

The solution to this ordinary, second–order differential equation, with constant coefficients, is

$$F(x) = e^{kx}(A\cosh\mu x + B\sinh\mu x), \tag{6.8}$$

where $\mu = \sqrt{\lambda^2 + k^2}$, and A and B are constants.

On the leading edge at $x = 0$, the boundary condition (3.7) must be satisfied. By applying this boundary condition to (6.8), we find that the constant A must equal zero. Therefore, our solution thus far is

$$\phi(x, y) = e^{kx}B \tag{6.9}$$

The planform has a trailing edge at $x = L$ and the appropriate boundary condition (3.8) requires that

$$\begin{aligned}\Big(Be^{kx}\cos\lambda y[k\sinh\mu x + \mu\cosh\mu x]\Big)^2 \\ + \Big(-B\lambda e^{kx}\sinh\mu x\sin\lambda y\Big)^2 = U^2\end{aligned} \tag{6.10}$$

at $x = L$. We note that the first term has a factor $(\cos\lambda y)^2$ and the second term has a factor $(\sin\lambda y)^2$, and therefore equation (6.10) can be satisfied if the coefficients of these factors each equals U^2. That is,

$$\Big(Be^{kL}[k\sinh\mu L + \mu\cosh\mu L]\Big)^2 = U^2 \tag{6.11}$$

and

$$\left(B\lambda e^{kL}\sinh\mu L\right)^2 = U^2. \tag{6.12}$$

These two equations provide the required solutions for the unknown constants L and B. From equation (6.12), we find that

$$B = \pm\frac{Ue^{kL}}{\lambda\sinh\mu L} \tag{6.13}$$

and, without loss of generality, we shall select the positive sign. By comparing equations (6.11) and (6.12), we see that

$$k\sinh\mu L + \mu\cosh\mu L = \pm\lambda\sinh\mu L, \tag{6.14}$$

or

$$L = \frac{1}{\mu}\operatorname{arctanh}\left(\frac{\mu}{-k\pm\lambda}\right). \tag{6.15}$$

Once again, we will take the positive sign for our solution. We now have the final form for the velocity potential ϕ:

$$\phi(x,y) = \frac{Ue^{k(x-L)}}{\lambda}\frac{\sinh\mu x}{\sinh\mu L}\cos\lambda y, \tag{6.16}$$

in which L is as defined in equation (6.15).

To complete our inverse solution, we must determine the equation describing the leading edge section along the side of the body. Since this section must satisfy the boundary condition (3.7), we can substitute equation (6.16) into (3.7) and rearrange to give an expression for y, namely

$$y = \frac{1}{\lambda}\arccos\left(\frac{\lambda x e^{k(L-x)}\sinh\mu L}{\sinh\mu x}\right). \tag{6.17}$$

Figure 6.8 illustrates two typical planforms produced using this inverse solution. The uniform stream U was of magnitude one as was the parameter λ. Two different values of k, the parameter controlling the angle of attack, were used. The narrower, longer body was produced with $k = -0.4$ and the other body was produced with $k = -0.5$. The sides, which are almost linear, form acute angles at the front corners of the body and this creates special problems when calculating the singular matrix coefficients A_s, defined in equation (4.22). For smooth contours, care must be taken to ensure when calculating these coefficients, that the two terms $\arctan\left(\frac{y_i - Y_{j+1}}{x_i - X_{j+1}}\right)$ and $\arctan\left(\frac{y_i - Y_j}{x_i - X_j}\right)$ are on the same arctan branch. However, when the contour has sharp corners, this requirement is no longer correct and the restriction must be removed at these corners. To check that the matrix A_s is being computed correctly, we consider the row sums of A_s. For a straight line segment, the interior angle measured at the middle of the segment is π and as the ith row sum is $\frac{1}{\pi}$ x (the interior angle at the ith segment), each row sum should equal one.

A comparison of the exact and numerical values of the velocity potential ϕ, for the planform illustrated in figure 6.8 with $k = -0.5$ are shown in figure 6.9. The body contour was divided into 102 segments. As most of the contour is leading edge, and therefore subject to condition (3.7), the agreement between the two sets of results is good. There are discontinuities in the slope of the curves at both corners but the discontinuity at the front corner is much more pronounced, as expected. Figure 6.10 also shows good agreement between the exact and numerical values of the normal derivative of the velocity potential $\frac{\partial \phi}{\partial n}$.

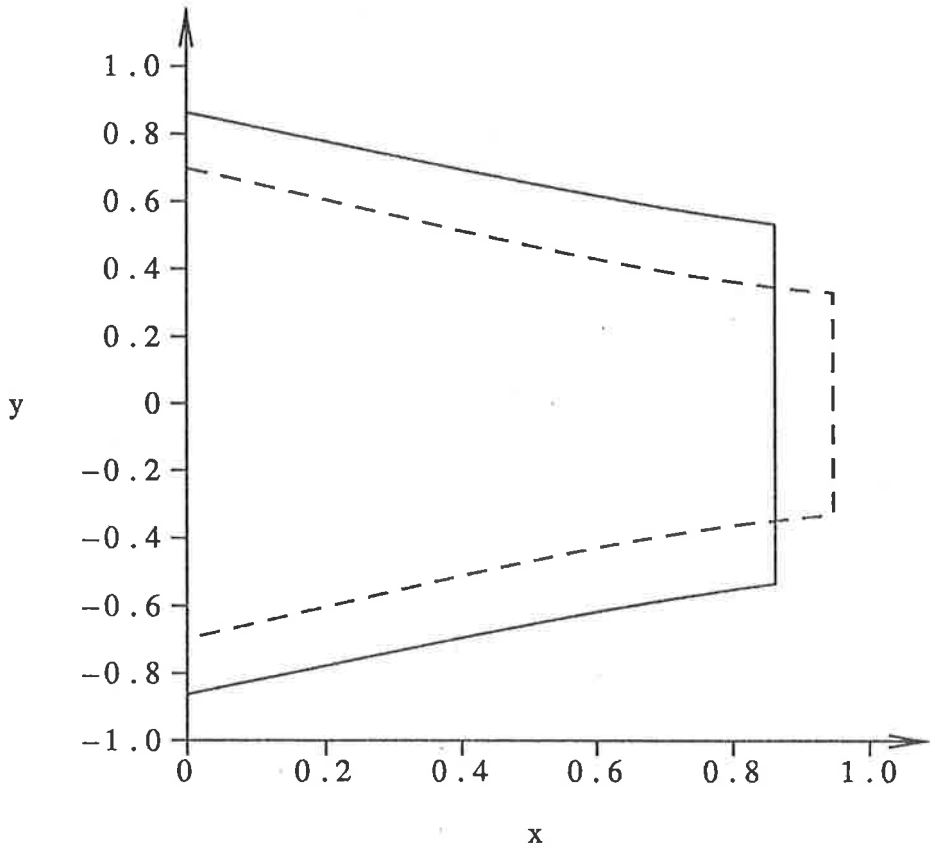

Figure 6.8 Two planforms created using the inverse solution with parameter $\lambda = 1.0$ and stream velocity $U = 1.0$. For one planform, k the parameter controlling the angle of attack equalled –0.5 (———) and for the other, $k = -0.4$ (– – –).

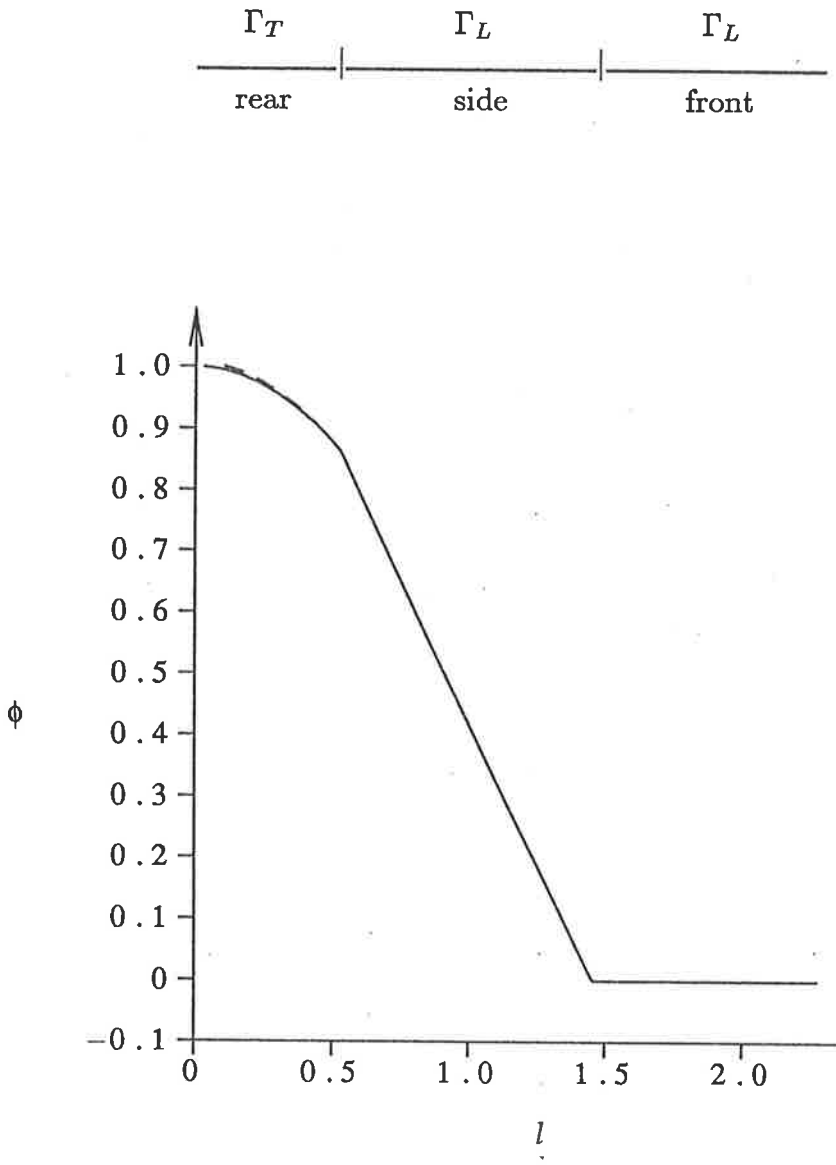

Figure 6.9 Comparison of the exact solution (——) for the velocity potential ϕ with the computed values (– – –) of ϕ against the arc–length l (as described in caption 6.1) for the body illustrated in figure 6.8 with $k = -0.5$ and $\lambda = 1.0$.

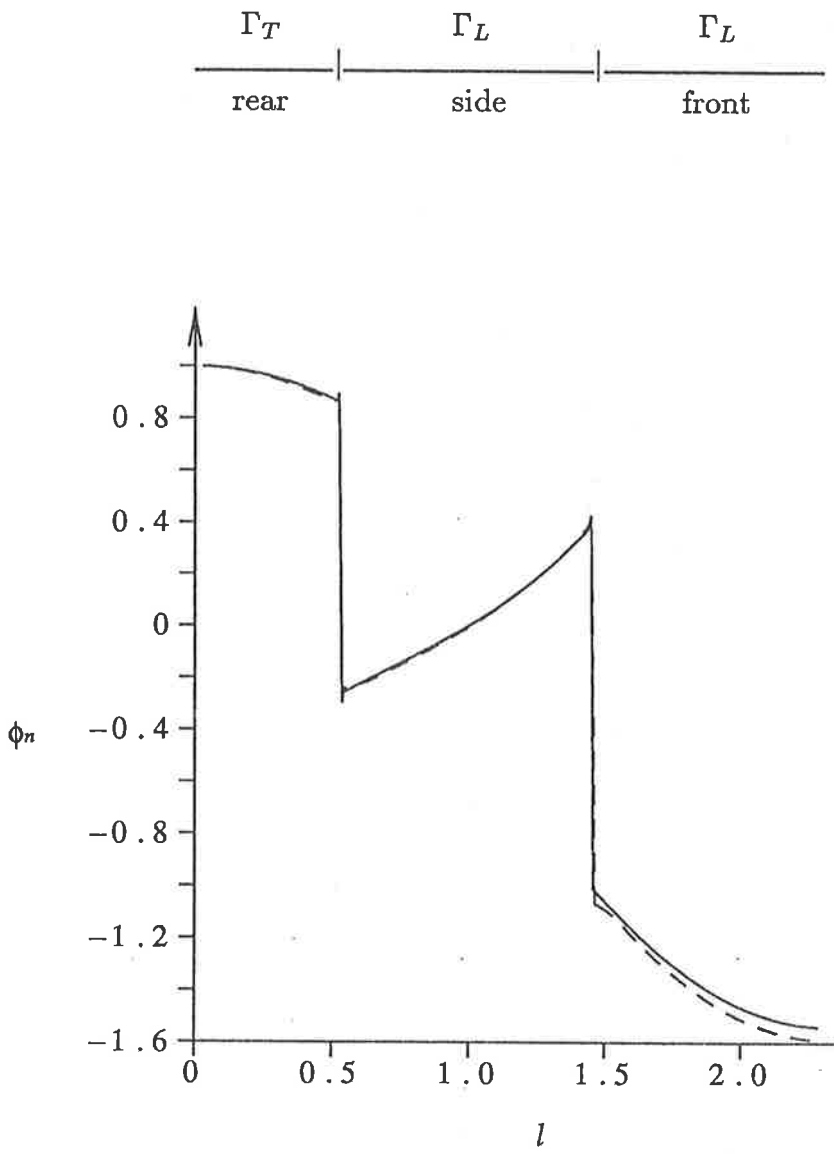

Figure 6.10 Comparison of the exact solution (——) for the normal derivative of the velocity potential ϕ_n with the computed values (– – –) of ϕ_n against the arc–length l (as described in caption 6.1) for the body illustrated in figure 6.8 with $k = -0.5$ and $\lambda = 1.0$.

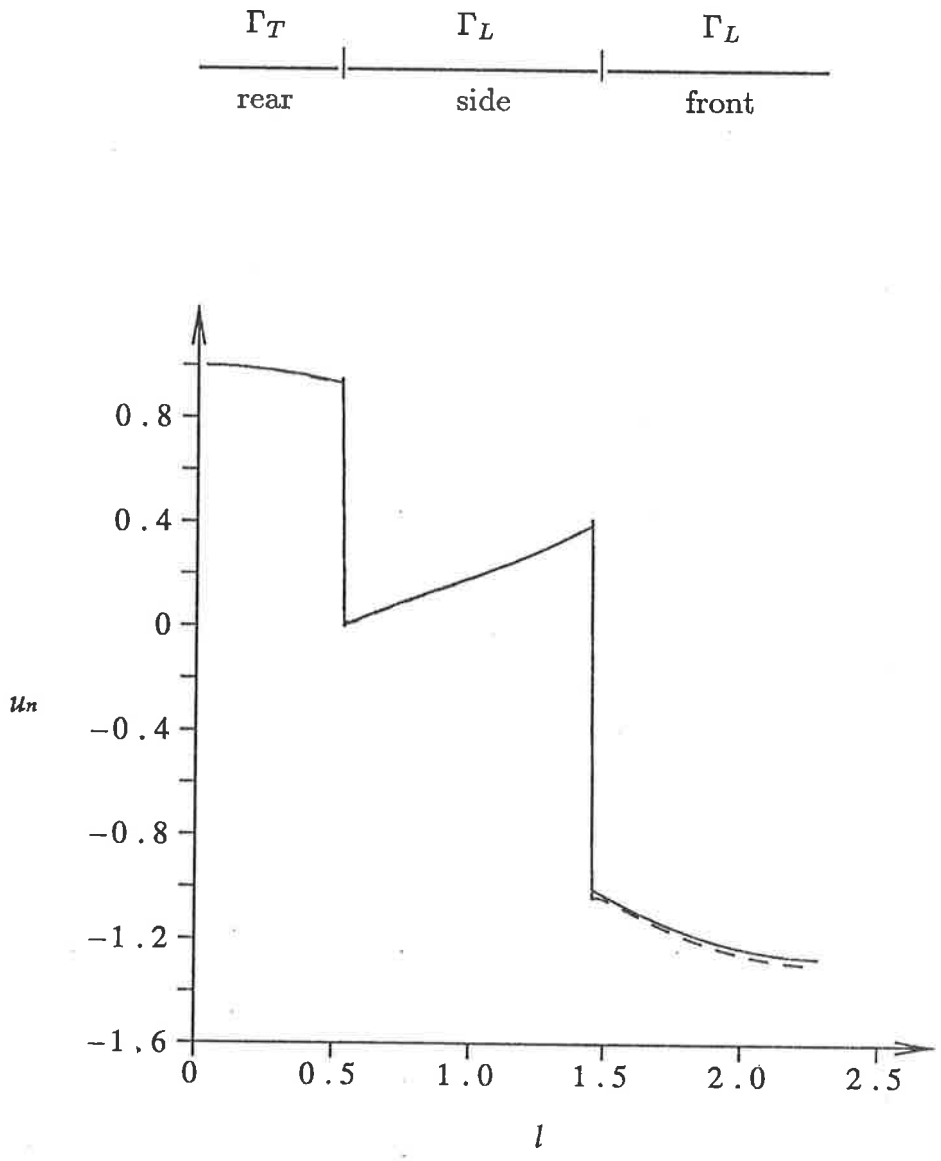

Figure 6.11 Comparison of the exact solution (——) for the mean normal component of velocity u_n with the computed values (– – –) of u_n against the arc–length l (as described in caption 6.1) for the body illustrated in figure 6.8 with $k = -0.5$ and $\lambda = 1.0$.

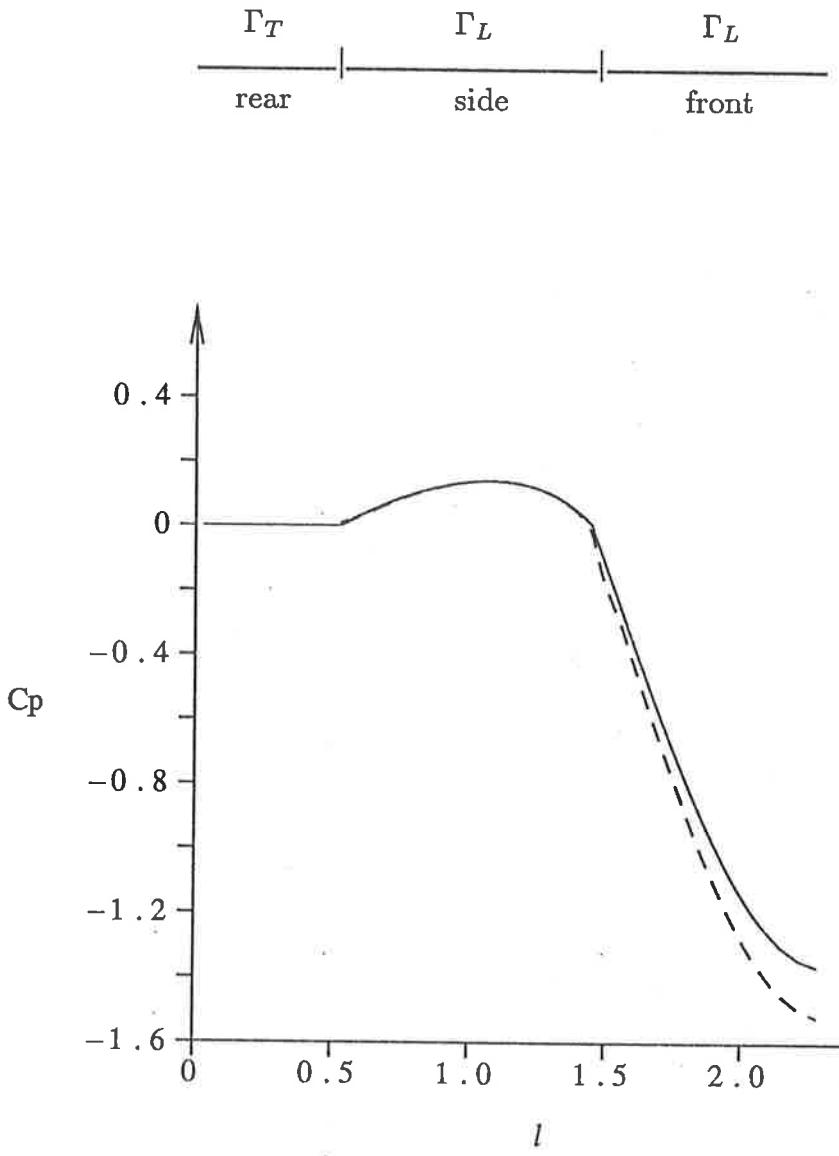

Figure 6.12 Comparison of the exact solution (——) for the pressure coefficient C_p with the computed values (– – –) of C_p against the arc–length l (as described in caption 6.1) for the body illustrated in figure 6.8 with $k = -0.5$ and $\lambda = 1.0$.

The exact and numerical values of the mean normal component of velocity u_n are graphed in figure 6.11. It can be seen that although the inverse solution satisfies all the governing conditions of the ground effect problem, it is not a physically viable solution as $u_n > 0$ on the leading edge side. This contravenes the physical definition of the leading edge as being the contour section where the fluid passes from outside the perimeter of the body to inside the perimeter of the body.

Figure 6.12 compares the exact and numerical values of the pressure coefficient C_p. For the rear and side portions of the body contour, the agreement is good. However, along the front section, the difference between the two sets of results gets larger as the C_p values get larger, due to the squaring of the errors.

Although the inverse solutions are not physically feasible, they have been useful as a comparison to determine how accurately the analytical–numerical scheme models acute corners.

CHAPTER 7

CONCLUSION

7.1 Conclusion

The purpose of this thesis is to study the air flow about a thin body moving steadily in extreme ground effect. In such cases when the clearance between the body and the ground is small, the prevailing three dimensional flow can be approximated by two dimensional flow in the gap between the body and the ground.

The partial differential equation governing this gap flow and the associated leading edge and trailing edge boundary conditions on the body are derived using the method of matched asymptotic expansions as described by Van Dyke (1964). A combination of numerical and analytical techniques is used to approximate the governing equation by a matrix equation for the case when the clearance is constant in y and exponential in x. The velocity potential and its normal derivative are then determined from the matrix equation using an iterative scheme.

Some theory is developed for thin bodies with low aspect ratio, and a simple equation relating k, the parameter controlling the angle of attack, to the x–coordinate of the transition point is derived. This relationship agrees with the low aspect ratio theory developed by Newman (1982).

Location of the transition point between the leading edge and the trailing edge is then investigated for thin bodies with near–rectangular planforms by considering a family of super–ellipses. We find that as the planform becomes more

rectangular, the transition point moves to the front (rear) for positive (negative) angle of attack. We then postulate that if the body was rectangular, the transition point would be located at the appropriate corner.

This conjecture is applied to rectangular thin bodies, and results are presented for negative angle of attack. Skirts are added to the contour and comparisons are made between rectangular bodies with skirts and those without. It can be readily seen that the addition of skirts to a thin body greatly increases the downward lift. In fact, this increase in negative lift occurs even when the skirts are not the full length of the body. If the skirts are only part of the way along the body, they must start at the rear corner when the clearance varies exponentially as assumed in the present numerical work. An inverse solution to the extreme ground effect problem is then developed and although it is not a physically feasible solution, it serves as a comparison to determine the accuracy with which the analytical–numerical scheme models sharp corners.

The computational method presented, for solving the flow around thin bodies in extreme ground effect, is applicable to general planforms with smooth contours and, if care is taken, can be used for planforms with sharp corners.

7.2 Suggestions for further research

There are several possibilities for extension of the work in this thesis. Firstly, thin bodies with more geometrically complicated planforms could be examined. The planforms studied in this thesis were chosen to illustrate various

properties, for example flow at corners, and to enable comparisons to be made with other work in this area.

The flow around thin bodies of general clearance could be solved by developing a fully numerical scheme to solve the governing equations. Calculations involving interior points could be done using the matrix equation (4.30). These extensions could then be used to investigate further such problems as the flow around artificial heart valves, skimboards and computer read–write heads.

REFERENCES

ABRAMOWITZ, M. & STEGUN I.A. (eds.) 1964 *Handbook of mathematical functions.* Dover, New York.

ADAMS, G.G. 1980 Procedures for the study of the flexible–disk to head interface. *IBM J. Res. Develop.* **24**, 512-517.

BAGLEY, J.A. 1961 The pressure distribution on two– dimensional wings near the ground. *Aero. Res. Counc. R. & M.* no. **3238**

BATCHELOR, G.K. 1970 *An introduction to fluid mechanics.* Cambridge University Press, U.K.

BIGG, G.R. 1983 *Diffraction and trapping of waves by cavities and slender bodies.* Ph.D. Thesis. University of Adelaide.

CHESTER, C.R. 1971 *Techniques in partial differential equations.* McGraw–Hill Inc.

EDGE, R.D. 1968 The surf skimmer. *Amer. Jour. of Phys.* **36**, 630-631.

GRUNDY, I.H. 1986 Airfoils moving in air close to a dynamic water surface. *J. Austral. Math. Soc. Ser. B.* **27**, 328-347.

HOLT, D.J. 1982 Underbody aerodynamics: the next area of refinement. *Soc. Auto. Eng. Inc.,* (Oct.), **90**, 57-62.

KOBER, H. 1952 *Dictionary of Conformal Representations.* Dover Pub. Inc.

KOGURE, K. et al. Design of negative pressure slider for magnetic recording disks. 1983 *Trans. ASME* **105**, 496-502.

LEE, J.J. 1969 Wave induced oscillations in harbours of arbitrary shape. *Cal. Ins. Tech. W.M. Keck Lab. Hydraul. Water Res. Rep. KH-R* **20**, 1-266.

NEWMAN, J.N. 1982 Analysis of small-aspect-ratio lifting surfaces in ground effect. *J. Fluid Mech.* **117**, 305-314.

OLLILA, R.G. 1980 Historical review of WIG vehicles. *J. Hydronautics.* **14**, 65-76.

PISTOLESI, E. 1937 Ground effect–theory and practice. *N.A.C.A., T.M.* no. **828**

PRYDE, A.J. & VAN DER HOEK, J. 1984 On a mixed free–boundary value problem which arises in the study of flows under thin bodies. *Aust. Nat. Uni. Res. Rep. 5*

SCOTTEN, L.N. et al. 1980 The new tilting–disc cardiac valve prosthesis. In vitro comparison of their hydrodynamic performance in the mitral position. *J. Thoracic Cardiovascular Surgery.* **79**, 680-688.

SHEPHERD, J.J. 1986 Asymptotic analysis of a narrow gas– lubricated flat sector thrust bearing. *RMIT Tech. Rep. 1*

SOVRAN, G., MOREL, T., & MASON, W.T. 1978 *Aerodynamic drag mechanisms of bluff bodies and road vehicles.* Plenum Press.

STRAND, T., ROYCE, W.W. & FUJITA, T. 1962 Cruise performance of channel–flow ground effect. *J. Fluid Mech.* **98**, 33-47.

TUCK, E.O. 1971 Irrotational flow past bodies close to a plane surface. *J. Fluid Mech.* **50**, 481-491.

TUCK, E.O. & NEWMAN, J.N. 1974 Hydrodynamic interactions between ships. *10th Symp. Naval Hydro., Cambridge, Mass. Proc., Office of Naval Res., Washington, D.C.,* pp **35-70**

TUCK, E.O. 1975 Matching problems involving flow through small holes. *Adv. Appl. Mech.*, **15**, 89-158.

TUCK, E.O. 1978 Unsteady small–gap ground effects. *Engng. Sci. Rep.* **78-1**, *Calif. Inst. Tech., Pasadena.*

TUCK, E.O. 1980 A non-linear unsteady one-dimensional theory for wings in extreme ground effect. *J. Fluid Mech.* **98**, 33-47.

TUCK, E.O. 1981 Steady flow and static stability of airfoils in extreme ground effect. *J. Eng. Math.* **15**, 89-102.

TUCK, E.O. 1982a Two-dimensional leaflet valves with maximum reverse-flow moment. *J. Eng. Math.* **16**, 47-57.

TUCK, E.O. 1982b An inviscid theory for sliding flexible sheets. *J. Austral. Math. Soc. (Ser. B)* **23**, 403-415.

TUCK, E.O. 1983 Non-linear extreme ground effect on thin wings of arbitrary aspect ratio. *J. Fluid Mech.* **136**, 73-84.

TUCK, E.O. & BENTWICH, M. 1983 Sliding sheets: Lubrication with comparable viscous and inertia forces. *J. Fluid Mech.* **135**, 51-69.

TUCK, E.O. 1984 A simple one dimensional theory for air– supported vehicles over water. *J. Ship Res.* **28**, 290-292.

TUCK. E.O. 1985 (unpublished report, work done at Stanford University).

VAN DYKE, M.D. 1975 *Perturbation methods in fluid mechanics.* Parabolic Press, Stanford.

WIDNALL, S.E. & BARROWS, T.M. 1970 An analytic solution for two and three dimensional wings in ground effect. *J. Fluid Mech.* **41**, 769-792.

WISE, C.E. 1979 Will the wing car fly at Indy? *Machine Design* (May), pp. **24-31**.

YIH, C.S. 1974 Fluid mechanics of colliding plates. *Physics of Fluids* **17**, 1936-1940.